2

PL-TR-93-2147

Penetrating Radiation Environment and Effects Study

H. D. Voss
W. L. Imhof
J. Mobilia
E. E. Gaines

Space Sciences Laboratory, 091-20, B255
Lockheed Palo Alto Research Laboratory
3251 Hanover Street
Palo Alto, Ca. 94304

JUNE 15, 1993

Scientific Report No. 1

Approved for public release; distribution unlimited

PHILLIPS LABORATORY
Directorate of Geophysics
AIR FORCE MATERIEL COMMAND
HANSCOM AFB, MA 01731-3010

"This technical report has been reviewed and is approved for publication"

Kevin P. Ray
KEVIN P. RAY, Capt, USAF
Contract Manager

E G Mullen
E.G. MULLEN, Chief
Space Particles Env. Branch

William Swider
WILLIAM SWIDER
Deputy Director

This report has been reviewed by the ESC Public Affairs Office (PA) and is releasable to the National Technical Information Service (NTIS).

Qualified requestors may obtain additional copies from the Defense Technical Information Center. All others should apply to the National Technical Information Service.

If your address has changed, or if you wish to be removed from the mailing list, or if the addressee is no longer employed by your organization, please notify PL/TSI, 29 Randolph Road, Hanscom AFB, MA 01731-3010. This will assist us in maintaining a current mailing list.

Do not return copies of this report unless contractual obligations or notices on a specific document requires that it be returned.

REPORT DOCUMENTATION PAGE

Form Approved
OMB No 0704 0188

1. AGENCY USE ONLY *(Leave blank)*

2. REPORT DATE
15 June 1993

3. REPORT TYPE AND DATES COVERED
Scientific Report No. 1

4. TITLE AND SUBTITLE
Penetrating Radiation Environment and Effects Study

5. FUNDING NUMBERS
F19628-90-C-0103
PE 62101F
PR 7601
TA 22
WU LD

6. AUTHOR(S)
H. D. Voss, W. L. Imhof, J. Mobilia, and E. E. Gaines

7. PERFORMING ORGANIZATION NAME(S) AND ADDRESS(ES)
Lockheed Palo Alto Research Laboratory
Space Science Laboratory
3251 Hanover Street
Palo Alto, CA 94304-1191

8. PERFORMING ORGANIZATION REPORT NUMBER

9. SPONSORING/MONITORING AGENCY NAME(S) AND ADDRESS(ES)
Phillips Laboratory
29 Randolph Road
Hanscom AFB, Ma. 01731-3010

Contract Manager : Kevin Ray Capt., USAF/GPSP

10. SPONSORING/MONITORING AGENCY REPORT NUMBER
PL-TR-93-2147

11. SUPPLEMENTARY NOTES

12a. DISTRIBUTION/AVAILABILITY STATEMENT
Approved for public release; distribution unlimited

12b. DISTRIBUTION CODE

13. ABSTRACT *(Maximum 200 words)*

This report summarizes some of the PREE achievements to date on data acquired from the Lockheed IMS-HI and SEP instruments on the CRRES satellite. The primary objectives of the PREE research are to, 1) inter-calibrate the ONR 307 instruments, 2) develop algorithms and software for understanding and modeling the radiation belts, 3) develop key parameters, and 4) study the dynamic radiation belt variations in the slot region and the outer belt. The new IMS-HI instrument performed well during the CRRES mission and has been inter-calibrated with the IMS-LO, SEP, and EPAS instruments. Much progress has been made in the development of key algorithms and software for mapping the electron, ion, and neutral flux. Energetic neutrals from the ring current have been observed directly and are an important low altitude and low latitude ionization source. Surveys of the medium energy (20-1000 keV) ion and neutral database indicate a sharp edge to the ring current flux which is not apparent in previous studies. The neutral flux is linked strongly with the low altitude edge of the ring current. To properly map the radiation belts and select key parameters a simple physical model was developed for the response of the magnetosphere to magnetic storms. The CRRES data indicate that the radiation belts including the inner belt are strongly modified during a sudden commencement (SC) on the order of several minutes. This momentary compression results in a net acceleration and transport of particles to low L in violation of the third invariant For the 24 March 1991 magnetic storm the magnetopause is inferred to have penetrated to L ~ 3.0 resulting in the possible establishment of the " new inner belt".

14. SUBJECT TERMS
Ions, Neutrals, Radiation Belts, Geomagnetic Storms, Acceleration

15. NUMBER OF PAGES
84

16. PRICE CODE

17. SECURITY CLASSIFICATION OF REPORT
Unclassified

18. SECURITY CLASSIFICATION OF THIS PAGE
Unclassified

19. SECURITY CLASSIFICATION OF ABSTRACT
Unclassified

20. LIMITATION OF ABSTRACT
SAR

Contents

1. Introduction 1
2. Experiment and Data 3
    2.1 Medium Energy Ion Mass Spectrometer (IMS-HI) 3
    2.2 Spectrometer for Electrons and Protons (SEP) 5
3. Progress and Current Activities 7
    3.1 Intercalibrations 7
    3.2 Neutral Atoms from the Ring Current 13
    3.3 Radiation Belt Modeling 16
        3.3.1 Model Description 16
        3.3.2 Generation of the IMS-HI Database 17
        3.3.3 IMS-HI Radiation Belt Model 19
    3.4 Magnetic Storm Dynamics 23
        3.4.1 Wave Particle Interactions 23
        3.4.2 Particle Transport and Acceleration during a Sudden Commencement 23
        3.4.3 Simulation of the Radiation Belt Electron Bursts 27
    3.5 Radiation Belt Acceleration and Transport 33
4. Future Plans 40
5. References 46
Appendix 1 IMS-HI Instrument Paper 48
Appendix 2 SEP Instrument Paper 53
Appendix 3 Neutral Atom Paper 58
Appendix 4 Abstracts 71

Figures

Figure 1 Illustration of the CRRES orbit plane with respect to the relevant magnetospheric particle regions 2

Figure 2 The principle of operation for IMS-HI 4

Figure 3 SEP Instrument Design 6

Figure 4a. IMS-HI Color Mode 0 survey plot for orbit 587 8
Figure 4b. IMS-HI Color Mode 1 survey plot for orbit 587 9

Figure 5 Flux line plots of H^+, He^+, and O^+ for orbit 587 10

Figure 6 Example of intercalibration of IMS-HI with IMS-LO 11

Figure 7 Example of intercalibration of IMS-HI with SEP 11

Figure 8 Intercalibration for protons with the EPAS, PROTEL, and GOES instruments....12

Figure 9 Energetic neutral atoms in the radiation belts 14

Figure 10 Mass spectrogram from IMS-HI detector 2 in the low altitude ion belt 15

Figure 11 Outline of IMS-HI data processing 18

Figure 12a Mass spectrum plot from the IMS-HI detectors 20
Figure 12b Line plot of Mode 1 data from the IMS-HI detectors 21

Figure 13 Summary display for the IMS-HI radiation belt Static Model 22

Figure 14 The IMS-HI instrument differential ion flux for 18 keV and 56 keV H^+, the ULF wave is observed in the magnetometer data (upper panel) and 18 keV proton (lower panel) channel 24

Figure 15 The association of B_z activity with 18 keV protons 24

Figure 16 Strong injected electron flux observed by IMS-HI during the 24 March 1991 magnetic storm onset 25

Figure 17 Greater than 50 MeV proton peak observed in the neutral detector about 35 s before the large electron peak. 26

Figure 18 SEP instrument response to the slot region injection event of 24 March 1991. The upper panel is for the E detector and the lower panel for the Anti-scintillator shield. 28

Figure 19 Monte Carlo simulation of the L=2.5 injection of energetic electrons (inset) and the SEP A detector 29

Figure 20 Simulation of the longitude interval of injection (lower panel) compared to the SEP E1 detector data. 30

Figure 21 Pitch angle sensitivity simulation 31

Figure 22 Simulation of the energy spectrum and pitch angle spread for injected electrons at L=2.5 32

Figure 23 Tsyganenko model for Kp > 5 during the CRRES injection event 34

Figure 24 Field line trace of a dynamic magnetosphere using an image dipole 36

Figure 25 CRRES magnetic field data during the 25 March 1991 sudden commencement 37

Figure 26 Approximate shift of particle drift orbits during a magnetic compression due to an image dipole 38

Figure 27 Standoff distance vs. time based on the image dipole compression of the magnetosphere. 41

Figure 28 Magnetic field line displacement during a sudden commencement 42

Figure 29 Magnetic field compression (acceleration) factor during a large sudden commencement 43

Figure 30 Constant B drift contours for particles during various stages of the compression event 44

Figure 31 Model of acceleration and injection of > 10 MeV electrons, protons, and alphas into the radiation belt slot region during a sudden commencement. 45

Tables

Table 1 IMS-HI Specifications 4

Table 2 SEP Specifications 6

1. Introduction

The purpose of this research activity is to improve our understanding of the Earth's radiation belts in the energy range > 18 keV. At present, the dynamics of the radiation belts are only poorly understood. This is exemplified in the unexpected appearance of a new inner belt (Mullen et al., 1991 and Gussenhoven et al., 1991) and the injection of > 10 MeV particles into the slot region (Vampola and Korth, 1992; Blake et al., 1992; Voss et al. 1992a) at the time of the 24 March 1991 storm. What the data show (Gussenhoven et al., 1991) is that, depending on orbit, both the existing proton and electron models can give large errors in dose that can compromise space system performance and lifetime. The Combined Release and Radiation Effects Satellite (CRRES) is overcoming this problem by making state-of-the-art measurements in the relevant magnetospheric particle trapping and precipitation regions as illustrated in Figure 1.

Models exist for the radiation belt environment, but certain important features such as the energetic neutral and ion mass component are not well known. The belts are also quite variable in regard to intensity, energy, and composition. Large particle doses can result from solar particle events and these occur in a somewhat random and unpredictable manner. Therefore, for an accurate knowledge of the radiation environment in space, it is necessary to perform in situ measurements at the times and positions of concern. Such measurements have been performed on the CRRES satellite and permit the development of a comprehensive database.

The IMS-HI instrument (ONR 307-8-3) on the CRRES satellite (see Appendix I) has the unique features that it is able to measure mass and energy (18 keV < E < 2 MeV) simultaneously with 100% duty cycle, has a large geometrical factor and count rate dynamic range, and has good background rejection because the ion mass peak to valley ratio is measured. The neutral detector in the IMS-HI instrument is providing the first neutral atom model of the Earth's radiation belts. The ONR 307-3 Spectrometer for Electrons and Protons (SEP) measures with fine pitch-angle resolution the flux of energetic electrons in the energy range of 20-keV to 5 MeV and flux of energetic protons in the energy range 500 keV to 100 MeV.

To understand and model the radiation belts it is essential that the geometry and dynamics of the belts be properly taken into consideration. The first area of investigation was to intercalibrate the IMS-HI instrument with ions from the IMS-LO instrument and with protons from the SEP instrument. Limited intercalibrations were also made with the AFGL EPAS and Protel instruments during the 24 March 1991 storm period. Because the IMS-HI neutral atom capability was unique to the CRRES satellite, the data near perigee were investigated first to "intercalibrate" with previous low-altitude satellite measurements (Voss et al., 1992c).

A series of computer programs were then developed as outlined in Section 3.3 to process the IMS-HI data for a comprehensive radiation belt model. Of particular concern in these models is

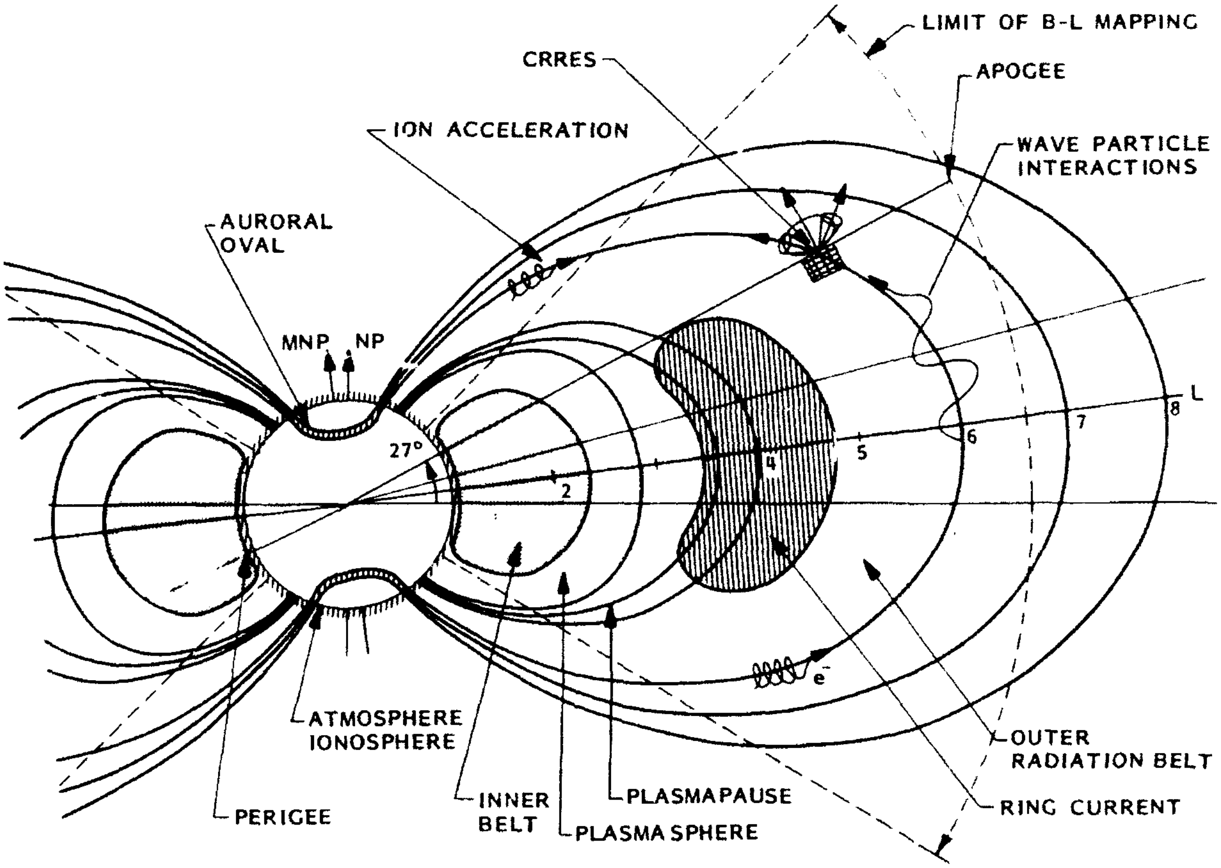

Figure 1 CRRES orbit plane with respect to the relevant magnetospheric particle regions

the rejection of background counts and the organization of the data according to location and magnetic storm dynamics. It has become very apparent in the CRRES data that storm time activity causes major transport and injection of particles in radiation belts. These topics are discussed in Sections 3.4 and 3.5.

Of particular excitement is the preliminary finding that the magnetic shock on the magnetosphere by a large storm can penetrate down to L-shells as low as 2.0. A simple model using an image dipole moving toward the earth is used to simulate the shock. The data from this simple model can explain much of the observed CRRES data for the 24 March event 1991. This transport and acceleration mechanism is crucial to the proper modeling of the radiation belts.

2.0 Experiment and Data

2.1 Medium Energy Ion Mass Spectrometer (IMS-HI)

The primary objective of the medium energy ion mass spectrometer (ONR 307-8-3) on the CRRES satellite is to obtain the necessary data to construct models of the energetic ion (10 to 2000 keV-AMU/q^2) and neutral atom (10 to 1500 keV) environment of the Earth's radiation belts. The spectrometer (Voss et al., 1992b) measures the energetic ion composition, energy spectrum, charge, and pitch angle distribution with good mass, temporal, and spatial resolution. The ion rejection in the neutral detector is <100 MeV-AMU/q^2. The instrument principle of operation is based on ion momentum separation in a 7 kG magnetic field followed by energy and mass defect analysis using an array of cooled silicon solid-state detectors. The architecture is parallel with simultaneous mass and energy analysis at relatively high sensitivity (100% duty cycle). The instrument is performing as designed in orbit with the major groups of hydrogen, helium, oxygen, and neutrals clearly resolved.

The conceptual instrument design is given in Figure 2 and the specifications are given in Table 1. An entrance collimator defines the ion beam angular resolution using a series of rectangular baffles and includes a broom magnet to reject electrons with energy less than 1 MeV. A 7-kG magnetic field then disperses the collimated ions onto a set of six passively cooled (-40°C) silicon surface barrier detectors. The energy range, which varies with ion species, is approximately EM/q^2= 10-2000 keV-AMU/q^2. A seventh sensor, located directly in line with the collimator, measures energetic neutrals.

Solid-state detectors 1-7 are located at angle, θ, of 40°, 65°, 90°, 115°, 140° 162.5°, and 180°, respectively. Solid-state detectors 1-6 are n-type silicon having either 20 or 40 micrograms cm^{-2} of gold surface deposit. The neutral detector is of p-type silicon to improve light rejection and radiation damage sensitivity and has 20 micrograms cm^{-2} of aluminum surface deposit. The energy loss in surface barrier windows for H, He, and O is discussed by Voss, 1982. The mass

Table 1 Medium Energy Ion Mass Spectrometer (IMS-HI) Specifications

Analyzer	7KG magnet(q^2/m) and Mass Defect
Sensors	Silicon Surface Barrier (-55°C)
Number of Imaging Sensors	7 at 0.5 cm^2 each
Look Direction from Spin Axis	75°
Particles and Energy Range:	
Neutrals	10-1500 keV
Protons	15-2000 keV
Helium	10-500 keV
Oxygen	20-130 keV
Oxygen++	20-500 keV
Other Ions	E>20 keV
Number of Differential Mass Channels	64
Number of High Rate Mass Channels	4
Number of Differential Energy Channels	6
Pitch Angle Resolution	4° FWHM
Geometric Factor	10^{-2} - 10^{-3} cm^2
Duty Cycle	100%

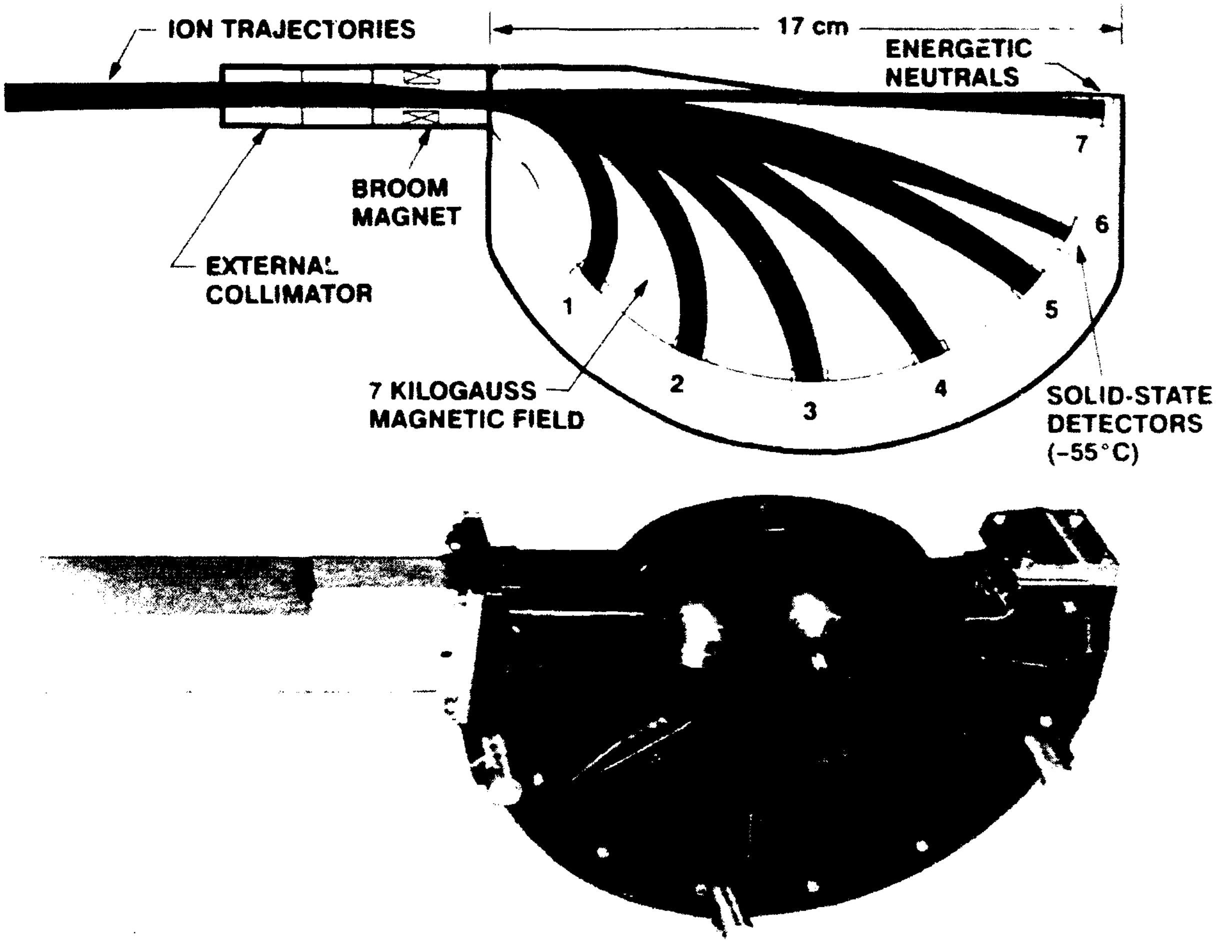

Figure 2 The principle of operation for IMS-HI

defect in solid-state detectors results from energy loss of non-ionizing nuclear collisions within the solid that reduce the efficiency of electronic signal genration. The mass defect increases with atomic weight of the nuclei in a well understood way and causes further mass separation, with commensurate energy scatter, for the heavier nuclei.

Two basic modes of instrument operation are used: Mass Lock and Mass Scan. In the Mass Scan mode each of the seven solid-state detectors is pulse height analyzed into 256 levels of which 64 intervals are accumulated in memory and read out every eight seconds. This mode is used to scan all mass peaks within the range of the sensor relative to the background continuum. In the Mass lock mode, each of the seven solid-state sensors is pulse height analyzed into 256 levels, of which four intervals (typically four ions) are accumulated in memory and read out every one-half second. This mode is used for making rapid spectral snapshots of four ions as a function of pitch angle. Baseline operation of the instrument was a toggle mode (32.768 seconds) between Mass Lock mode and the Mass Scan mode. Additional information on the IMS-HI instrument is given in Appendix I.

2.2 Spectrometer for Electrons and Protons (SEP)

The SEP design is based on the heavily successful SC-3 spectrometer (Reagan et al., 1981) flown on the SCATHA mission. Unlike the single-detector system used on SCATHA, SEP consists of three solid-state particle spectrometers oriented at 40°, 60°, 80° from the spacecraft spin axis. A cross-sectional view of one of the telescopes is shown in Figure. 3. Each spectrometer has four detector elements labeled A, D, E, and E'. Various logic combinations of the four detector elements in each spectrometer are used to determine the particle types and energy ranges which are measured sequentially. The operational modes of each telescope are individually commandable.

Each of the three identical SEP particle telescopes has a high-resolution, 3° (FWHM) field of view provided by a long collimator (20 cm) containing 10 baffles. The collimators are identical to the ones used on the SC-3 instrument (Reagan et al., 1981) providing an instrument geometric factor of ~3×10^{-3} cm^2 sr. For the 80° and 60° telescopes, measurements over 12 energy channels are obtained every 0.25 seconds with a dead time of 2 millisecond. Due to telemetry restrictions, the 40° telescope accumulates for 0.5 seconds with a dead time of 4 millisecond. Specifications for the SEP instrument are given in Table 2. Additional instrument details are given in the SEP instrument paper by Nightingale et al., 1992 (Appendix II).

Table 2 SEP Specifications

Mode	Sensor A Energy range, MeV	Sensor A Width, MeV	Sensor B Energy range, MeV	Sensor B Width, MeV	Sensor C Energy range, MeV	Sensor C Width, MeV
Electron 1	0.042-.324	0.0235	0.042-0.336	0.0245	0.041-.313	0.0227
Electron 2	0.164-4.93	0.397	0.171-5.12	0.413	0.170-5.11	0.412
Proton 1	0.875-6.60	0.478	0.916-6.7	0.482	0.920-6.8	0.490
Proton 2	2.5-38.7	3.01	2.2-33.7	2.62	2.0-30.4	2.37
Proton 3	35.8-80.2	3.7	31.2-69.9	3.22	28.2-63.1	2.91
Proton 4	45-94	4.08	45-105	5.00	45-110	5.42
Alphas	6.8-24	1.43	6.9-24.3	1.45	7.00-24	1.47

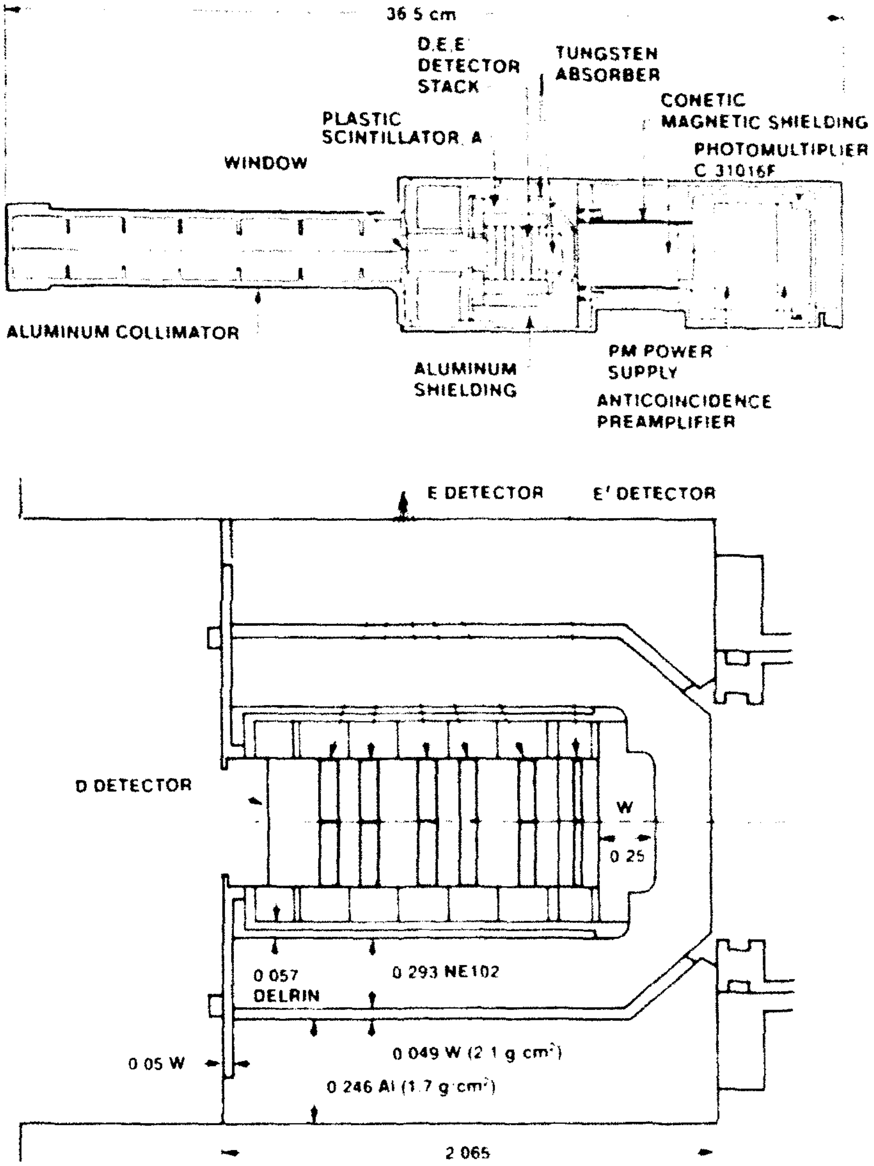

Figure 3 SEP Instrument Design

3. Progress and Current Activities

3.1 Intercalibrations

The quality of the measurements of the radiation environment directly affects the precision and reliability of studies utilizing the data. A continuing effort has been made to intercalibrate the various CRRES instruments in orbit. Potential problems have been found which include scattering in collimators and backgrounds due to bremsstrahlung, pile-up, and penetrating radiation. Unlike geostationary orbits, the CRRES orbit environment is demanding on the instrument hardware and therefore new and improved algorithms were developed to derive comprehensive flux measurements over all regions of the radiation belts.

An example of the IMS-HI survey plots for orbit 587 is shown in Figure 4a. Only data from the 64 channel mass scan mode is shown. For detector 1 the 18 keV proton peak in the center mass channels is prominent. The mass channels covered for protons are numbers 38-42. Adjacent to this proton band, the penetrating background continuum is observed in all mass channels. The actual 18 keV H^+ flux is thus the counts in the peak above the background continuum. Although this is obvious the IMS-HI instrument provides this added information for validating the ion flux. The more common broom-magnet spectrometers are unable to differentiate between background.

For $L<3$, on both ends of the plot, the continuum is quite variable due to the inner belt and sudden commencement (0342 UT) associated particle penetration, yet no ion peak is observed in this region indicating the rapid drop off of ion flux and the importance of the peak to valley ratio background algorithms. For detector 2 hydrogen is located in mass channels, 58-63 and He^+ is located in mass channels 33-35. Again the continuum is subtracted off of the peak count rates.

For the higher energy detectors the background subtraction algorithm is a combination of sensors. For example the proton flux in detector 6 is given by

$$\text{Det 5 flux} = 0.14\left[\sum_{\text{ch }54}^{63} - \text{ch63 of Det 5}\right] + 0.19\left[\sum_{\text{ch }54}^{62} \text{of Det 5} - \sum_{\text{ch }43}^{52} \text{of Det 5}\right] \quad (1)$$

A series of orbital flux profiles using the background subtraction is given in Figure 5 for orbit 587. For protons the L dependence of the various energies is apparent with the higher energies peaking at low L shells. The rapid drop off of 18 keV flux by several orders of magnitude at $L \sim 3.0$ is surprising and indicates a strong loss process in this region. The enhanced flux of 1.7 MeV and $E > 50$ MeV protons is consistent with the on-going solar proton event. For He^+ the L dependence is in the opposite direction of the protons with the higher energies peaking at the higher L shells.

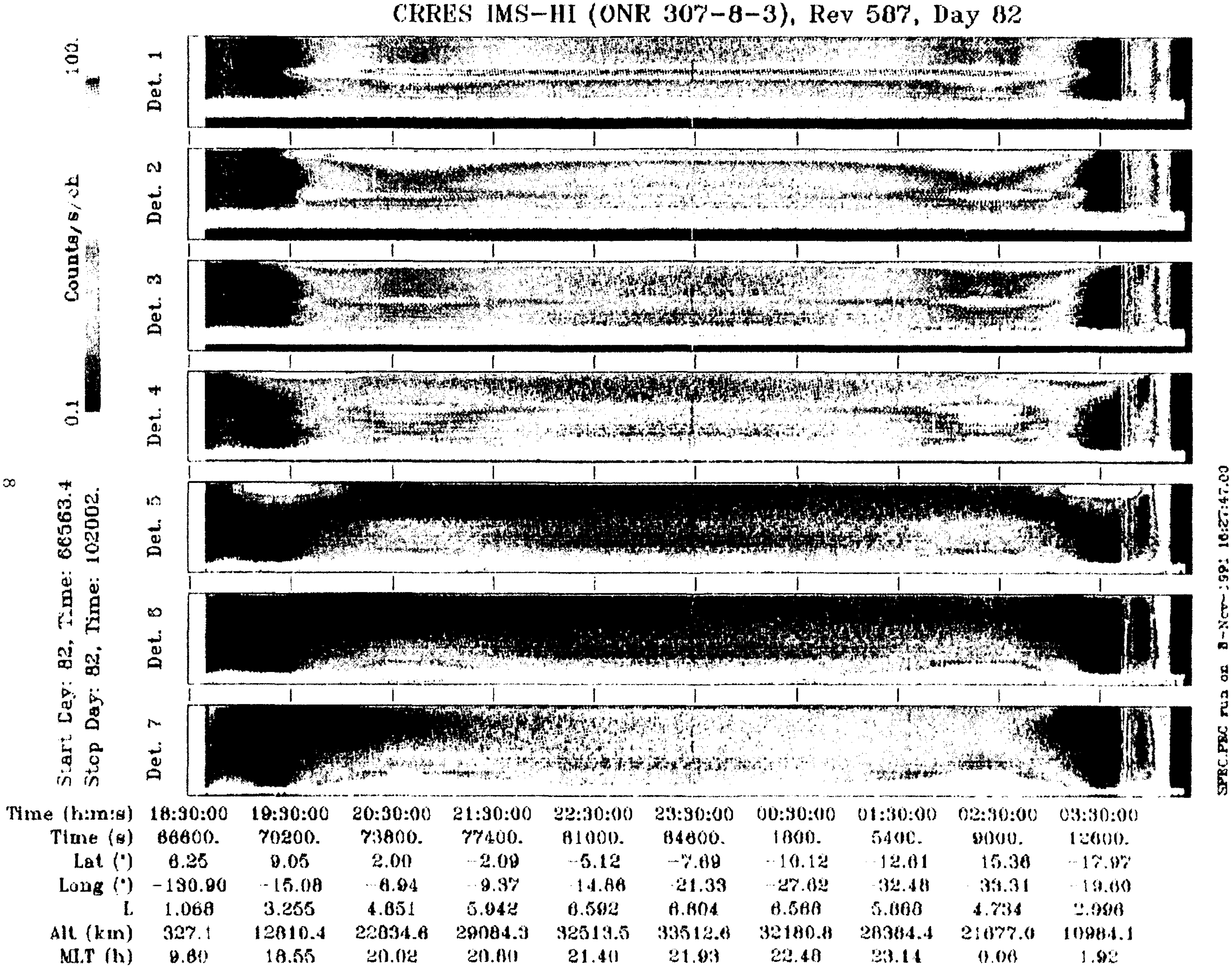

Figure 4a. IMS HI Color Mode 0 survey plot for orbit 587

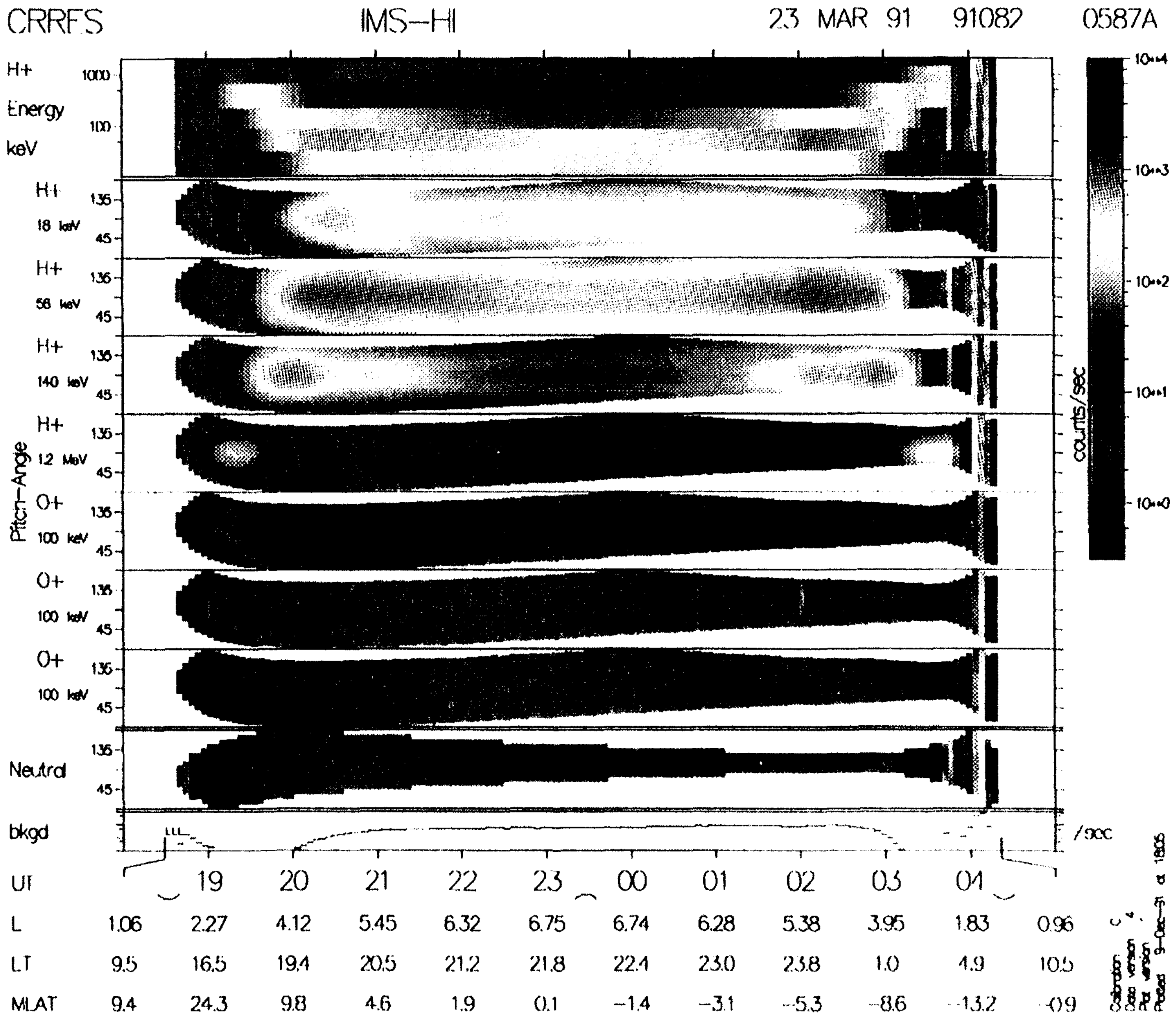

Figure 4b. IMS HI Color Mode I survey plot for orbit 587

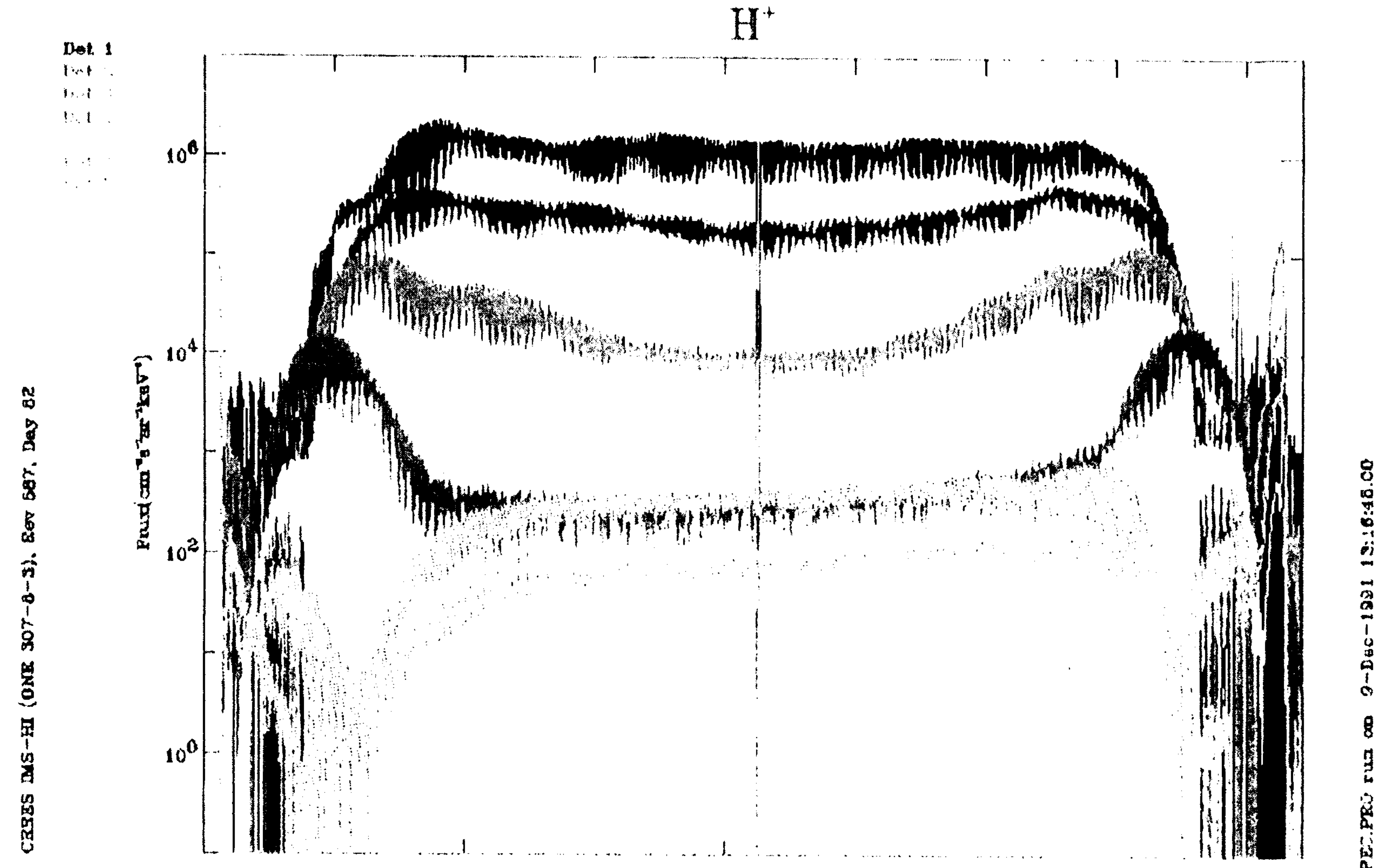

Time (hh:mm:ss)	18:30:00	19:40:00	20:50:00	22:00:00	23:10:00	00:20:00	01:30:00	02:40:00	03:50:00
Time (s)	66600.	70800.	75000.	79200.	83400.	1200.	5400.	9600.	13800.
Lat (°)	8.36	7.47	0.46	-3.68	-8.66	-9.73	-13.61	-16.65	-17.11
Long (°)	-130.90	-12.04	-7.18	-11.91	-19.14	-26.03	-32.48	-32.62	-2.51
L	1.008	3.559	5.266	6.321	6.704	6.638	5.000	4.488	2.250
Alt (km)	387.1	14813.5	26278.1	31118.6	33488.6	32567.2	28384.4	20816.1	6846.6
MLT (h)	9.60	18.91	20.32	21.11	21.76	22.39	23.14	0.27	3.37

Figure 5   Flux line plots of H+, He+, and O+ for orbit 587

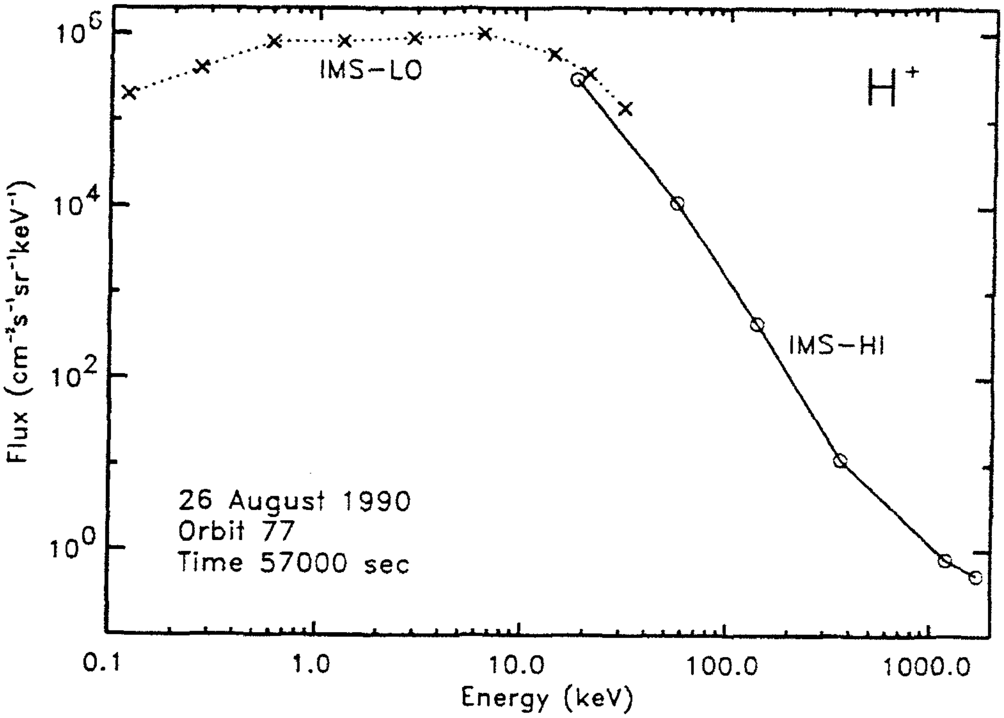

Figure 6 Example of intercalibration of IMS-HI with IMS-LO

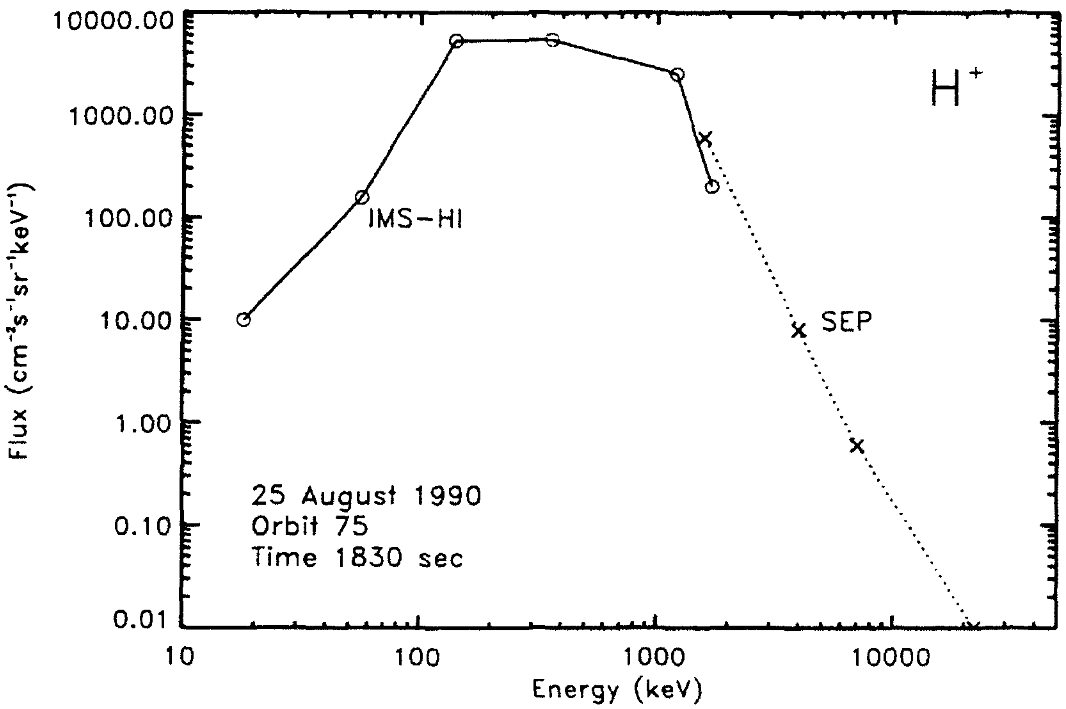

Figure 7 Example of intercalibration of IMS-HI with SEP

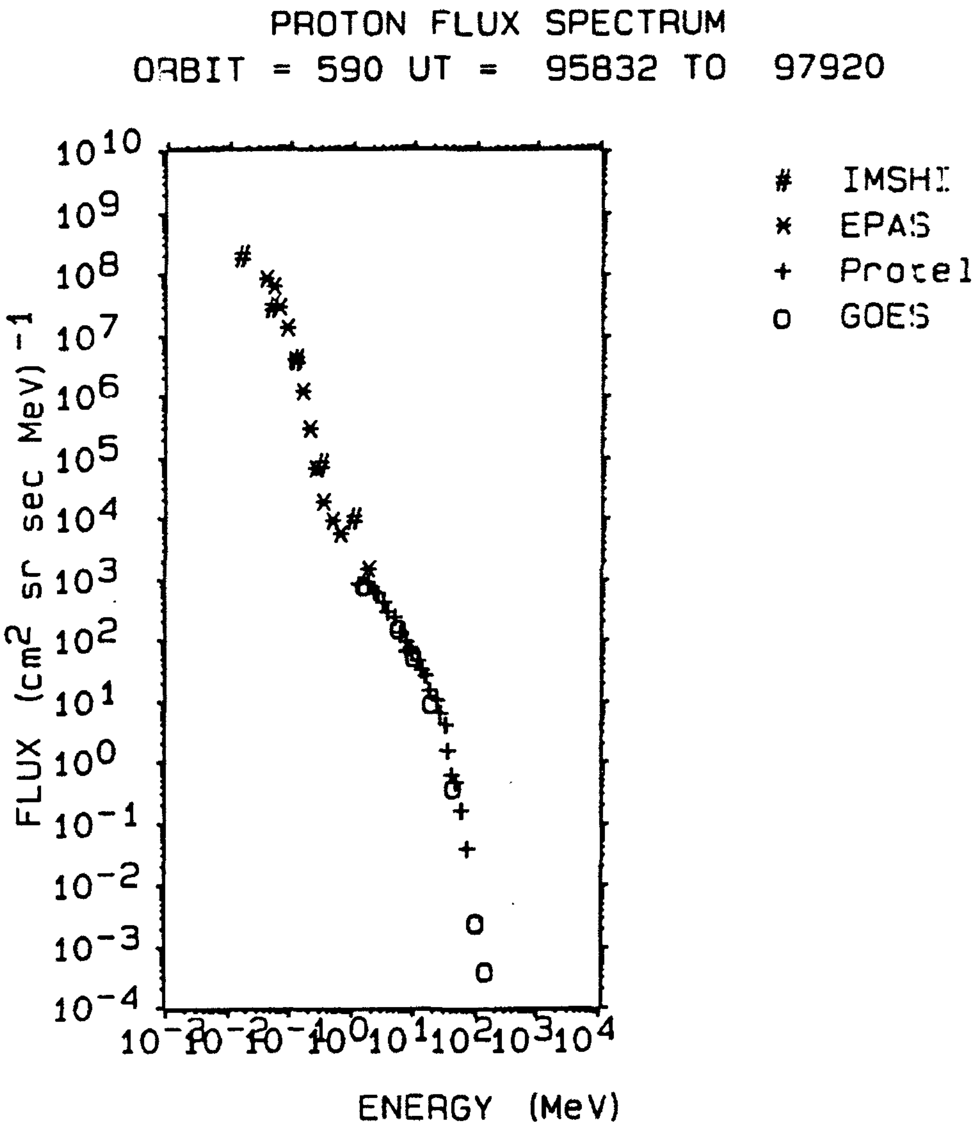

Figure 8 Intercalibration for protons with the EPAS, PROTEL, and GOES instruments

The IMS-HI instrument was intercalibrated with IMS-LO instrument for energetic protons. The IMS-HI 18 keV channel overlaps in energy with two of the IMS-LO channels. Both instruments have narrow fields-of-views. In general, the instruments agreed well in hydrogen flux measurements. An example of the typical overlap is shown in the spectrum of Figure 6. The IMS-HI instrument was intercalibrated with the SEP instrument for energetic protons in energy range 1 to 2 MeV. An example of the typical overlap is shown in the spectrum of Figure 7 for orbit 75.

Several periods of time were used to intercalibrate the IMS-HI with the EPAS and Protel instruments. An example of this intercalibration is shown in Figure 8. In this case the agreement is good suggesting that the geometric factors and energy channel calibrations have been properly taken into account. However, when backgrounds are high (e.g. $L<3$) it appears that the EPAS instrument gives fluxes that are up to several orders of magnitude higher than from the IMS-HI. In fact, the IMS-HI instrument data indicates that there is a strong energy dependent cutoff of ions in the slot region as indicated in Figures 4 and 5.

3.2 Neutral Atoms from the Ring Current

Modeling of the radiation belt protons and heavier ions requires an understanding of the neutral components. Energetic neutrals are the consequence of the change exchange process of radiation belt ions with thermal ions, and vary according to the importance of this loss process. Because the neutrals are not restricted to the magnetic field they can rapidly fill all of the magnetosphere. Neutral atoms can therefore provide a mapping of the internal composition, spatial geometry, and temporal changes of the ring current, weighted by the appropriate cross sections and neutral hydrogen density; it provides a powerful method of studying the magnetosphere (Roeloff et al., 1985, Hsieh et al. 1992). Using the IMS-HI instrument on the CRRES satellite the first in-depth investigation of the neutral atom radiation environment is being conducted.

The source of energetic neutral atoms (ENA) at low altitudes is believed to be a double-charge-exchange process of ions originating in the ring current (Moritz, 1972; Tinsley, 1981) as shown in Figure 9. The trapped ions of the ring current, by charge exchange with thermal hydrogen atoms of the geocorona, become high velocity neutral atoms which are focused, for those directed toward the earth, in the equatorial atmosphere where they again become ions by ionization collisions. In principle the spin of the CRRES satellite and orbit motion can be used to "raster scan" a portion of the magnetosphere to obtain a neutral atom image. In practice, however, the duty cycle associated with the spinning of the satellite and the background of the radiation belts make this a difficult task from CRRES. The injected energetic neutrals at low altitudes produce the equatorial precipitation zone and a temporary low altitude ion belt between 200 and 1000 km as

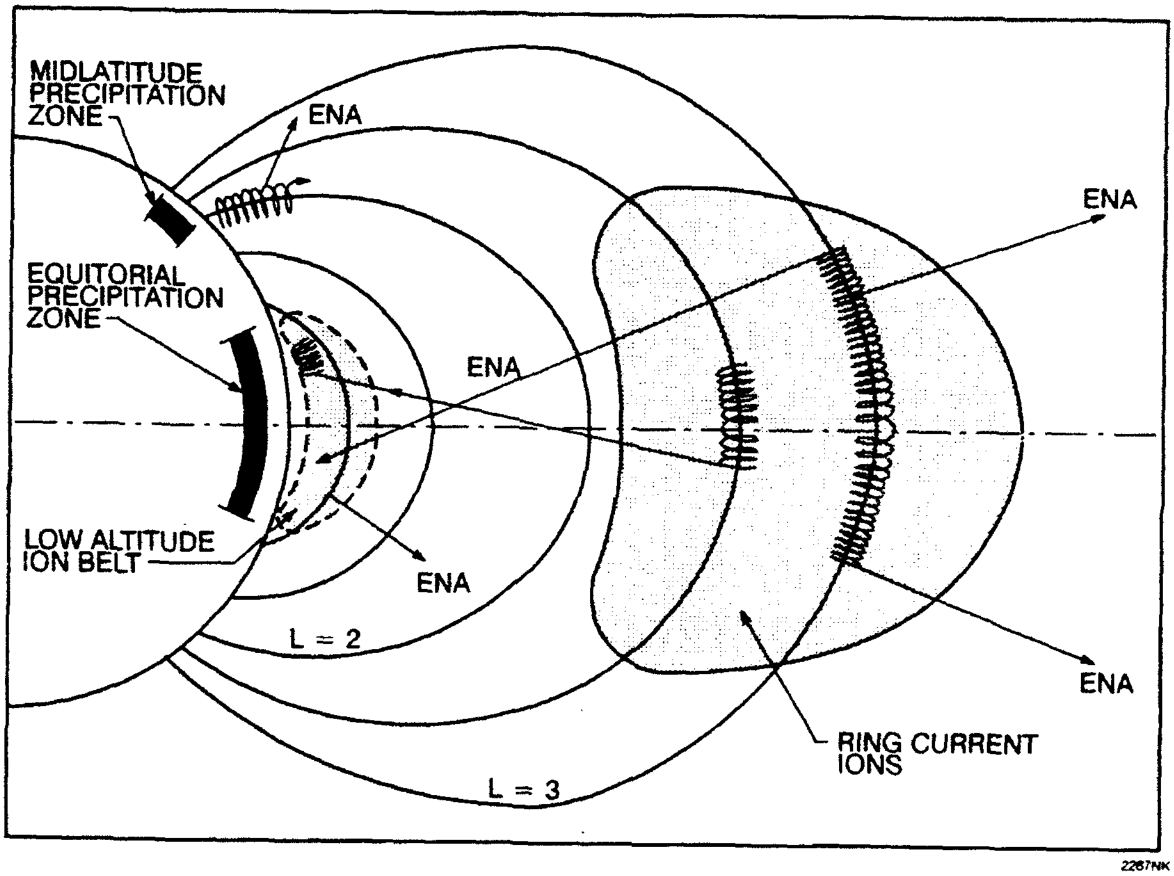

Figure 9 Energetic neutral atoms in the radiation belts

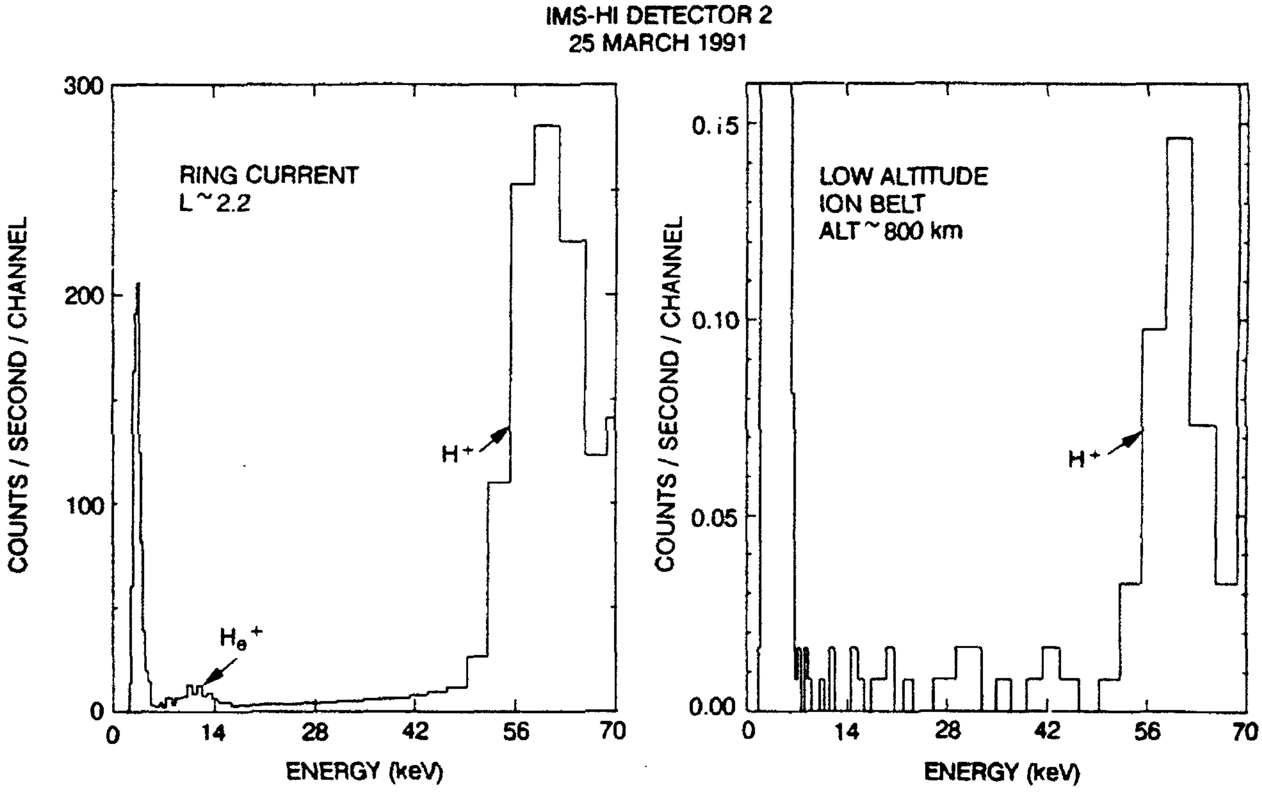

Figure 10 Mass spectrogram from IMS-HI detector 2 in the low altitude ion belt

illustrated in Figure 9.

Near perigee (<1000 km), when CRRES is below the inner belt, the IMS-HI instrument is able to directly view the ring current neutrals and ion composition of the low-altitude ion belt. Above the inner belt the IMS-HI instrument is able to make cross-sectional cuts of the ring current ion composition. About one day after the large magnetic storm of 24 March 1991 the ring current ions were observed to increase and move to lower altitudes. The ring current flux at this time extends down to L~2.0 and is dominated by hydrogen at E~60 keV. O^+, O^{++}, and He^+ are one to two orders of magnitude less in flux at these energies.

The ENA transported to low altitude is again charge exchanged by the atmosphere and temporarily becomes the low-altitude ion belt. Because the ions cannot support drift motion in much of the belt the loss rate is high. The steady-state ion population to first order is a mapping of the source composition multiplied by the appropriate atmospheric loss rates. A mass spectrogram of the low altitude ion belt for detector two is shown for the first time in Figure 10 for 25 March 1992. Also shown for comparison is the mass spectrogram of detector two near the inside edge of the ring current at L~ 2.2. At this time the prominent ion, inferred from the ring current ENA is H^+ at 60 keV. The average low-altitude hydrogen count rate is about 2000 times lower than the average count rate in the ring current for the IMS-HI spectrometer.

3.3 Radiation Belt Modeling

3.3.1 Model Description

The static version of the Empirical Model of medium energy ring current ion composition consist of a set of average equatorial energy and pitch-angle distributions of fluxes of H^+, He^+, and O^+ consistent with the IMS-LO data base (Collin et al., 1992). The distributions are binned by energy and pitch-angle with 7 energy bins covering the whole of the IMS-HI energy range, 18 keV/amu to 1.7 MeV/amu, and eighteen, 10°, pitch angle bins which cover the full range of 0° to 360°, allowing for pitch-angle asymmetry. The model contains a H^+, He^+, and O^+ distribution for each of a number of spatial regions. These regions are defined by dividing the equatorial plane into six local time sections of four hours in width and into six radial sections between L = 2.5 Re and L = 8.5 R_E each 1.0 R_E in width. Associated with each flux value is an estimate of its statistical uncertainty and for development purposes a measure of the background and number of data samples used to determine the flux value (Collin et al., 1992). The model can therefore be used to determine the average ion distributions away from the equatorial plane, assuming the absence of parallel electric fields and wave-particle interactions, by mapping the equatorial distributions down the field lines to the location of interest.

In addition to the medium energy ion composition model a similar model is used for energetic neutrals. In this case the neutrals are binned into four energy ranges (out of 64 energy channels) and into eighteen angular bins relative to the earth's geometry over 0 to 360°. Because the neutral flux is several orders of magnitudes less than the ring current ion flux the background must be validated for inclusion into the model.

3.3.2 Generation of IMS-HI Database

A schematic of the IMS-HI data processing is shown in Figure 11. The first stage of processing is to unpack and decode the data on the agency tapes and then write the data from each orbit to a group of files for each instrument together with ephemeris and magnetometer files. At this stage all data is in the form of counts and engineering units at the full resolution of the instrument. This forms the high resolution database (level 1) and is stored on optical disks.

In level 2 the IMS-HI instrument data is stripped from the optical disk file along with other selected parameters and binary compressed. From this file the computational burden is significantly reduced for the summary data base and level three processing. As indicated in Figure 11 level three processing has four formats: 1) Mode 0 color spectrograms of 64 channel mass (Figure 4a), 2) Mode 1 color pitch angle plots (Figure 4b), 3) Line plots/files of scaler data, and 4) at line plots of Mode 0 mass.

In level 4 processing four types of line plots are possible: mass spectrums plot up to seven detectors, (1A) pitch angle plot of 3 mass intervals (2A), mode 1 scales line plots, and 1 energy line plots of 3 mass intervals. An example of formats 1A is given in Figure 12a and of format 2 in Figure 12b.

Based on review of the level 3 and level 4 processing the level 5 summary database is being constructed. This IMS-HI Summary Data base is a compact, partially processed data base consisting of averages, over 131 seconds, of IMS-HI ion and neutral data sorted by energy and pitch angle. Supporting data include time, background count rate, status information, measured magnetic field and ephemeris information. The ion and neutral data are recorded as count rates in order to make the data base independent of revisions to instrument calibration with cross calibrations underway. Calibrations are applied to the count rates where the data base is accessed. The Summary Database is suitable for rapid retrieval of energy spectra, pitch angle distributions or survey and for the basis forms the statistical studies. An attempt has been made to keep the data base similar to the IMS-LO data base (Collin et al., 1992) so that the final Radiation Belt Model for IMS-HI will be consistent with the IMS-LO model. In level 6 processing the final IMS-HI Radiation Belt Model is formed. The model results are designed so that they can be compared with

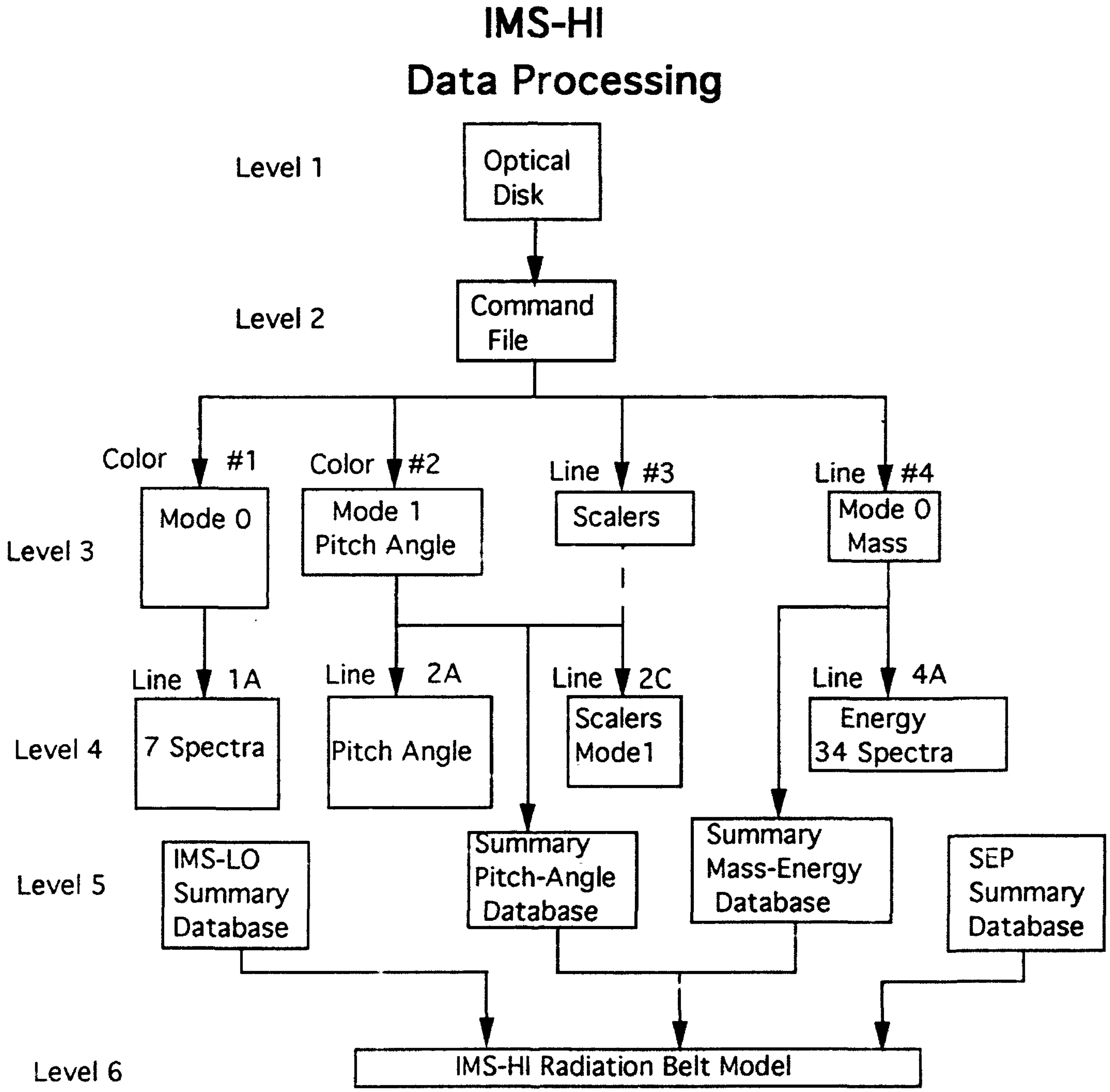

Figure 11 Outline of IMS-HI data processing

the IMS-LO and IMS-HI databases as well and for application of existing dose/shielding algorithms.

3.3.3 IMS-HI Radiation Belt Model

The IMS-HI Summary Data base can be used for both static and dynamic modeling. The model average equatorial distributions are constructed by accumulating and averaging equatorial distributions from many orbits. Similar to IMS-LO the data are binned by their energy and equatorial pitch-angle and sorted into ranges of L and local time. These distributions are mapped adiabatically from the satellite location to the equatorial plane. The mapping makes use of the modeled values of the local magnetic field strength and the minimum field on the same field line which are provided in the CRRES ephemeris files.

The quality of the data base is strongly dependent on an understanding of contamination sources, especially for the neutral atom database. The capability of IMS-HI to measure the peak to valley ratio in each spectrometer mass channel eliminates background to a great degree (see Section 3.1). In addition a quality factor (1 to 10) based on the signal to background ratio is given to each interval of time so that data quality can be tracked. Furthermore, each orbit's summary data will be checked manually with the high resolution color spectrogram data to verify that the data quality is valid. With the background rejection accurate data should be obtained over the whole orbit.

Figure 13 is a condensed display of data for the static model. The layout is based on a portion of the Summary Data base and is consistent with the IMS-LO database. The top panel contains energy spectra, averaged over pitch angle for H^+, He^+, and O^+. The bottom panels contain H^+, He^+, and O^+ pitch angle distributions at selected energy bands. These panels are divided horizontally by bold black vertical lines into six broad strips which correspond to six ranges of L. The left most of the broad strips, for example, corresponds to divided strips corresponding to a magnetic local time interval. Each of the narrow strips displays the average equatorial energy spectral and pitch-angle distributions for its own local time L range. As in IMS-LO data base the energy spectra in the top panel (or pitch angle in the lower panels) can be referenced to the equatorial plane with radii of 2, 3, 4, 5, 6, at 7 R_e.

The static model can be averaged over any interval during the CRRES lifetime. For the whole of the CRRES lifetime the model represents a fairly active time period during solar maximum. The use of the static model forms the basis for dynamic modeling by binning the static model according to various magnetic disturbance indices.

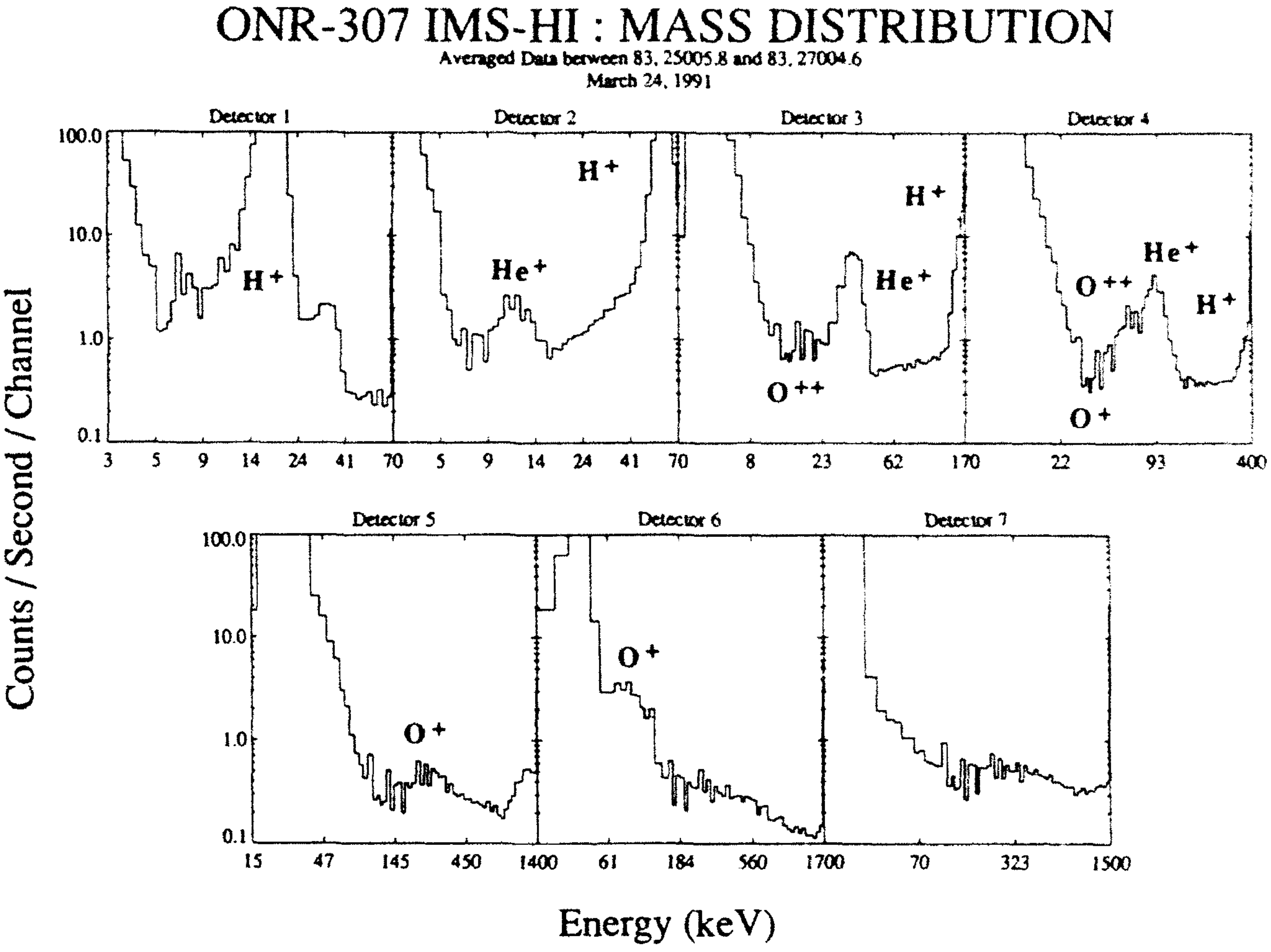
ONR-307 IMS-HI : MASS DISTRIBUTION

Averaged Data between 83, 25005.8 and 83, 27004.6

March 24, 1991

Detector 1

Detector 2

Detector 3

Detector 4

Detector 5

Detector 6

Detector 7

Figure 12a Mass spectrum plot from the IMS-HI detectors

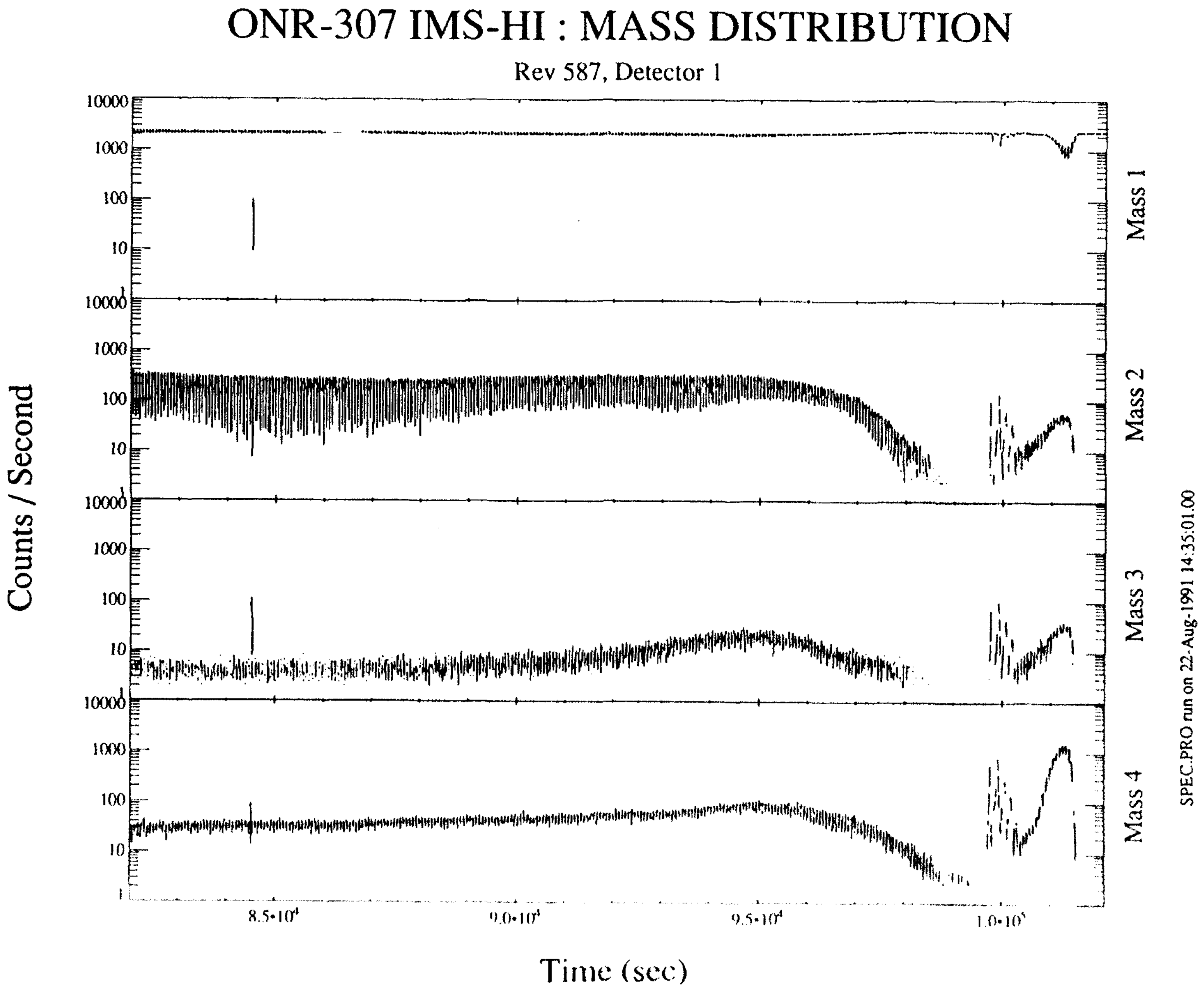

Figure 12b Line plot of Mode 1 data from the IMS-HI detectors

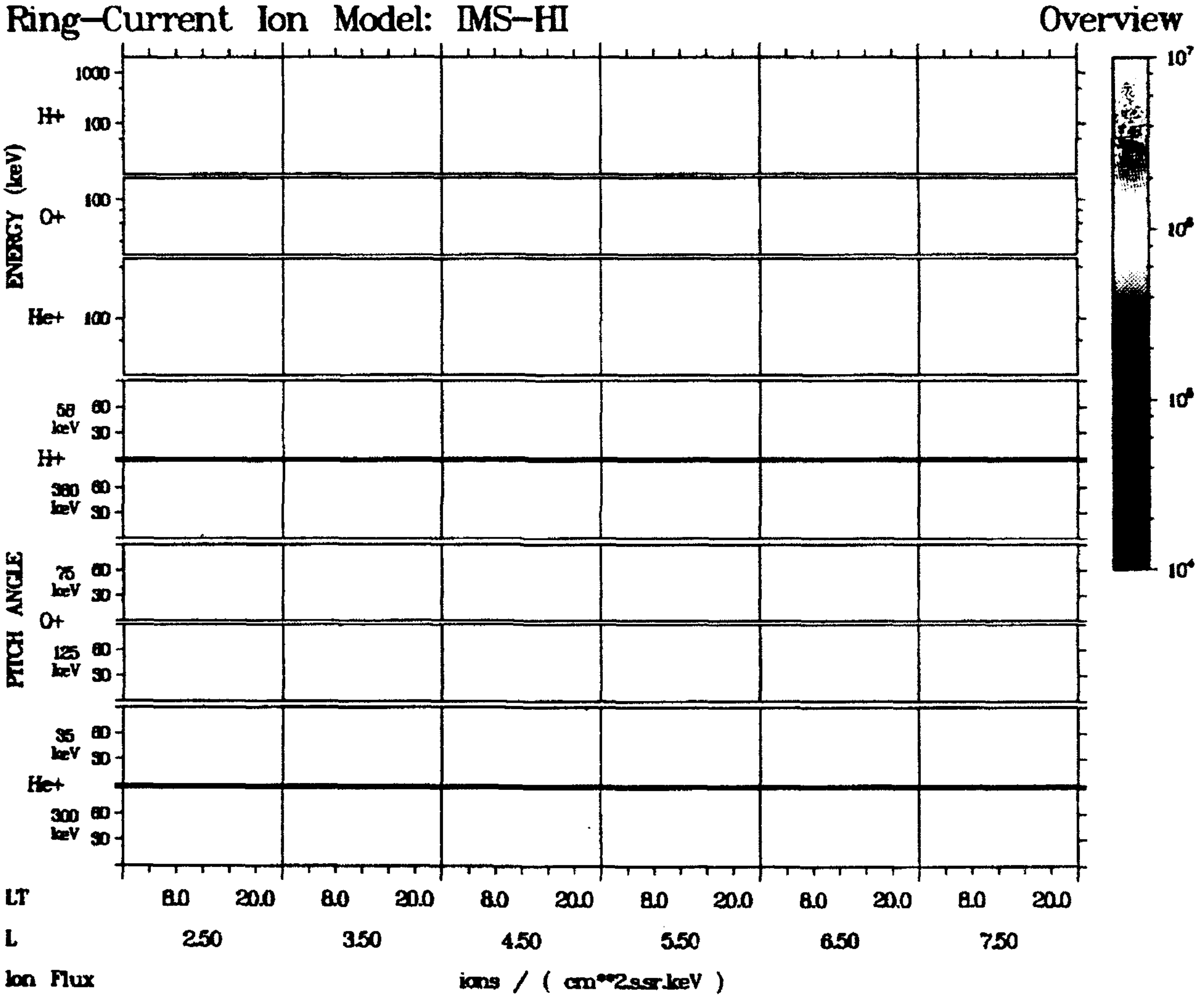

Figure 13 Summary display for the IMS-HI radiation belt Static Model

3.4 Magnetic Storm Dynamics

The 26 August 1990 and 24 March 1991 Magnetic storms were investigated using the IMS-HI and SEP instruments on the CRRES satellite. These storms show considerable variation and variation with other events (e.g. Gloeckler et al., 1985 and McEntire et al., 1985). By understanding the injection, acceleration, and transport within the radiation belts the assumptions for modeling algorithms can be improved. The best models are usually based on parameters which have good physical significance.

For the 26 August 1990 magnetic storm the Kp reached 7-. At the time of the sudden commencement CRRES was near apogee in the dawn sector. For 24 March 1991 the Kp reached 9-. At the time of the sudden commencement CRRES was in the slot region at L~2.5 at about 0300 hr UT.

3.4.1 Wave Particle Interactions

Of particular interest is the sensitivity of the differential ion flux measurements of the IMS-HI instrument to waves. In Figure 14, a 6 minute period ULF wave , that is observed prior to the sudden commencement, is also observed in the 18 keV proton channel. The resonant interaction is such that at 56 keV no interaction is observed. The small scale fluctuations in the 18 keV and 56 keV channels are associated with spin modulation. At the time of the sudden commencement the magnetic flux density is increased due to the magnetic compression and the particle flux is likewise increased in accordance with Louisville's theorem. Another association of B_Z wave activity with 18 keV protons during this storm event is shown in Figure 15. Wave-particle interaction observed with the CRRES energetic electron and electric field experiments are currently being investigated by Dr. W.L. Imhof and will be reported in a later publication.

3.4.2 Particle Transport and MeV Acceleration during a Sudden Commencement.

Simultaneous injection/acceleration of >10 MeV particles at L~2.5 with a sudden commencement is surprising and suggests that an unexpected acceleration mechanism is active in that region. Between 0342 and 0354 UT the particle instruments on the CRRES satellite measured impulsive bursts of >10 MeV electrons, protons, and alphas in the slot region (2.1 <L<2.5) near the equator at 0300 hours MLT (Mullen et al., 1991; Vampola and Korth, 1992; Blake et al., 1992; and Voss et al., 1992a). The electron bursts (Figure 16) are consistent with drift echoes of about 15 MeV electrons while the proton groups are consistent with drift echoes of >20 MeV protons. No medium energy 18 keV < E < 1.5 MeV ion bursts were observed. However, in the IMS-HI

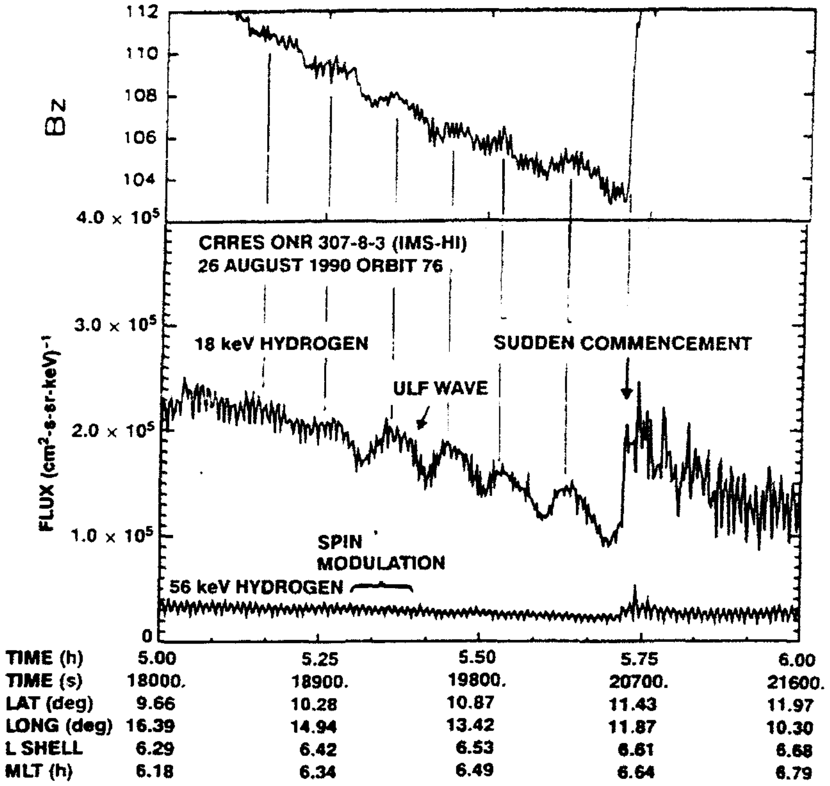

Figure 14 The IMS-HI instrument differential ion flux for 18 keV and 56 keV H+, the ULF wave is observed in the magnetometer data (upper panel) and 18 keV proton (lower panel) channel

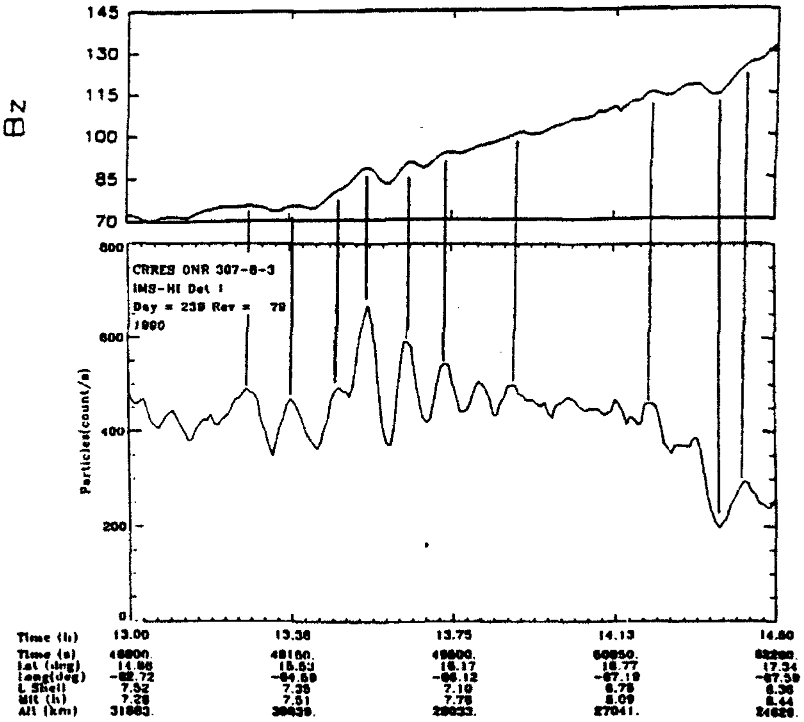

Figure 15 The association of B_Z activity with 18 keV protons

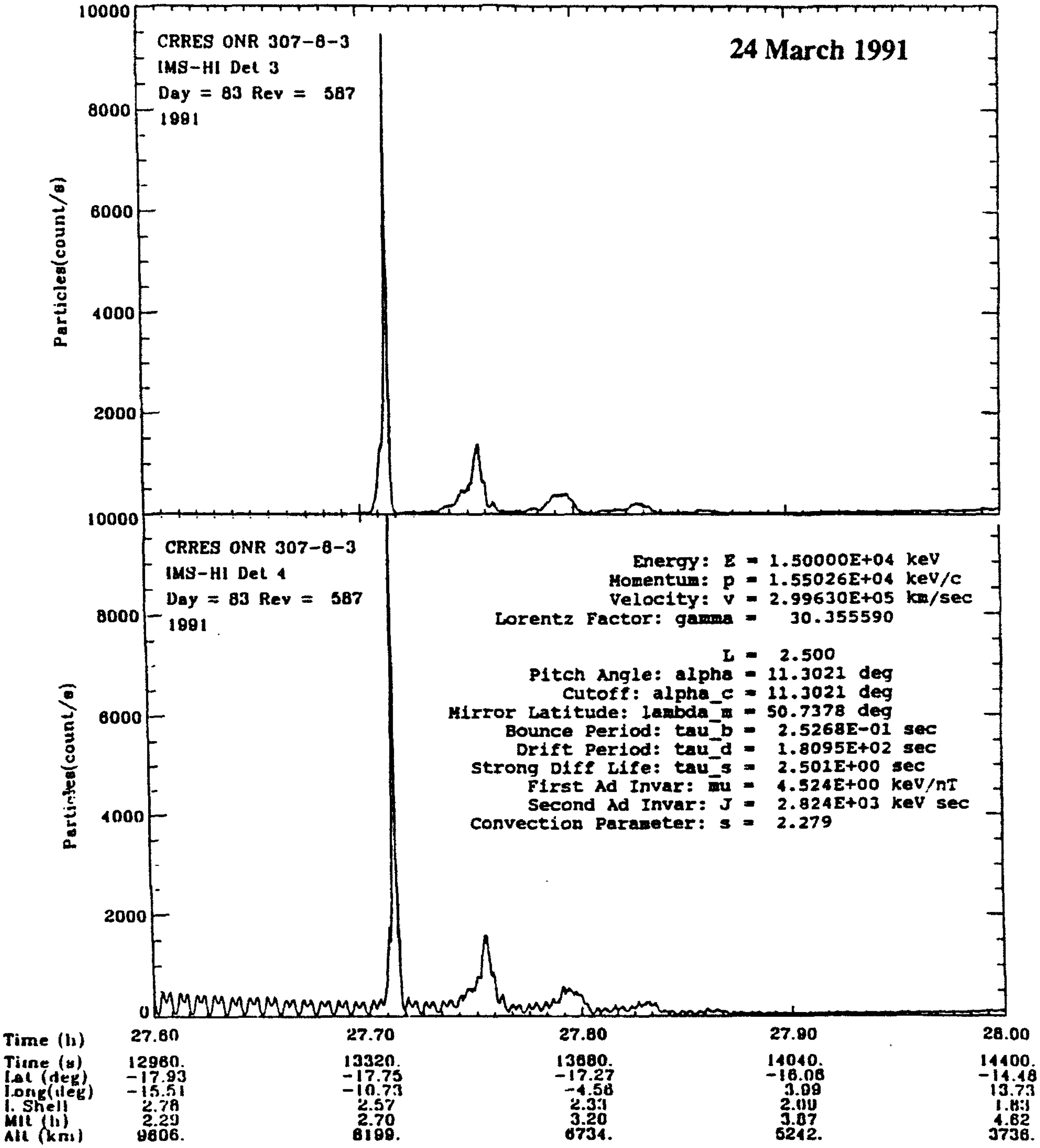

Energy: E = 1.50000E+04 keV
Momentum: p = 1.55026E+04 keV/c
Velocity: v = 2.99630E+05 km/sec
Lorentz Factor: gamma = 30.355590

L = 2.500
Pitch Angle: alpha = 11.3021 deg
Cutoff: alpha_c = 11.3021 deg
Mirror Latitude: lambda_m = 50.7378 deg
Bounce Period: tau_b = 2.5268E-01 sec
Drift Period: tau_d = 1.8095E+02 sec
Strong Diff Life: tau_s = 2.501E+00 sec
First Ad Invar: mu = 4.524E+00 keV/nT
Second Ad Invar: J = 2.824E+03 keV sec
Convection Parameter: s = 2.279

Figure 16 Strong injected electron flux observed by IMS-HI during the 24 March 1991 magnetic storm onset

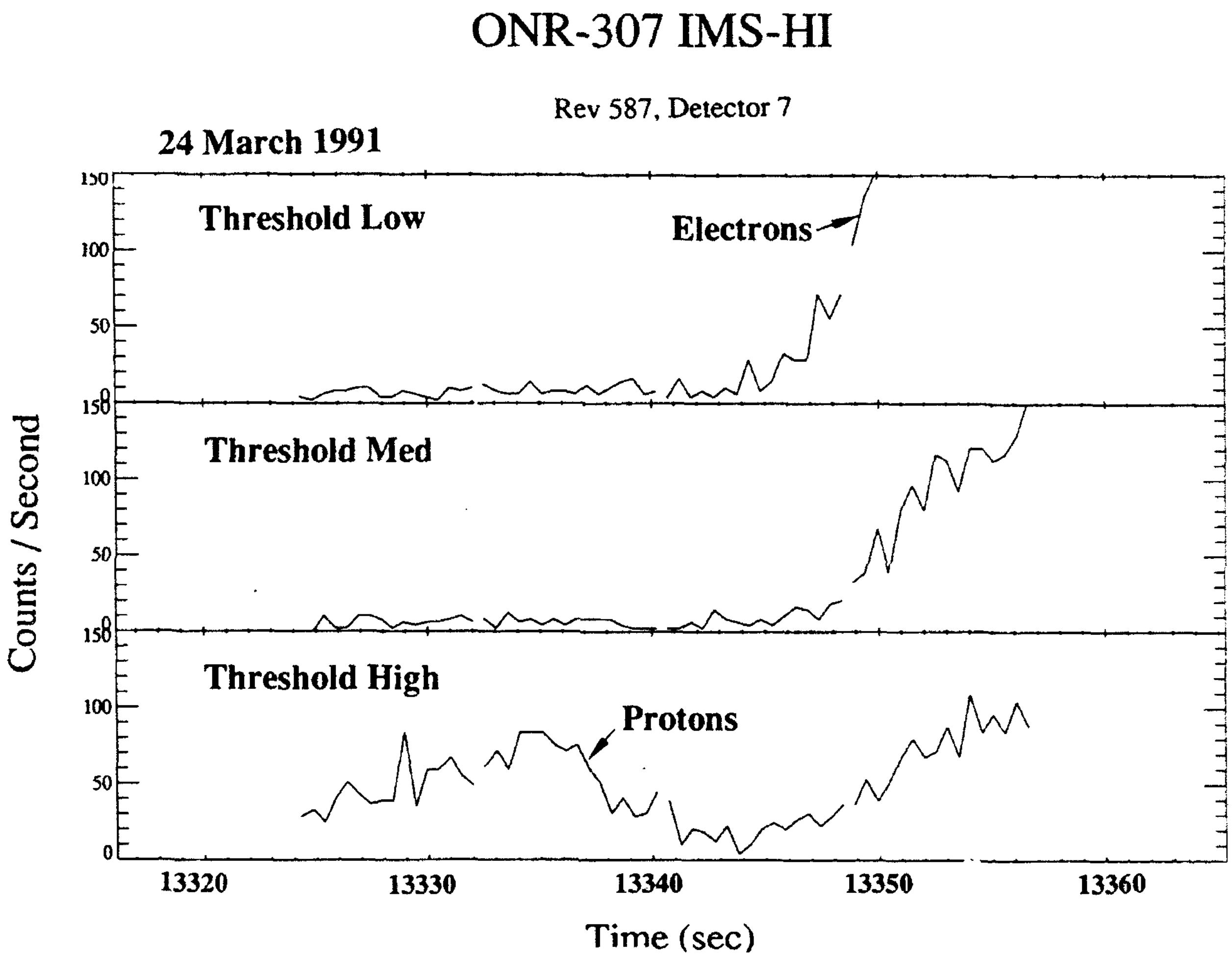

Figure 17 Greater than 50 MeV proton peak observed in the neutral detector about 35 s before the large electron peak

neutral detector, which is also sensitive to protons with E> 50 MeV, a particle burst was observed 0.5 minutes before the electron peak (Figure 17).

During the burst event the SEP instrument scanned through 7 logic modes (Figure 18) to measure the electron, proton , and alpha flux and energy spectra. In Figure 18 the lower panel shows the scintillator response of the anticoincidence shield on the SEP telescope. The voltage threshold of this scintillator is constant and is set at a low energy (~100 keV) so that it is very sensitive to penetrating radiation. The two largest peaks represent the first two electron bursts shown in Figure 16. The initial precursor at 13315 sec, which also appears in the E detector is thought to be E>100 MeV protons. The spin modulation may account for the apparent drop in flux after the precursor peak and before the low energy 20 MeV peak. The data indicate that the 100 MeV protons arrive at the detector first followed by the lower energy but higher fluxes of 25 MeV protons. The strong 15 MeV electron peak occurs about 30 seconds after the 25 MeV proton peak. This information can be used to infer some of the characteristics of the injection region.

3.4.3 Simulation of Radiation Belt Electron Bursts

The characteristics of the electron bursts of March 24 are: 1.) The peak is narrow in time (about 5 seconds), 2.) Some dispersion is apparent in the subsequent echoes as the successive peaks have lower amplitudes but are broader in time, 3.) The electron energy is large enough to penetrate the walls of the IMS-HI and SEP detectors and, 4.) The drift period decreases slightly between successive peaks as the L value of the satellite decreases. This observation strongly suggests the energy of the injected electrons increases with decreasing L.

This information can be used to investigate the initial energy and pitch angle distribution, the size of the injection region, and the time interval during which injection/acceleration persisted. As a first approximation it was assumed that electrons were injected into the unperturbed geomagnetic field and followed the normal gradient and curvature drifts. Various initial particle distributions were used and the count rates which would have been observed at the CRRES satellite were tabulated for comparison with the experimental data. An example of the simulation is shown in Figure 19. The simulation was developed by M. Walt using a Monte Carlo technique. Initial particles were drawn from various specified distributions in initial longitude, energy, time of injection, and pitch angle. The drift motion of each particle was then tracked about the earth and tabulated each time it reached the satellite position. The resulting count rates then gave the expected signal the CRRES satellite would have been expected to observe.

Samples of these results are shown in the insert of Figure 19, the lower panel of Figure 20, and in Figures 21 and 22. The energy dispersion is investigated in Figure 19 where the initial energy distribution is represented by exp(- E/2 MeV) with a threshold determined by the IMS-HI

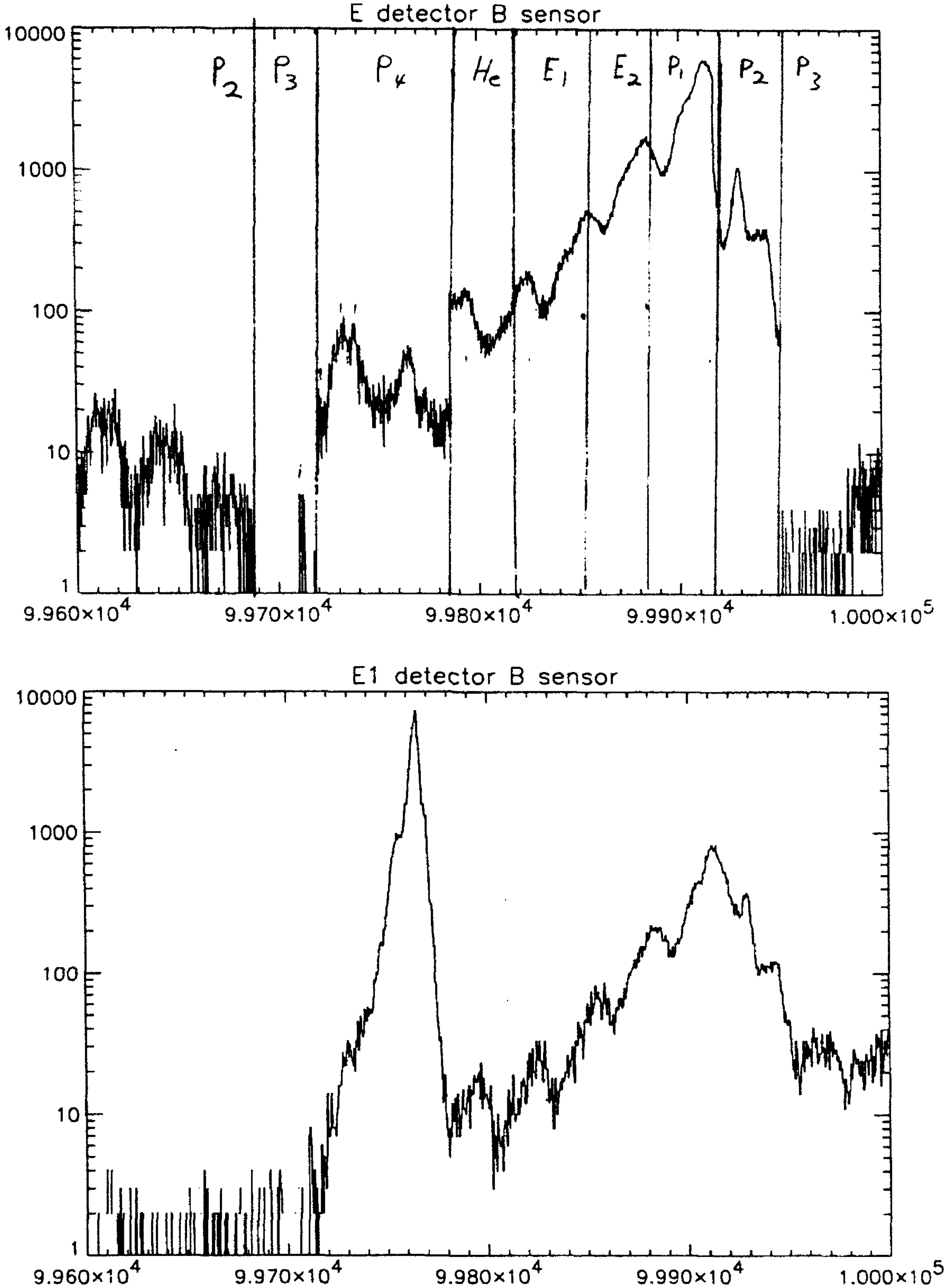

Figure 18 SEP instrument response to the slot region injection event of 24 March 1991. The upper panel is for the E detector and the lower panel for the Anti-scintillator shield.

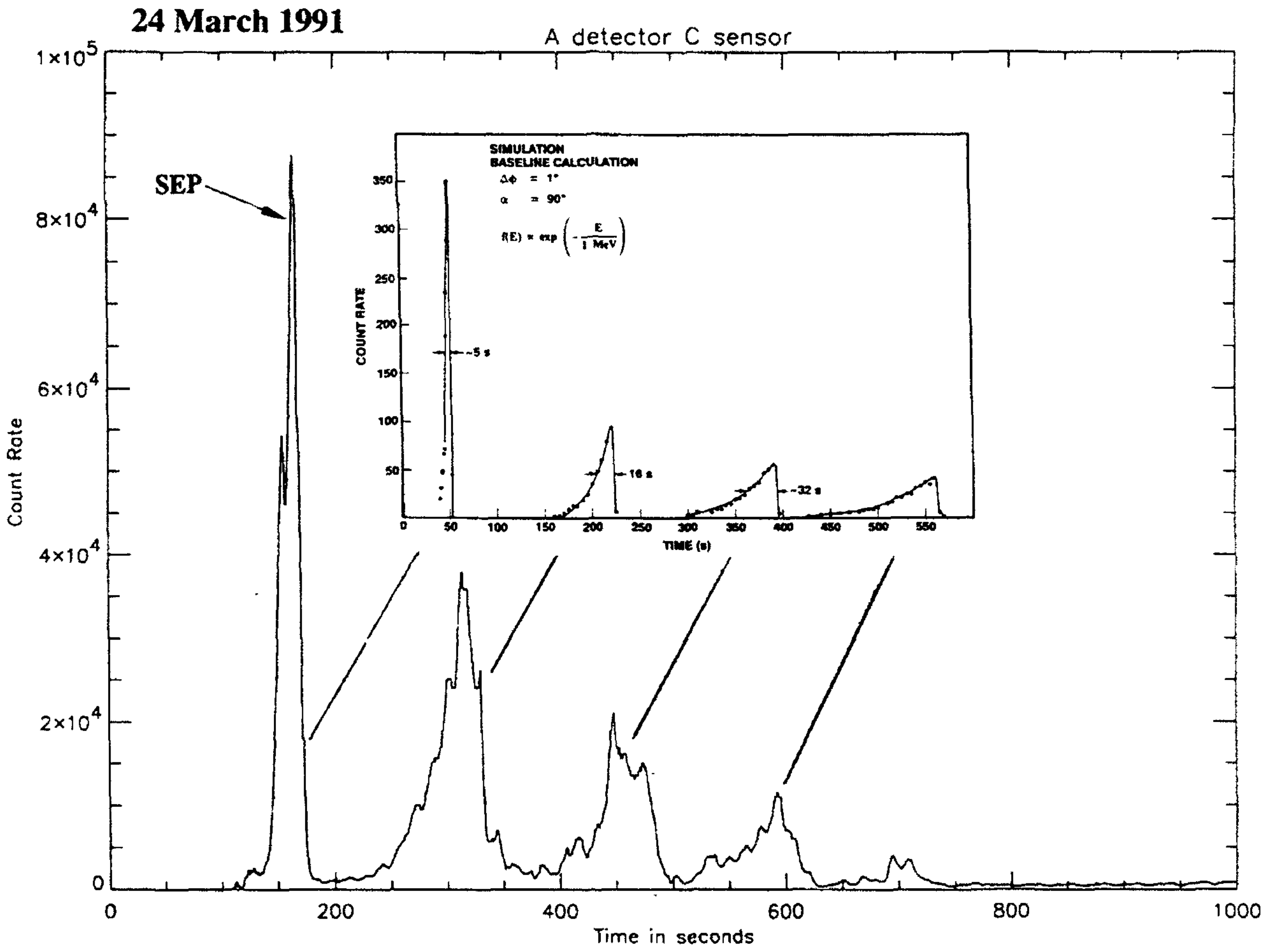

Figure 19 Monte Carlo simulation of the L=2.5 injection of energetic electrons (inset) and the SEP A detector

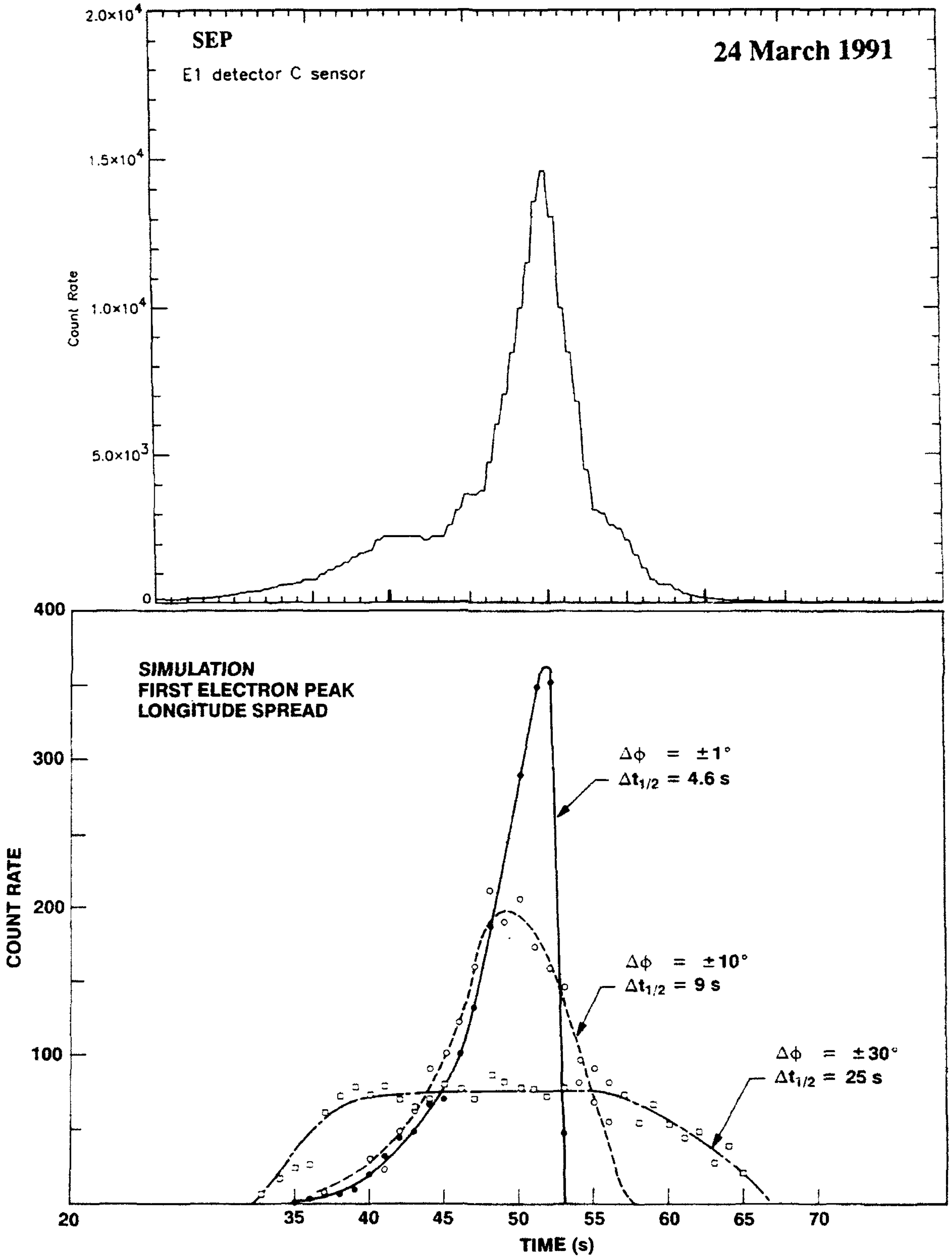

Figure 20 Simulation of the longitude interval of injection (lower panel) compared to the SEP E1 detector data.

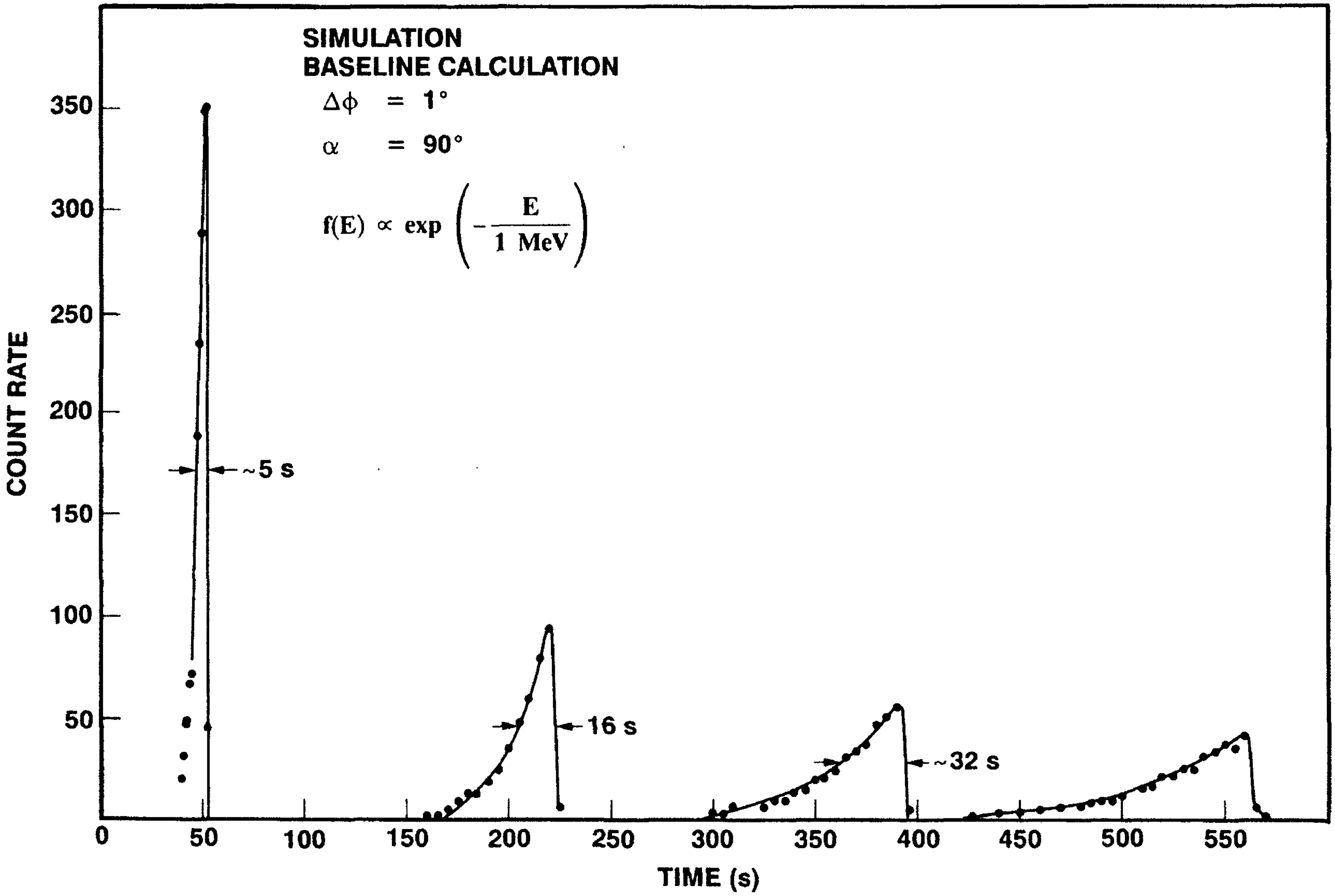

Figure 21 Pitch angle sensitivity simulation

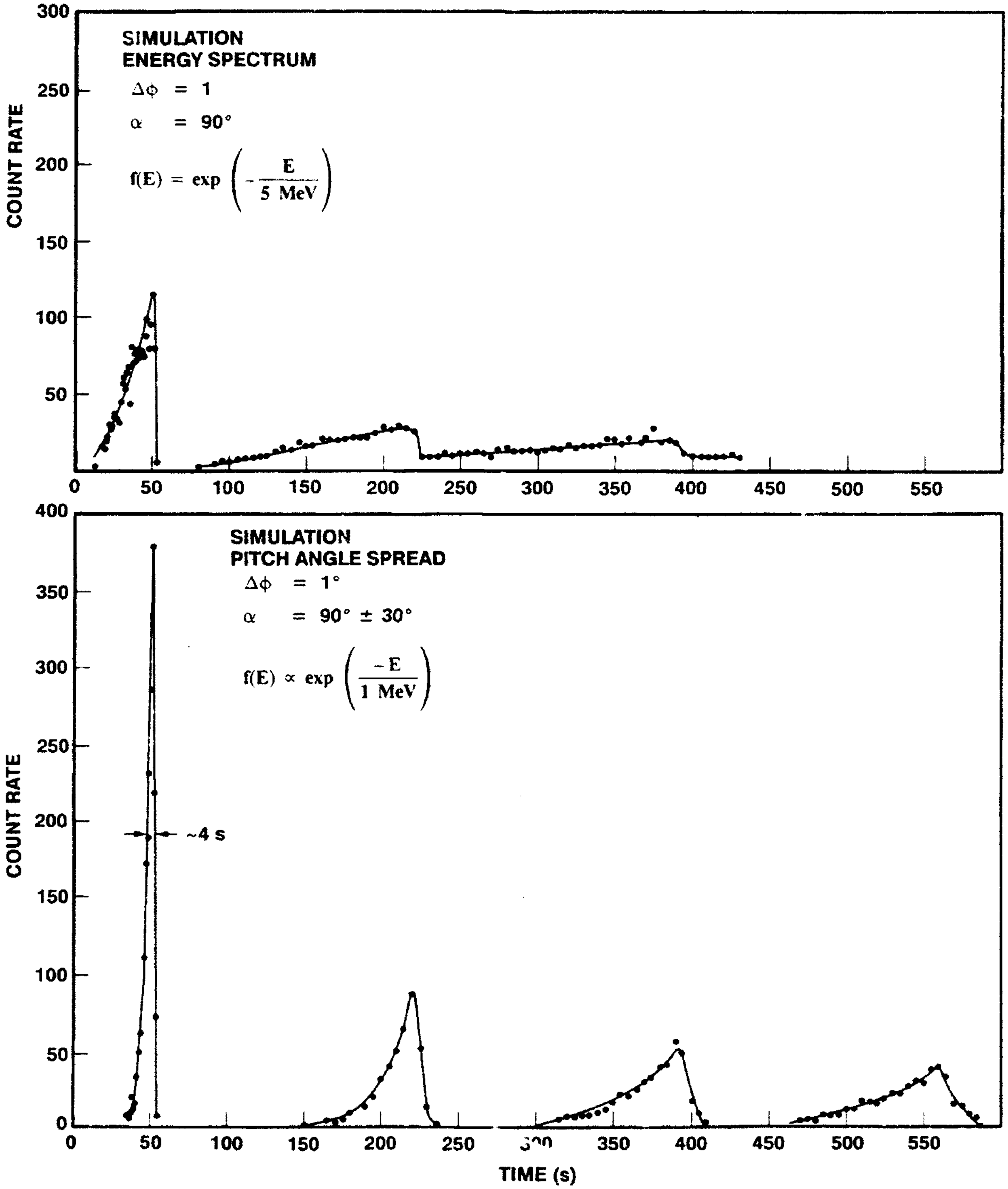

Figure 22 Simulation of the energy spectrum and pitch angle spread for injected electrons at L=2.5

detector sensitivity at 10 MeV. Particles were injected simultaneously in a narrow longitude interval (1°) and in equatorial orbits. The calculated dispersion under these conditions is due entirely to the initial energy spread and is similar to the observed values. Therefore, the initial energy distribution, must have been very narrow and if expressed as an exponential, had an e-folding energy of no more than 2 MeV. The echo peaks confirm this result as shown in Figure 22. If the e-folding energy is as large as 5 MeV, the second and third peak become unacceptably long due to the dispersion in drift period with energy.

Figure 20 explores the longitude interval of injection and compares the simulation results with the width of the initial electron peak. It is apparent that with these assumptions the injection region can have a longitude spread of no more than about 10 degrees. Otherwise the first peak would have had too long a time duration.

The shape of the electron pulses are not sensitive to the pitch angle distribution as shown in Figure 21. In Figure 22 the initial flux was assumed to be spread uniformly in equatorial pitch angle between 60 and 90 degrees. The simulated electron bursts are not significantly different from those with the flux concentrated at 90 degrees.

3.5 Radiation Belt Acceleration and Transport

Before the CRRES measurements, the very strong response of the radiation belts at L=2.5 to a sudden commencement (SC) was not expected. The CRRES data suggest that the radiation belt fluxes and energies are affected within minutes of initiation of the SC magnetic shock in the magnetosphere. To properly model and predict the radiation belt effects the algorithms must take into consideration the recent or expected magnetic activity factors.

In this section an initial attempt is made to explain the CRRES data for the surprisingly rapid injection of MeV particles in the inner radiation belt. Various mechanisms have been suggested such as solar MeV particle penetration , inner belt expansion during the storm, electric-field drift accelerations (Pfitzer, 1992), and direct magnetic compression and relaxation (Voss, 1992d) as discussed in this report. The important requirement of the theory is that it should explain the following key data:

1) The narrow 5 second pulse width of the electron bursts indicate a narrow longitude spread and a short time interval of injection.
2) The preferential acceleration of only MeV energy particles.
3) The greater injected particle energy at lower L shells.
4) The apparent dusk-noon location of the injection region (or the relative delay between the proton and electron peaks).
5) The simultaneous injection/acceleration of MeV electrons, protons, and alpha particles.

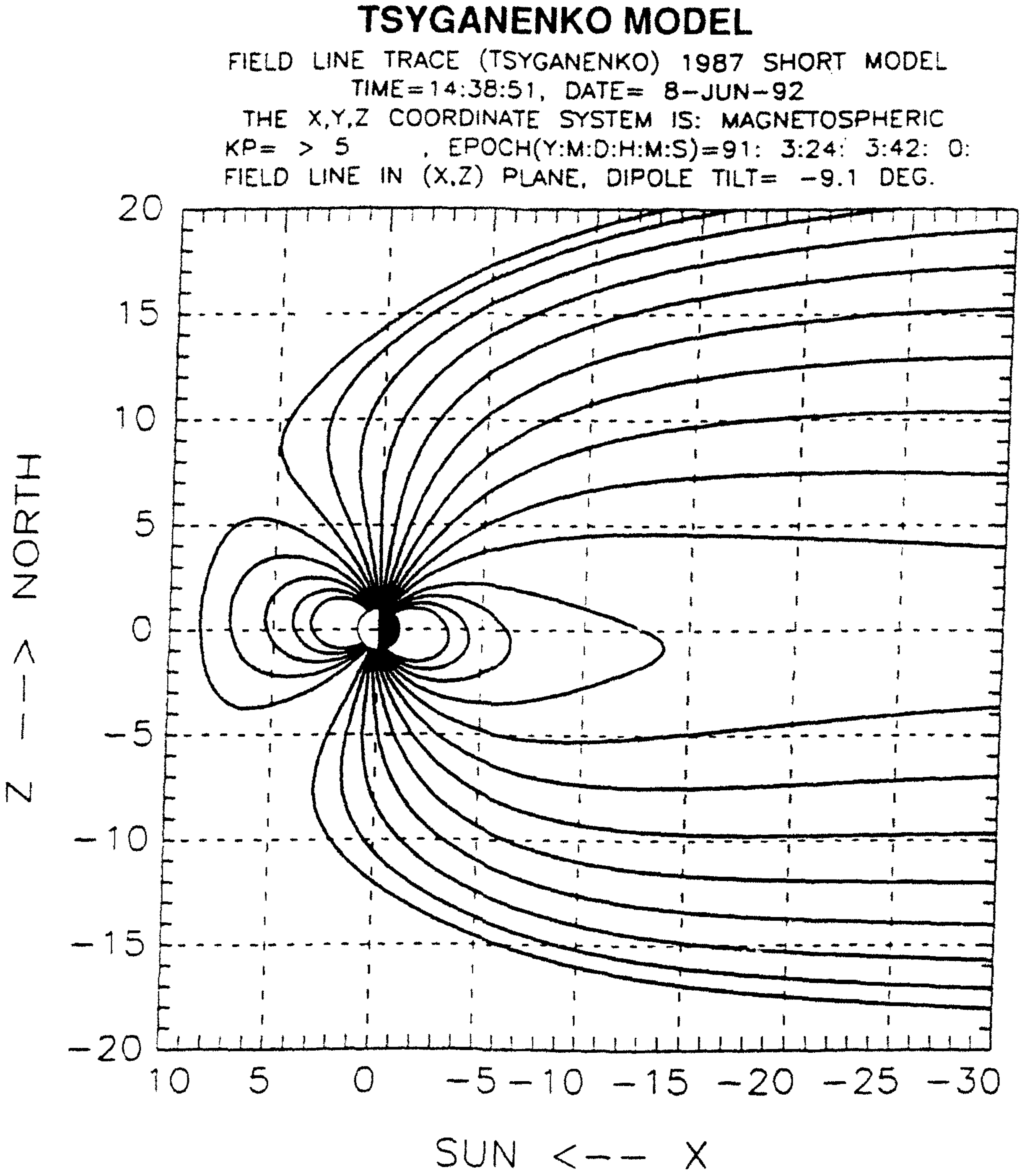

Figure 23 Tsyganenko model for Kp > 5 during the CRRES injection event

6) The nearly simultaneous injection of particles with the magnetic compression (150 γ at CRRES) during the SC.

The magnetic field configuration at the time of the SC is shown in the field line traces of Figure 23, using the Tsyganenko (1987) short model for Kp>5. The dipole tilt is - 9.1 degrees. For this case the standoff distance is about 8 Re, much greater than what is inferred during a SC shock impulse.

To understand the impact of a shock on the magnetosphere and radiation belt a simple model was formulated using a dipole field and a parallel shock front. The parallel shock was constructed using an image dipole. The algorithms were also set up to vary the strength of the image dipole so that earth's dipole field would form a magnetosphere cavity (Hones, 1963). An example of the image dipole field line trace is shown in Figure 24 for a standoff distance of 5 Re.

The objective of this simple model is to represent the first order physics for explaining the acceleration and transport of particles within the radiation belts during a shock compression. The large 120 gamma field increase observed at the CRRES location at 03 MLT (Figure 25) is thought to be the result of the magnetosphere compressing, i.e. the sum of the earth' s dipole and image dipole in our simple model. On the front side of the magnetosphere the compression is much greater because that region is much closer to the image dipole (r^{-3} dependence). The drifting of particles along constant B results in the rapid transport of high energy particles to lower L shells and the violation of the third invariant. Following Parker (1960) the perturbation fields of an image dipole are:

$$\begin{aligned} B'_x &= 3B_o \left(\frac{a}{r}\right)^3 \bullet \; z\left(\frac{1}{r^2}\right) \\ B'_y &= 3B_o \left(\frac{a}{r}\right)^3 \bullet \; z\,(y+2L)\left(\frac{1}{r^2}\right) \\ B'_z &= B_o \left(\frac{a}{r}\right)^3 \bullet \left(\frac{3z^2}{r^2}-1\right) \end{aligned} \qquad (2)$$

where $r = x^2 + (y+2L)^2 + z^2$ and 2L is the dipole separation distance. For small changes in the magnetosphere the drift orbit of particles may be represented as circles that are offset from the center of the earth. During rapid compression the ring of particles are "frozen" to the field lines (Parker, 1963, Birmingham and Jones, 1968) and move in the antisolar direction as illustrated in Figure 26. However, because of the higher magnetic field strength on the day side during compression, the subsequent drift circles of undisturbed particles have centers in the solar direction from the earth's center.

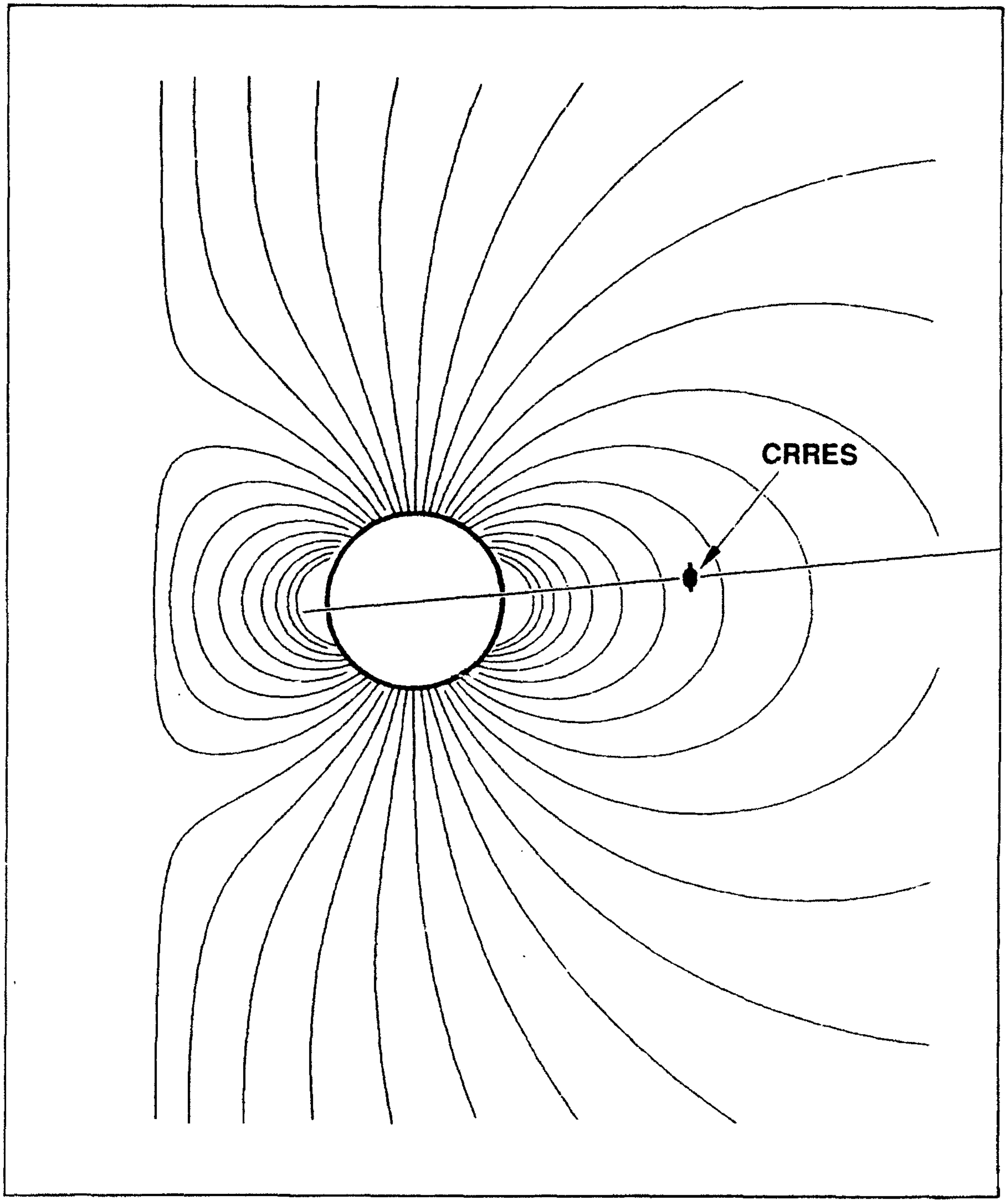

Figure 24 Field line trace of a dynamic magnetosphere using an image dipole

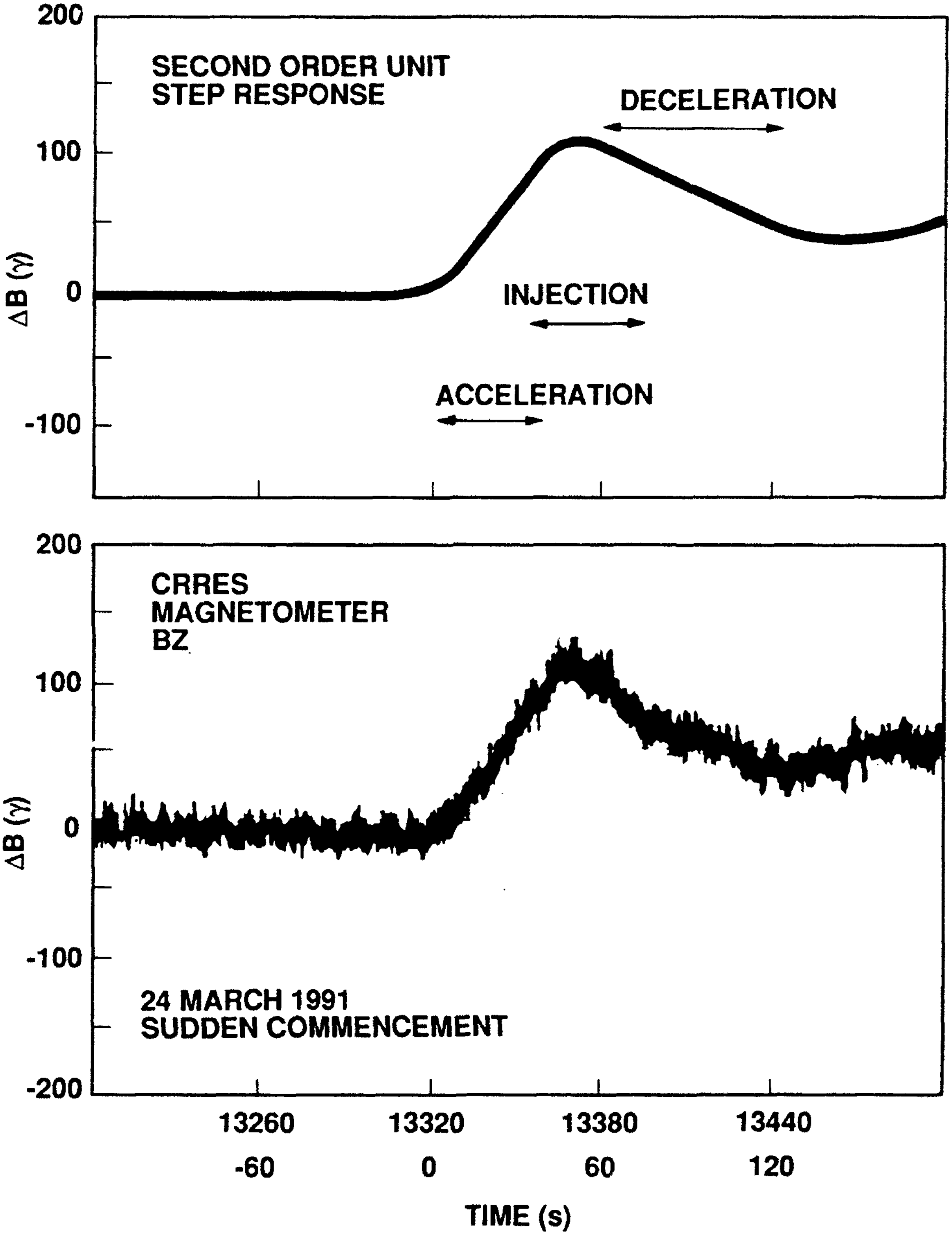

Figure 25 CRRES magnetic field data during the 25 March 1991 sudden commencement

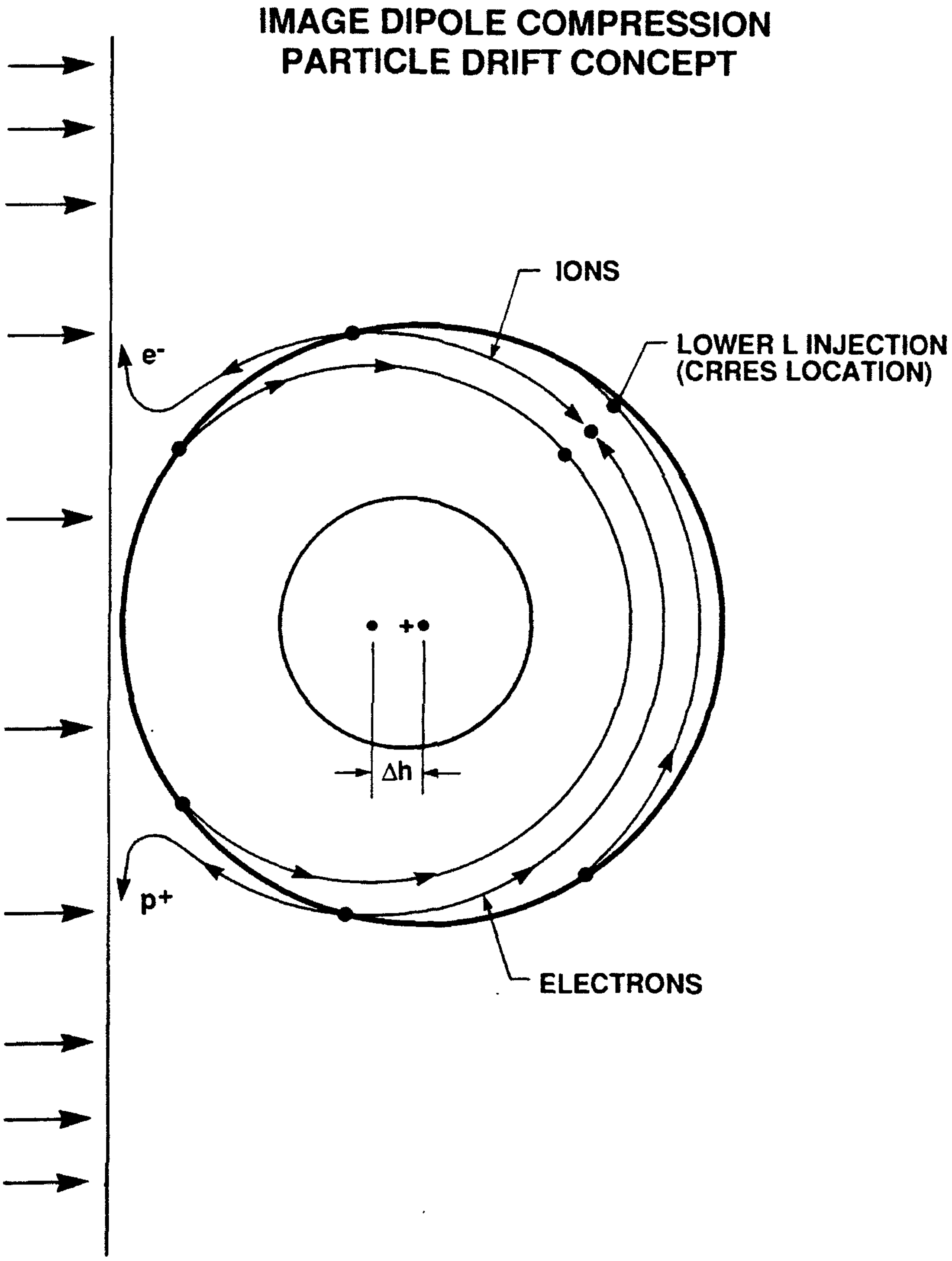

Figure 26 Approximate shift of particle drift orbits during a magnetic compression due to an image dipole

Using the magnetic observations at the CRRES satellite (100 gamma increase) and the image dipole model the standoff distance varies with time as shown in Figure 27 for a minimum standoff distance of 3 Re. Although this momentary penetration of the magnetopause in L to ~3.0 is surprising, much of the data can be explained with such an interpretation. After the initial penetration to low L (at 35 seconds) the magnetic field relaxes and the standoff distance backs off to L shells near 5. Following Henrick (1963) the magnetic line displacement during a compression event is given in Figure 28 assuming a final standoff distance of 3.0 and an initial standoff distance of 6.0. The resulting compression factor (an acceleration) is given in Figure 29. For a 6 Re particle that is compressed to 3 Re the acceleration would be about a factor of eight . A particle at 4 Re initially would move to 2.7 Re and have an acceleration of 4.5 times. On the night side the particles are only slightly affected in agreement with the data.

In this view the shock front compresses the frontside radiation belts to low L shells in about 30 seconds. The particles at noon ($3< L < 10$) are transported to L shells below 3 and are accelerated because of the increased magnetic flux from the adiabatic compression event (first invariant conserved). Using equation 2 for the dipole image model, the contours of constant B are shown in Figure 30 for standoff distances of 5, 3 and 2.5 Re. As the compression event proceeds the lower L shell contours shift towards the sunward direction, become tear shaped and then open up to give direct access from the compression region to the radiation belt inner slot. For 10> MeV electrons, protons, and heavier ions the drift periods are short enough (<3 minutes) so that these particles can drift to the nightside before the magnetosphere is partially decompressed (relaxed). A simplified diagram illustrating the important features of the magnetic compression, acceleration, and relaxation model is shown in Figure 31. This model explains the observations found in the CRRES data for the 24 March 1991 expansion event:

1) The narrow 5 second pulse width of the electron bursts indicate a narrow longitude spread and a short time interval of injection.
2) The preferential acceleration of only MeV energy particles.
3) The greater injected particle energy at lower L shells.
4) The apparent dusk-noon location of the injection region (or the relative delay between the proton and electron peaks).
5) The simultaneous injection/acceleration of MeV electrons, protons, and alpha particles.
6) The nearly simultaneous injection of particles with the magnetic compression (150 γ at CRRES) during the SC.

4.0 Future Plans

Most of the effort during the first three years of this contract has been devoted to 1) understanding the new IMS-HI instrument medium energy ion and neutral data (i.e. intercalibration), 2) the development of powerful software using optical disk storage to build up a comprehensive database, 3) understanding the fundamental dynamics of the radiation belts so that the database is meaningful, and 4) beginning the development of the IMS-HI static radiation belt model. The ONR 307 contract has supported the basic instrument calibration and data processing effort which this contract has extended to further the intercalibration, database processing, and our understanding of the radiation belt dynamics.

We expect to submit for publication a paper on the dynamics of the radiation belts.

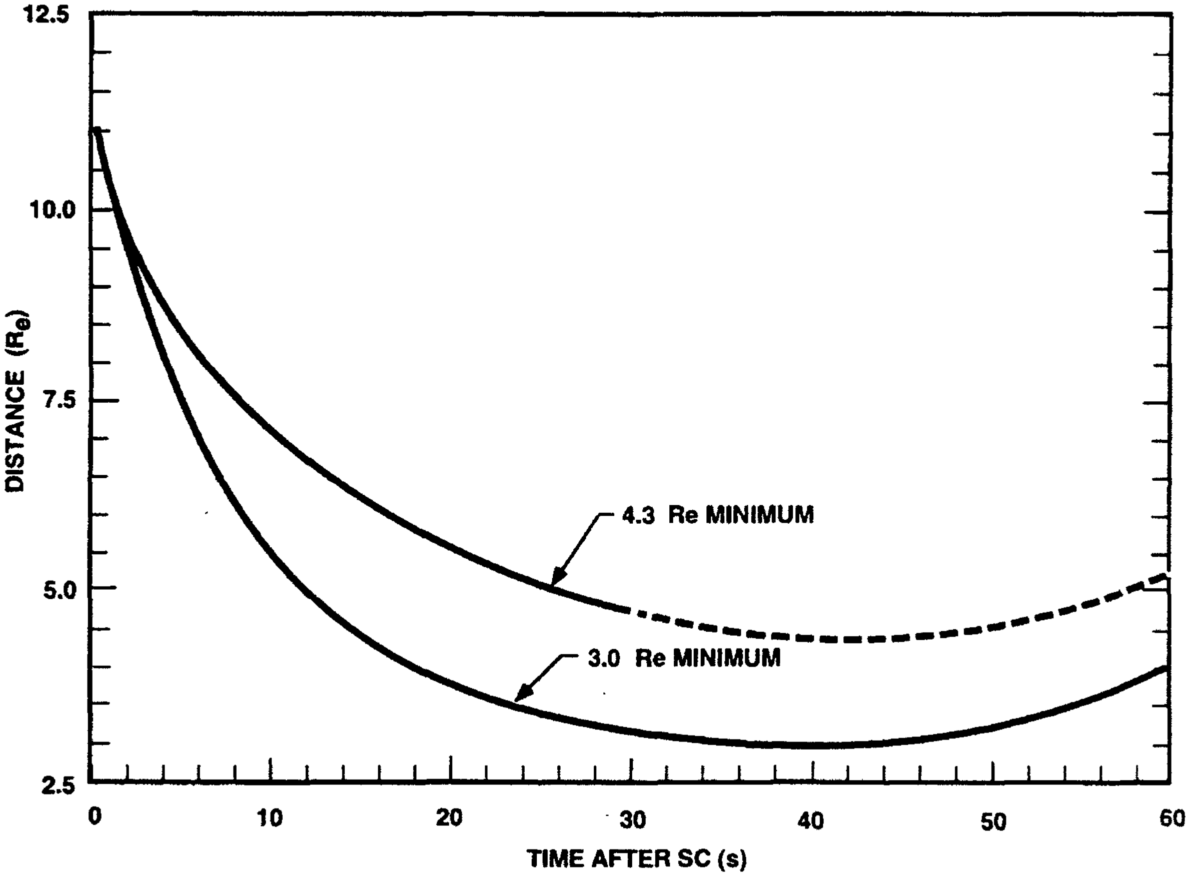

Figure 27 Standoff distance vs. time based on the image dipole compression of the magnetosphere.

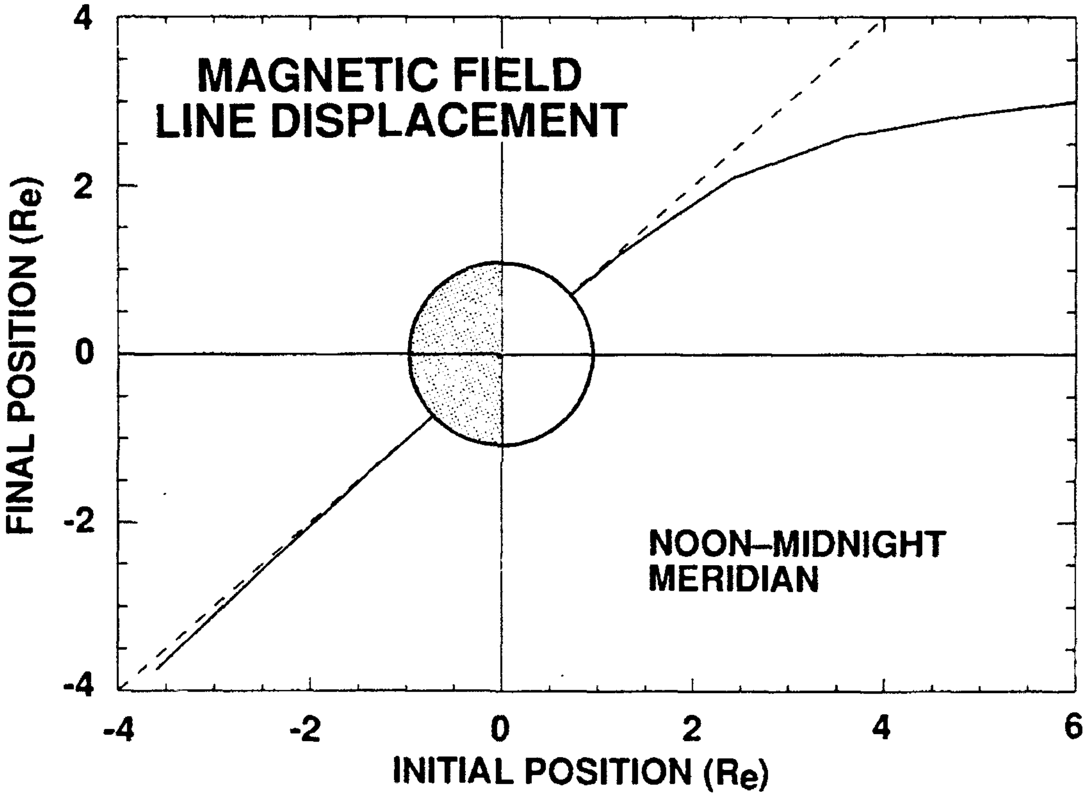

Figure 28 Magnetic field line displacement during a sudden commencement

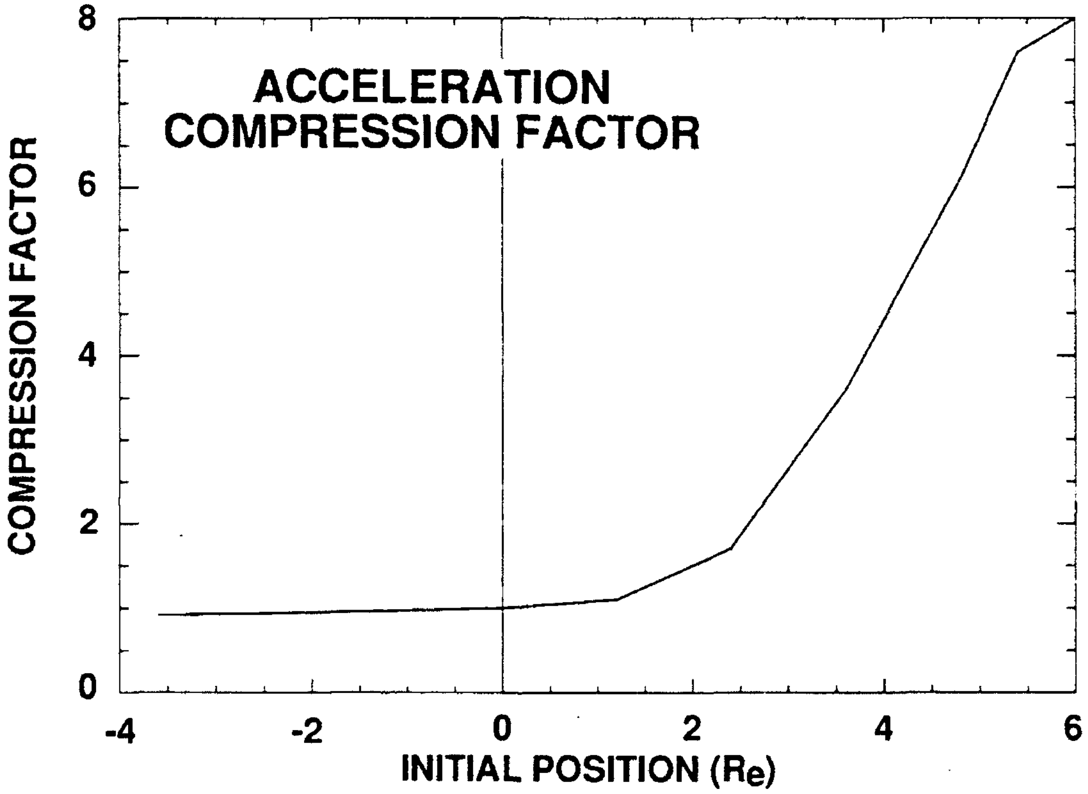

Figure 29 Magnetic field compression (acceleration) factor during a large sudden commencement

PARTICLE DRIFT CONTOURS DURING INJECTION

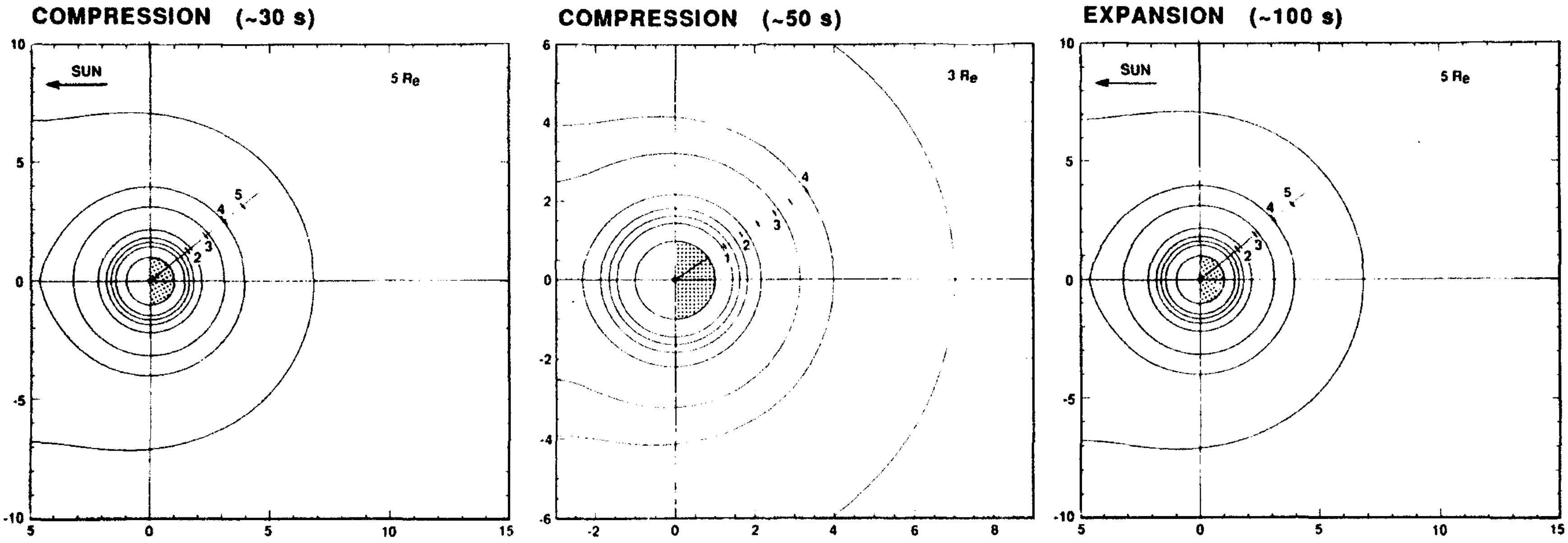

Figure 30 Constant B drift contours for particles during various stages of the compression event

RADIATION BELT ACCELERATION-DIRECT ACCESS MODEL

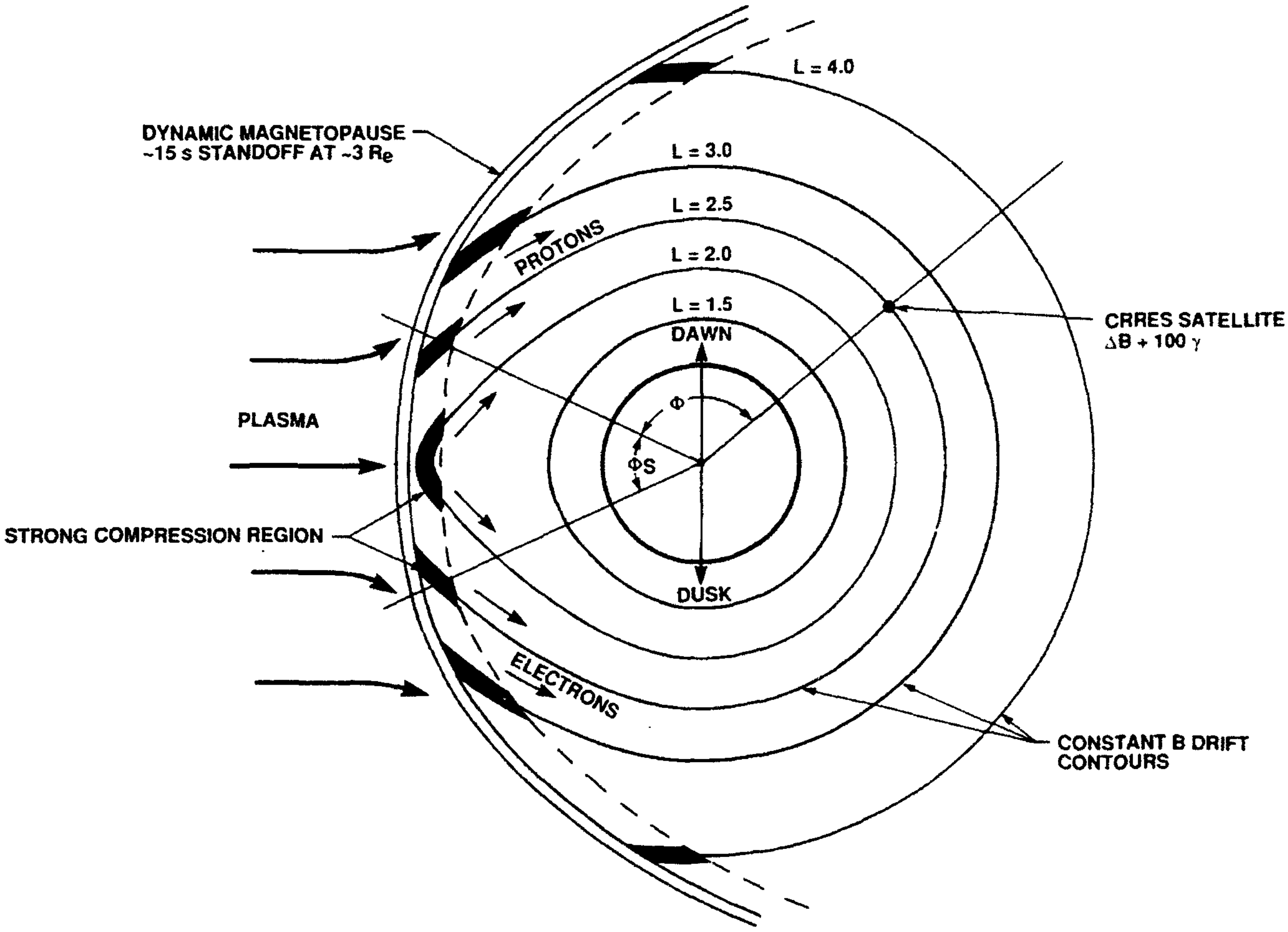

Figure 31 Model of acceleration and injection of > 10 MeV electrons,protons, and alphas into the radiation belt slot region during a sudden commencement.

5.0 References

Birmingham, T.J. and F.C. Jones, "Identification of Moving Magnetic Field Lines", J. Geophys. Res., 73, 5505, 1968

Blake, J.B. , W.A. Kolasinski, R.W. Fillius, and E.G. Mullen, "Injection of Electrons and Protons with Energies of Tens of MeV into L<3 on 24 March 1991", Geophys. Res. Lett., 19, 821-824, 1992

Collin, H.L., J.B. Cladis, J.M. Quinn, "Investigation of Ring Current/Storm Dynamics", PL-TR-92-2161, 1992, ADA256688

Gloeckler, F., B.Wilken, W. Studemann, F.M. Ipavich, D. Hovestadt, D.C. Hamilton, and G. Kremser, "First Composition Measurement of the Bulk of the Storm-time Ring Current (1-300 keV/e) with AMPTE/CCE", Geophys. Res. Lett., 12, 325, 1985

Gussenhoven, M.S., E.G. Mullen, D.H. Brautigam, E.Holeman, C.Jordan, F. Hanser, B. Dichter, "Preliminary Comparison of Dose Measurements on CRRES to NASA Model Predictions", IEEE Trans. on Nuclear Science, NS-38, 1655-1662, 1991

Henrich, L.R., "A Note on the Compression of the Earth's Magnetic Field and Hypothetically Related Phenomena", J. Geophys. Res., 68, 1295-1302, 1963

Hones, E.W, "Motion of Charged Particles Trapped in the Earth's Magnetosphere", J. Geophy. Res., 68, 1209-1219, 1963

Hsieh K.C., C.C. Curtis, C.Y. Fan, and M.A. Gruntman, "Techniques for the Remote Sensing of Space Plasma in the Heliosphere Via Energetic Neutral Atoms: a Review", in Solar Wind Seven, eds. E. Marsch and R. Schwenn, Pergamon Press, 1992, 357

McEntire, R. W. , Lui, A. T. Y. , Krimigis, S. M. and Keath, E. P. , “AMPTE/CCE Energetic Particle Composition Measurements During the September 4, 1984 Magnetic Storm”, Geophys. Res. Lett., 12, 1985, 317-320

Mead, G.D., "Deformation of the Geomagnetic Field by the Solar Wind", J. Geophys. Res., 69,1181,1964

Moritz, J., "Energetic Protons at Low Altitudes: A Newly Discovered Radiation Belt Phenomenon and its Explanation", Z. Geophys., 38, 701,1972

Mullen, E.G, M.S. Gussenhoven, K.Ray, and M. Violet, "A Double-peaked Inner Radiation Belt: Cause and Effect as Seen on CRRES", IEEE Trans. on Nuclear Science, NS_38, 1713-1717, 1991

Nightingale, R.W., R.R. Vondrak, E.E. Gaines, W.L. Imhof, R.M. Robinson, S.J. Battel, D.A. Simpson, and J.B. Reagan, "CRRES Spectrometer for Electrons and Protons", J. Spacecraft and Rockets, 29, 614-617, 1992

Parker, E.N., "Geomagnetic Fluctuations and the Form of the Outer Zone of the Van Allen Radiation Belt", J. Geophys. Res., 65, 3117-3130, 1960

Pfitzer, K.A., "Acceleration Mechanisms in the Inner Magnetosphere", EOS Trans. Amer. Geophys. Union, 73, no. 14, (abstract), 1992

Reagan, J.B., R.W. Nightingale, E.E. Gaines, W.L. Imhof, and E.G. Stassinopoulos, "Outer Zone Energetic Electron Spectral Measurements", J. of Spacecraft and Rockets, 18, 83-88,1981

Roeloff, E.C. , D.G. Mitchell, and D.J. Williams, "Energetic Neutral Atoms (5-50 keV) from the Ring Current, Imp 7/8 and ISEE-1", J. Geophys. Res., 90, 10991-11008, 1985

Tinsley, B.A., "Neutral Atom Precipitation- a Review", J. Atmos.Terr. Phys., 43, 617, 1981

Tsyganenko, N.A., "Global Quantitative Models of the Geomagnetic Field in the Cislunar Magnetosphere for Different Disturbance Levels", Planet. Sp. Sci., 35,1347-1358,1987

Vampola, A. L. and A. Korth, "Electron Drift Echoes in the Inner Magnetosphere", Geophy. Res. Lett., 19, 625-628, 1992

Voss, H.D., "Energy and Primary Mass Determination Using Multiple Solid State Detectors", IEEE Trans on Nuclear Science, NS-29, 178-181, 1982

Voss, H.D., W.L. Imhof, M.Walt, J. Mobilia, R.M. Robinson, and R.W. Nightingale, "Intense > 10 MeV particle Injection Near L=2.5 During the 24 March 1991 Magnetic Shock", Eos Trans. Amer. Geophys. Union, 73, no. 14, (abstract), 1992a

Voss, H.D., E. Hertzberg, A.G. Ghielmetti, S.J. Battel, K.A. Appert, B.R. Higgins, D.O. Murray, and R.R. Vondrak, "The Mediu m Energy Ion Mass and Neutral Atom Spectrometer (ONR-307-8-3)", J. Spacecraft and Rockets, 29, 566-569,1992b

Voss, H.D., J. Mobilia, H.L. Collin, and W.L. Imhof, "Satellite Observations and instrumentation for Imaging Energetic Neutral Atoms", SPIE, 1744, Instrumentation for Magetospheric Imagery, 79-90, 1992c

Voss, H.D., "Acceleration of Particles to >10 MeV at L=2.5 During a Sudden Commencement", EOS Trans. Amer. Geophys. Union, (abstract) , Fall, 1992d

Appendix 1

IMS-HI Instrument Paper

JOURNAL OF SPACECRAFT AND ROCKETS
Vol. 29, No. 4, July-August 1992

Medium Energy Ion Mass and Neutral Atom Spectrometer

H. D. Voss,[*] E. Hertzberg,[†] A. G. Ghielmetti,[‡] S. J. Battel,[§] K. L. Appert,[†] B. R. Higgins,[†]
D. O. Murray,[*] and R. R. Vondrak[¶]
Lockheed Palo Alto Research Laboratory, Palo Alto, California 94304

The primary objective of the medium energy ion mass spectrometer (ONR 307-8-3) on the CRRES is to obtain the necessary data to construct models of the energetic ion (10–2000 keV-amu/q^2) and neutral atom (10–1500 keV) environment of the Earth's radiation belts. The spectrometer measures the energetic ion composition, energy spectrum, charge, and pitch angle distribution with good mass, temporal, and spatial resolution. The ion rejection in the neutral detector is < 100 MeV-amu/q^2. The instrument principle of operation is based on ion momentum separation in a 7000-G magnetic field followed by energy and mass defect analysis using an array of cooled silicon solid-state detectors. The architecture is parallel with simultaneous mass and energy analysis at relatively high sensitivity (100% duty cycle). The instrument performed as designed in orbit with the major groups of hydrogen, helium, oxygen, and neutrals clearly resolved. The energetic ion composition during the August 26, 1990, storm illustrates the instrument performance.

I. Introduction

THE medium energy ion mass spectrometer (IMS-HI) on the Combined Release and Radiation Effects satellite (CRRES) measures the energy spectra and pitch angle distributions of magnetospheric ions and neutral particles. The instrument is designed specifically to measure the highly variable fluxes of ions in the energy range from a few tens of kiloelectron volts to a few hundred kiloelectron volts that populate the ring current and produce the variations seen in the magnetic Dst index associated with magnetic storms.

Ring-current studies based on data from the Explorer 45 spacecraft[1] were hampered because the detectors did not distinguish between protons and higher mass ions. Other researchers[2-5] have demonstrated the importance of including neutrals and ions other than protons to explain the decay rates observed in the ring current. By charge exchange with thermal hydrogen atoms, energetic ions become neutrals and can escape from the Earth's environment. This is a significant loss process for the medium-energy ring current ions. More recent measurements obtained by the medium-energy plasma analyzer on the AMPTE/CCE spacecraft have demonstrated the advantages of comprehensive ion composition measurements for the study of ring current processes.[6]

On CRRES, ring-current ion composition and neutral atom measurements are provided in part by the IMS-HI instrument. This instrument is one of four instruments that comprise the Office of Naval Research (ONR-307) energetic particles and ion compositon (EPIC) experiment. The contiguous mapping of the particle distribution over the radial distance range from 400 km to 5.5 Earth radii (Re) near the equatorial plane provides a comprehensive data base that can be used for studies of radiation belt and ring-current energization, injection, and loss processes.

II. Measuring Techniques

The IMS-HI instrument is based on ion momentum separation in a magnetic field followed by energy and mass defect analysis using an array of cooled silicon solid-state sensors as shown in Fig. 1. The entrance collimator consists of a series of rectangular baffles that define the ion beam angular resolution and a broom magnet to reject electrons with energy less than 1 MeV.

After exiting the collimator ions enter a 7000-G magnetic field where they are deflected (mv/qB) onto a set of six passively cooled (-50°C) silicon surface-barrier detectors. The technique of cooling solid-state detectors for high-resolution [<2 keV full width at half maximum (FWHM)] energetic ion measurements in spacecraft instruments was discussed by Voss et al.[7] and was successfully demonstrated in the stimulated emission of energetic particles (SEEP) experiment on the S81-1 satellite.[8] The energy range covered varies with ion species and is approximately em/q^2 = 10–2000 keV-amu/q^2. A seventh sensor, located directly in line with the collimator, measures energetic neutrals and has an ion rejection of approx-

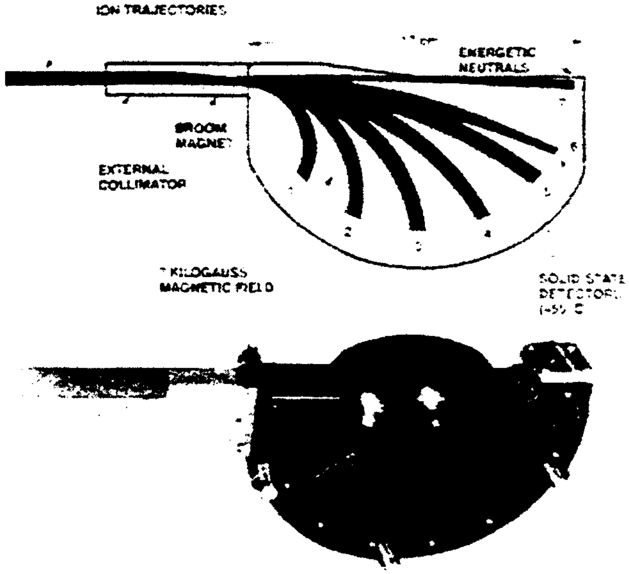

Fig. 1 Principle of operation for IMS-HI is based on ion momentum, mass defect, and energy analysis using an array of cooled solid-state detectors. Magnet is shown in the upper portion of the figure and the ion optics in the lower portion.

Received July 12, 1991; revision received Oct. 11, 1991; accepted for publication Oct. 11, 1991. Copyright © 1992 by the American Institute of Aeronautics and Astronautics, Inc. All rights reserved.

[*] Staff Scientist, Space Sciences Laboratory, Dept. 91-20, B/255, 3251 Hanover Street.

[†] Research Engineer, Space Sciences Laboratory, Dept. 91-20, B/255, 3251 Hanover Street.

[‡] Research Scientist, Space Sciences Laboratory, Dept. 91-20, B/255, 3251 Hanover Street.

[§] Space Sciences Laboratory, Dept. 91-20, B/255, 3251 Hanover Street; currently, Consultant, Battel Engineering. Member AIAA.

[¶] Manager, Space Sciences Laboratory, Dept. 91-20, B/255, 3251 Hanover Street. Associate Fellow AIAA.

Table 1 Medium energy ion mass spectrometer (IMS-HI) specifications

Analyzer	7 kg magnet (m/q^2) and mass defect
Sensors	Silicon surface barrier (−55°C)
Number of imaging sensors	7 at 0.5 cm^2 each
Look direction from spin axis	75 deg
Particles and energy range:	
Neutrals	10–1500 keV
Protons	15–2000 keV
Helium	4–500 keV
Oxygen	20–130 keV
Oxygen + +	20–500 keV
Other ions	E > 20 keV
Number of differential mass channels	64
Number of high rate mass channels	4
Number of differential energy channels	6
Pitch angle resolution	4 deg FWHM
Geometrical factor	10^{-2}–10^{-3} cm^2sr
Duty cycle	100%

imately 100 MeV-amu/q^2. Detailed instrument specifications are given in Table 1.

The instrument features simultaneous mass and energy analysis at relatively large geometrical factors (10^{-3} to 10^{-2} cm^2 sr). Simultaneous measurements of charge states can be identified for each m/q^2 and for the same m/q^2, in some cases, within the solid-state detector due to dead zone and mass defect energy losses for equal m/q^2 (e.g., O^{++} and He^+). Because of the multisensor design and parallel processing electronics, the dynamic range in flux covered is approximately six orders of magnitude.

A simulation of the ion separation in a 7000-G magnetic field is shown in the position-energy diagram of Fig. 2. The image surface S is defined as the arc length, beginning at the collimator, for a radius $R = 8$ cm. Solid-state detectors 1-7 are located at angles Θ of 40, 65, 90, 115, 140, 162.5, and 180 deg, respectively. Solid-state detectors 1-6 are n-type silicon having either 20 or 40 $\mu g\ cm^{-2}$ of gold surface deposit. The neutral detector is of p-type silicon to improve light rejection and radiation damage sensitivity and has 20 $\mu g\ cm^{-2}$ of aluminum surface deposit. The energy loss in surface-barrier windows for H, He, and O is discussed by Voss.[9] The mass defect in solid-state detectors results from energy loss of nonionizing nuclear collisions within the solid that reduce the efficiency of electronic signal generation. The mass defect increases with atomic weight of the nuclei in a well-understood way[10] and causes further mass separation, with commensurate energy scatter, for the heavier nuclei.

The magnet section consists of a yoke, pole pieces, and a SmCo permanent magnet. To produce a homogeneous magnetic field with high inducton (~7 kG) in a 5-mm gap and with minimized weight, the best available magnetic material (SmCo Recoma 25, with 25 MGOe energy product) was selected. The yoke completely surrounds the magnetic field except for the entrance aperture, permitting one to reduce the magnetic resistivity in the return flux section and to minimize the magnetic stray fields. Shape and dimensions of the yoke are optimized to reduce weight and are designed for a uniform magnetic induction of 19 kG anywhere within the yoke. The resultant complex shape necessitates the use of numerical computer-aided machining methods to meet the weight requirement and design goal of ≤ 100 nT magnetic stray field at a distance of 1 m. A yoke materia' (Hyperco 50) that possesses relatively high permeability (2000–4000) at high-induction levels (20 kG) was chosen. The mass of the flight yoke and magnet assembly is about 5.7 kg.

A functional system diagram of the IMS-HI is shown in Fig. 3. Variable pulse-height signals from the ion sensors are each routed for analysis to a peak detector circuit and analog multiplexer. Each peak detector circuit is allowed to track and hold the highest peak value for input pulses below the programmable low level threshold V_T and to hold and stop sampling for input pulses above V_T. This allows signals to be processed well into the noise level for added in-orbit performance. The sample interval for each detector is 45 μs. The read and reset of each peak detector circuit is controlled by strobes from a master clock so that a continuous and sequential scan is made of each detector.

Simultaneous with the reset command, a 256-channel analog-to-digital converter is activated, and the resulting digital pulse height (8 bits) is placed on the address bus of an energy lookup table. Also placed on the address bus of this RAM are the 3 bits that specify which detector is being processed. The content of this memory cell (16 bits) is read into an accumulator, incremented by one, and then read back into the memory cell. An address counter is then used to sequentially step through the entire RAM for telemetry readout. A data compressor packs the 16-bit sum into an 8-bit byte for serial interface with the satellite telemetry.

The instrument operates in two basic modes; mass lock and mass scan. In the mass scan mode, each of the seven solid-state sensors is pulse-height analyzed into 256 levels of which 64 intervals are accumulated in memory and read out every 8 s. This mode is used to scan all mass peaks within the range of the sensor relative to the background continuum. In the mass lock mode, each of the seven solid-state sensors is pulse-height analyzed into 256 levels, of which four intervals (typically, four ions) are accumulated in memory and read out every half-second. This mode is used for making rapid spectral snapshots of four ions as a function of pitch angle. Baseline operation of the instrument will be to toggle every 32.768 s between the mass lock mode and the mass scan mode.

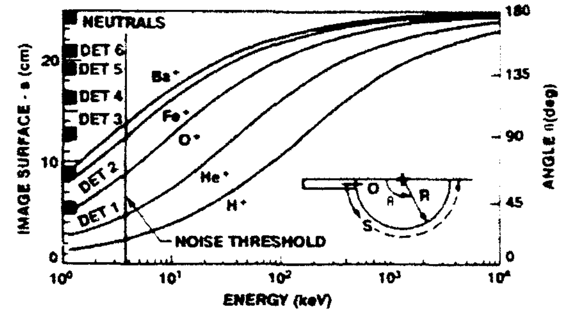

Fig. 2 Energy of various ions that are mapped onto the detector focal surface S is shown for a 7000-G magnetic field.

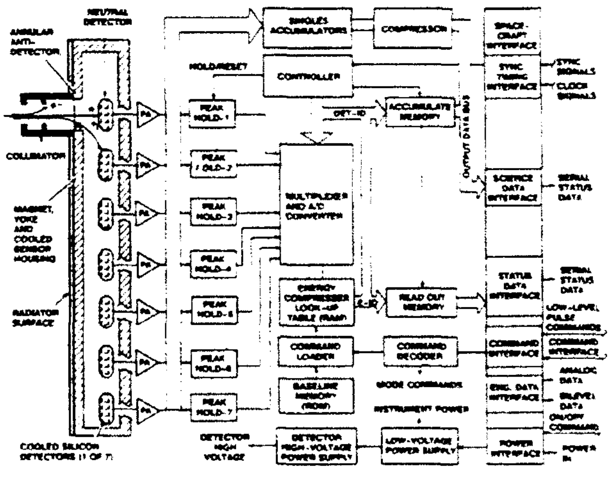

Fig. 3 Functional block diagram of the IMS-HI instrument.

III. Calibration

The IMS-HI instrument was calibrated at Goddard Space Flight Center (GSFC) using the low-energy accelerator for ions up to 150 keV. The instrument was mounted on a scan platform in a vacuum chamber at the output end of the accelerator beam line. At a bend in the beam line, an electromagnet was used to select the desired mass after the electrostatic acceleration. A solid-state detector at the entrance to the vacuum test chamber was used to monitor the beam stability. The instrument was calibrated using H^+, He^+, He^{++}, N^+, N^{++}, O^+, and O^{++} ions. The neutral detector was calibrated using energetic neutral hydrogen atoms.

To illustrate the instrument performance during calibration, an energy scan for protons impinging on detector 2 is shown in Fig. 4. The calibration data are currently being compared to the instrument computer model and to the flight data to arrive at the best-fit calibrations. The energy passbands are very clean as indicated in Fig. 4 and scattering from the pole pieces is less than 0.2%. The background rate can be subtracted using an algorithm based on the differential pulse-height spectrum in each of the seven detectors and the omnidirectional megaelectron volt electron flux.

In addition to the accelerator calibrations, the instrument was tested with radioactive sources at −30°C in its final flight configuration. Six T1-204 sources of varying intensities were used to saturate the sensors in a known fashion to calibrate flux rate effects. An internal electronic pulser was also included in the instrument to give several pulse heights at the detector front end to calibrate gain, linearity, and resolution in orbit. It has also been observed in orbit that, when the instrument is illuminated with high fluxes of megaelectron volt electrons in the outer belt, K-alpha lines are present and associated with high-atomic-number materials near the sensors.

IV. Preliminary Flight Results

The instrument design temperatures were achieved: −55°C for the magnet and sensors, −12° C for the preamps, and 0°C for the electronics box. The sensors' noise thresholds were therefore well within specifications. This is shown in Fig. 5 for detector 1 during orbit 77. Here the primary hydrogen peak is at 18 keV with a noise threshold of about 4 keV and a noise resolution of about 2 keV FWHM.

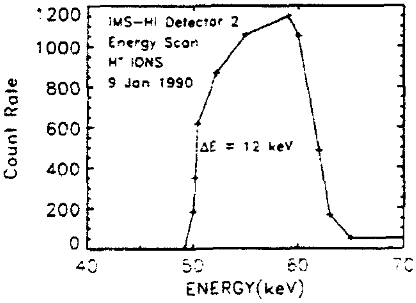

Fig. 4 Energy passband for protons in detector 2 obtained during preflight calibrations.

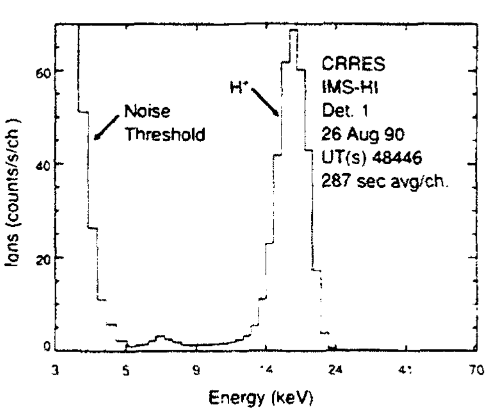

Fig. 5 In-flight data from detector 1 indicates a noise threshold of about 4 keV and a hydrogen ion peak resolution of 2 keV FWHM.

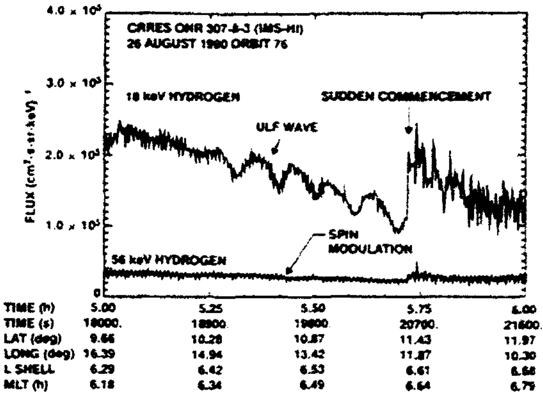

TIME (h)	5.00	5.25	5.50	5.75	6.00
TIME (s)	18000.	18900.	19800.	20700.	21600.
LAT (deg)	9.66	10.28	10.87	11.43	11.97
LONG (deg)	16.39	14.94	13.42	11.87	10.30
L SHELL	6.29	6.42	6.53	6.61	6.68
MLT (h)	6.18	6.34	6.49	6.64	6.79

Fig. 6 Example of scalar data from detector 1 and 2 for protons during the August 26, 1990, sudden commencement.

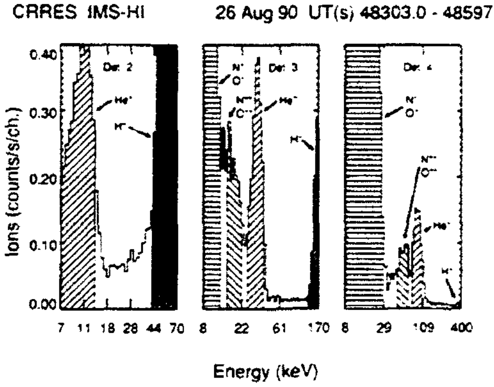

Fig. 7 Ion mass peaks observed in detectors 2, 3, and 4 during the August 26, 1990, storm.

The scalar data for 18- and 56-keV protons during the sudden commencement on August 26, 1990, is illustrated in Fig. 6. The major ultra lower frequency (ULF) wave-particle interaction is at 18 keV and nearly absent at 56 keV.

The final example of instrument performance is shown in Fig. 7 for the 64-channel mass spectrum of detectors 2, 3, and 4. These data were obtained on August 26, 1990 over a 5-min interval near $L = 5.0$. The distributions shown are for the raw count rates and do not have noise filtering, efficiencies, and other corrections included. The energy scale is preliminary and represents the deposited energy of the ions in the solid-state detectors.

The H^+ and He^+ peaks are conspicuous in each of the detectors as noted. The importance of mass defect in the solid-state detector is illustrated well in detector 4 for He^+ and O^{++}. Both ions have the same m/q^2 and thus the same energy incident on the detector (95 keV). Because the oxygen ion is less efficient at generating electron hole pairs, its peak is shifted down from the He^+ peak by about 30 keV. It is well separated from the He^+ and N^+/O^+ peaks. Thus, over certain energy and mass intervals the mass defect is an effective method of separating ion beams in a magnetic spectrometer. To obtain the ion flux, the penetrating backgrounds and skirts of the strong ion peaks must be properly subtracted using peak-analysis software.

V. Summary

The IMS-HI experiment on CRRES operated successfully since launch. Preliminary results show that the instrument is able to distinguish all of the major ion species and a few minor species with good time resolution. These measurements will comprise an important data base for studies of radiation belt and ring-current energization, injection, and decay rates.

Acknowledgments

This effort was supported by the Office of Naval Research under Contract N00014-83-C-0476 and by the Lockheed Independent Research Program. The authors wish to thank F. Hilsenrath, L. A. Hooker, T. C. Sanders, D. A. Simpson, and V. F. Waltz for their efforts in the design, development, and fabrication of this instrument. We wish to thank R. M. Robinson and J. Mobilia for comments on the manuscript, and R. A. Baraze and R. McDonald for their efforts in data analysis. Appreciation is extended to R. G. Joiner for his program management role of our instruments at ONR. We also deeply appreciate the assistance of W. L. Imhof, J. M. Quinn, J. B. Reagan, R. D. Sharp, and E. G. Shelley. The assistance of S. Brown of GSFC was critical to the final calibration of this instrument.

References

[1] Smith, P. H., and Hoffman, R. A., "Ring Current Particle Distributions During the Magnetic Storms of December 16-18, 1971," *Journal of Geophysical Research,* Vol. 78, No. 22, 1973, pp. 4731–4737.

[2] Lyons, L. R., and Evans, D. S., "The Inconsistency Between Proton Charge Exchange and the Observed Ring Current Decay," *Journal of Geophysical Research,* Vol. 81, No. 34, 1976, pp. 6197–6200.

[3] Spjeldvik, W. N., and Fritz, T. A., "Energetic Ionized Helium in the Quiet Time Radiation Belts: Theory and Comparison with Observations," *Journal of Geophysical Research,* Vol. 83, No. A2, 1978, pp. 654–662.

[4] Tinsley, B. A., "Effects of Charge Exchange Involving H and H^+ in the Upper Atmosphere," *Planetary and Space Science,* Vol. 26, 1978, p. 847.

[5] Williams, D. J., "Dynamics of the Earth's Ring Current: Theory and Observation," *Space Science Review,* Vol. 42, 1985, p. 375.

[6] McEntire, R. W., Lui, A. T. Y., Krimigis, S. M., and Keath, E. P., "AMPTE/CCE Energetic Particle Composition Measurements During the September 4, 1984 Magnetic Storm," *Geophysical Research Letters,* Vol. 12, No. 5, 1985, pp. 317–320.

[7] Voss, H. D., Reagan, J. B., Imhof, W. L., Murray, D. O., Simpson, D. A., Cauffman, D. P., and Bakke, J. C., "Low Temperature Characteristics of Solid State Detectors for Energetic X-ray, Ion and Electron Spectrometers," *IEEE Transactions on Nuclear Science,* Vol. NS-29, 1982, pp. 164–168.

[8] Imhof, W. L., Reagan, J. B., Voss, H. D., Gaines, E. E., Datlowe, D. W., Mobilia, J., Helliwell, R. A., Inan, U. S., Katsufrakis, J., and Joiner, R. G., "The Modulated Precipitation of Radiation Belt Electrons by Controlled Signals from VLF Transmitters," *Geophysical Research Letters,* Vol. 10, No. 8, 1983, pp. 615–618.

[9] Voss, H. D., "Energy and Primary Mass Determination Using Multiple Solid State Detectors," *IEEE Transactions on Nuclear Science,* Vol. NS-29, 1982, pp. 178–181.

[10] Forcinal, G., Siffert, P., and Coche, A., "Pulse Height Defects due to Nuclear Collisions Measured with Thin Window Silicon Surface Barrier Detector," *IEEE Transactions on Nuclear Science,* Vol. NS-15, 1968, p. 475.

Appendix 2

SEP Instrument Paper

CRRES Spectrometer for Electrons and Protons

R. W. Nightingale,* R. R. Vondrak,† E. E. Gaines,*
W. L. Imhof,‡ R. M. Robinson,§ S. J. Battel,¶
D. A. Simpson,** and J. B. Reagan††
Lockheed Palo Alto Research Laboratory,
Palo Alto, California 94304

Introduction

IMPORTANT components of the magnetospheric plasma to be explored by the CRRES are the energetic electrons and protons that populate the Earth's radiation belts. The fluxes of these particles depend critically on the production and loss mechanisms in the radiation belts and exhibit dynamic behavior in response to solar and geomagnetic activity.[1,2] The understanding of these processes requires detailed measurements of the particle distribution functions including the pitch angle. Previous measurements of energetic electrons and protons have been made by instruments on satellites such as Ogo 5,[3] SCATHA,[4] (S/C) 1979-053, and (S/C) 1982-019,[1,2] but the unique CRRES orbit offers exciting new possibilities for developing improved models of the inner and outer radiation belts.[5,6] For example, the particle distributions measured along the spacecraft trajectory can be used to map the two-dimensional radiation belt morphology in the orbit plane for $1.05 < L \leq 7$ near the geomagnetic equator.

The ONR 307-3 Spectrometer for Electrons and Protons (SEP) is one component of the ONR 307 Energetic Particles and Ion Composition experiment. SEP measures the energy and pitch angle distributions of energetic electrons and protons throughout the CRRES orbit. The specific science objectives of the SEP experiment are 1) to understand the physics of the sources, losses, energization, transport, and lifetimes of energetic particles in the Earth's radiation belts; 2) to understand the details of wave-particle interactions (WPI), both natural and man made, that result in precipitation of radiation belt particles; and 3) to utilize this experimental data base to greatly improve the accuracy of trapped radiation belt models.

Experiment Description and Operations

The SEP design is based heavily on the successful SC-3 spectrometer[4,7] flown on the SCATHA mission. Unlike the single-detector system used on SCATHA, SEP consists of three solid-state particle spectrometers oriented at 40, 60, and 80 deg from the spacecraft spin axis. A cross-sectional view of one of the telescopes is shown in Fig. 1. Each spectrometer has four detector elements labeled A, D, E, and E′. Various logic combinations of the four detector elements in each spectrometer are used to determine the particle types and energy ranges, which are measured sequentially. The operational modes of each telescope are individually commandable.

The D detector, which is 200-μm-thick intrinsic silicon, is used to measure both the rate of energy loss of the higher-energy particles and to directly stop and measure the low-energy particles. The E detector, which consists of a stack of five 2-mm-thick silicon surface-barrier detectors in parallel, is located behind the D detector to stop the higher-energy particles and to measure their total energy loss. The E′ detector, which is a 1000-μm-thick piece of silicon, is located behind the E detector and is used as an active collimator. Following it is a tungsten absorber that sets the upper energy limit for analysis. The entire telescope-configured stack is surrounded by the anticoincidence A detector, which consists of a plastic scintillator viewed by a photomultiplier tube. The A detector senses and rejects energetic particles and bremsstrahlung that penetrate either the outer shielding walls of aluminum and tungsten or the silicon detector stack and tungsten absorber. The detector stack is located behind a long, narrow collimator that defines the 3-deg angular field of view full width at half maximum (FWHM). The aluminum and tungsten effectively stop electrons with energy up to 5 MeV and bremsstrahlung photons with energy up to about 150 keV.

Each of the three identical SEP particle telescopes has a high-resolution, 3-deg (FWHM) field of view provided by a long collimator (20 cm) containing 10 baffles. The collimators are identical to the ones used on the SC-3 instrument,[4] providing an instrument geometric factor of ~ 3×10^{-3} cm^2-sr. For the 80- and 60-deg telescopes, measurements over 12 energy channels are obtained every 0.25 s with a dead time of 2 ms. Because of telemetry restrictions, the 40-deg telescope accumulates for 0.5 s with a dead time of 4 ms.

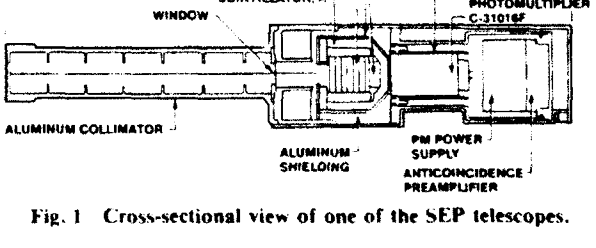

Fig. 1 Cross-sectional view of one of the SEP telescopes.

Received June 18, 1991; revision received Sept. 3, 1991; accepted for publication Sept. 3, 1991. Copyright © 1992 by the American Institute of Aeronautics and Astronautics, Inc. All rights reserved.

*Research Scientist.

†Manager. Associate Fellow AIAA.

‡Consulting Scientist.

§Staff Scientist.

¶Consultant, Battel Engineering. Member AIAA.

**Senior Staff Research Engineer.

††General Manager. Fellow AIAA.

The three SEP spectrometer heads and the analyzer package are shown in Fig. 2. The two units are mounted on the bottom of the spacecraft and are separated to achieve a lower temperature in the silicon detectors for improved low-energy electron detection.[8,9]

Each sensor operates from its own 256, 8-bit word CMOS memory, which is individually addressable and loadable via a 16-bit serial-digital command. Four of these words completely define one operating mode (32-bit control register) for an individual sensor. A mode is defined by specifying the logic conditions (coincidence/anticoincidence), gain, detector for pulse-height analysis, and energy thresholds required between the four detector elements to uniquely establish a particular type and energy range for analysis.[4]

Several modes can be programmed in sequence to emphasize one particle type, to obtain comprehensive measurements for special events such as solar flares, or to dwell on a narrow energy range for any particle type. A hard-wired backup mode that measures the higher-energy electrons (215-5100 keV) is independent of the memory and is used automatically at turn-on and whenever the memory is being loaded or disabled. The basic programmable mode parameters are the energy range and energy channel widths for the electrons and for the protons. Typical modes that may be used during the CRRES mission are shown in Table 1.

Calibration

The SEP sensor heads were calibrated using electron and proton beams from accelerators at the Goddard Space Flight Center (GSFC) in Greenbelt, Maryland, and at Harvard University in Cambridge, Massachusetts. Two accelerators were utilized at GSFC, a low-energy electron machine for energies up to 150 keV and a Van de Graaff accelerator with a maximum energy of 1.5 MeV for both electrons and protons. The sensors were in vacuum at room temperature for these runs. The beam rate of the low-energy accelerator was stable to about 25% at a few thousand counts per second for electrons between 25 and 150 keV. The Van de Graaff accelerator extended the electron measurements to 1500 keV in 10 steps and started the proton range from 500 to 1500 keV in five energy steps.

High-energy proton calibrations were done in air at the Harvard Cyclotron Laboratory for eight energy steps between 35 and 100 MeV. The 159-MeV proton beam was reduced in energy by absorbers that produce a beam energy spread of less than 6% at 90 MeV and above, whereas the spread is about 40% at the lowest energies. The measured energy deposition from higher-energy protons penetrating the detectors was within 1 MeV of calculated values.

Figure 3 shows examples of calibration data for electrons and protons. The spectra of monoenergetic beams were obtained with a laboratory multichannel analyzer and were related to the 12 channels of the flight pulse-height analyzers by voltage levels. The calibration data were used to specify the energy ranges for each mode of each sensor as shown in Table 1. The mode ranges are electronically divided into 12 channels, each approximately having the channel width shown in the table. The energy ranges in Table 1 show some overlap between modes. The particle collimation, the D detector absorption, and the sensor coincidence circuitry combine to significantly reduce the overlap.

Results

SEP commenced normal operations on August 7, 1990, after a successful instrument activation period. Preliminary results are shown in Figs. 4 and 5. Figure 4 shows pitch angle spectrograms for electrons and protons measured during orbit 79 by the sensor that is 80 deg from the spin axis. This orbit occurred several days after the commencement of a moderate magnetic storm (Dst = − 116). Each panel shows the relative flux of electrons or protons integrated over the energy ranges

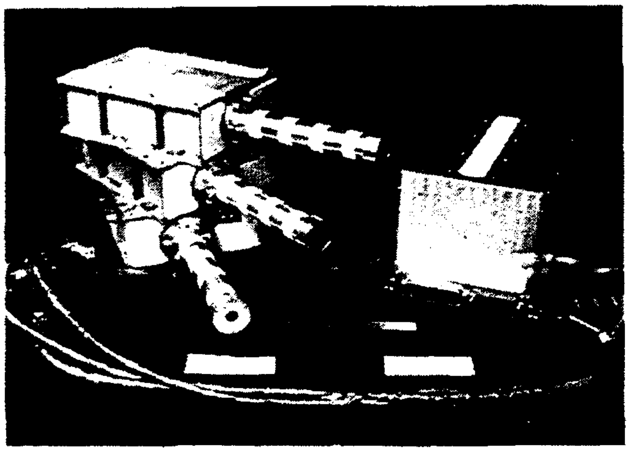

Fig. 2 Photograph of the three SEP telescopes mounted together and the electronics analyzer package.

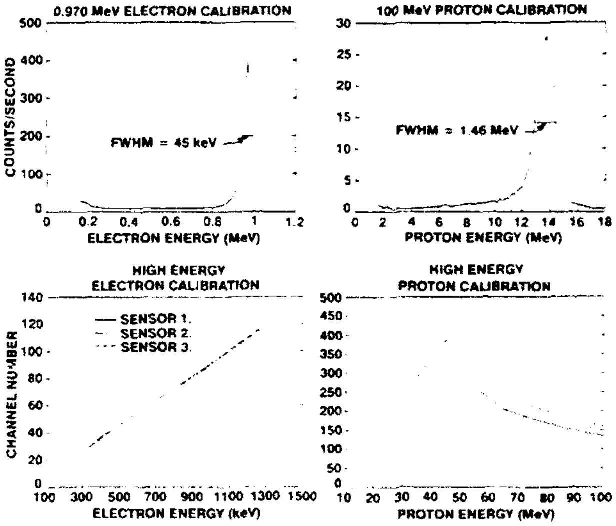

Fig. 3 Examples of calibration data showing typical spectra of the particle beams and the pulse-height responses vs energy in all three sensors for high-energy electrons and protons.

Table 1 SEP initial energy range and channel width

	Sensor A		Sensor B		Sensor C	
Mode	Energy range, MeV	Width, MeV	Energy range, MeV	Width, MeV	Energy range, MeV	Width, MeV
Electron 1	0.042-0.324	0.0235	0.042-0.336	0.0245	0.041-0.313	0.0227
Electron 2	0.164-4.93	0.397	0.171-5.12	0.413	0.170-5.11	0.412
Proton 1	0.875-6.60	0.478	0.916-6.70	0.482	0.920-6.80	0.490
Proton 2	2.5-38.7	3.01	2.2-33.7	2.62	2.0-30.4	2.37
Proton 3	35.8-80.2	3.7	31.2-69.9	3.22	28.2-63.1	2.91
Proton 4	45-94	4.08	45-105	5.00	45-110	5.42
Alphas	6.8-24	1.43	6.90-24.3	1.45	7.00-24.	1.47

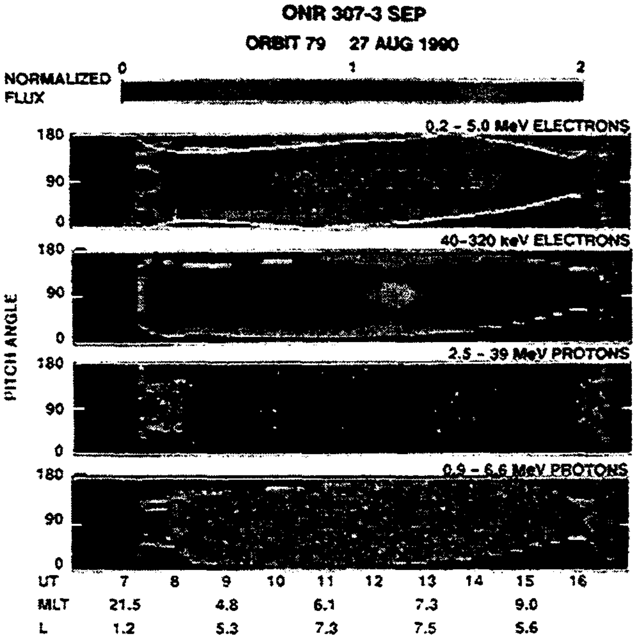

Fig. 4 Pitch angle spectrograms showing relative intensities of electrons and protons measured during orbit 79. The intensities are normalized to the average differential, directional flux measured during the 64-s sampling interval.

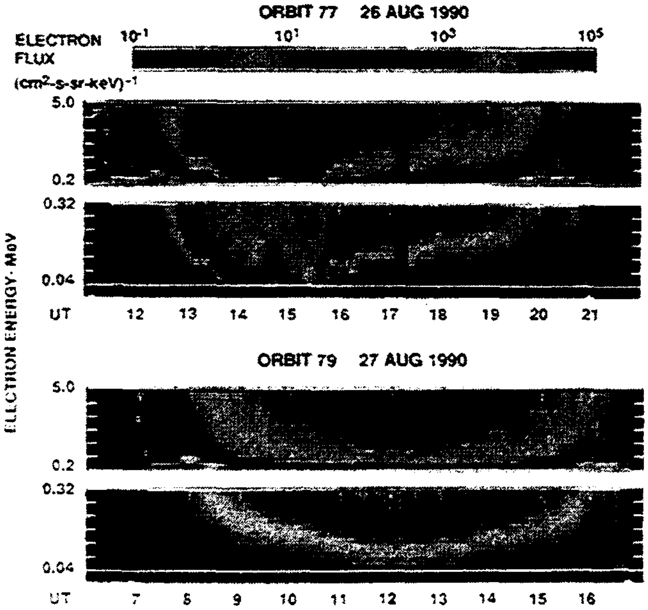

Fig. 5 Energy time spectrograms showing approximately spin-averaged fluxes of electrons during orbits 77 and 79.

indicated in the upper right-hand portion. The intensity is color coded according to the flux in 4-deg-wide pitch angle bins normalized to the average differential, directional flux measured during each sampling interval. A full energy and pitch angle distribution is obtained in 64 s in the normal SEP operating mode. The time axis in the plot is arranged with perigee near the beginning and end and apogee at the center. Note how the pitch angle coverage for this detector varies during the orbit. Depending on the orientation of the magnetic field, data from the other two sensors can extend the pitch angle coverage achievable with a single telescope. Evidence for both pancake and butterfly pitch angle distributions are apparent in this display.

Figure 5 shows energy time spectograms for electrons measured during orbits 77 and 79. The differential number fluxes are averaged over 32 s; because the satellite spin is about 29 s, these are approximately spin-averaged fluxes. The data for each orbit are shown in two panels corresponding to the low- and high-energy electron ranges. The large dropout in fluxes in the first half of the orbit is a result of the magnetic storm that commenced one orbit earlier. Two orbits later, the energetic particle fluxes have recovered. Just after 12 UT in orbit 79 there are three dispersive-like electron events possibly associated with substorm activity.

To obtain the differential particle flux from the SEP data, the counts in each sampling interval are divided by the product of the live time, the spectrometer geometric factor, the energy width of the channel for the particular mode, and the sensor particle detection efficiency for the channel. Pitch angle distributions for each sensor are calculated using the sensor look directions and the magnetic field direction determined from the onboard magnetometer.

Conclusions

The SEP experiment on CRRES operated almost continuously throughout the lifetime of the spacecraft. The data obtained in the CRRES orbit allows the computation of the particle distribution functions in phase space for energetic electrons and protons throughout the radiation belts. These distributions can be used for developing models of both the static and dynamic radiation belt populations. Preliminary work toward a dynamic model has been completed using SCATHA outer-belt electron distributions together with a general solution to a simple form of the simultaneous bimodal (radial and pitch-angle) diffusion equation.[10,11] The SEP data are especially suited for these types of studies because of the good angular resolution and extended pitch angle coverage provided by the three telescopes.

Acknowledgments

This work was primarily supported by the Office of Naval Research under Contract N00014-83-C-0476 and in part by the Lockheed Independent Research Program. The authors wish to thank J. C. Bakke, L. A. Hooker, and V. F. Waltz for their efforts in the design, development, and fabrication of this instrument. We also deeply appreciate the contributions provided at Lockheed by H. D. Voss and J. M. Quinn. Special appreciation goes to the Ball Aerospace Systems Division who built the CRRES satellite; to the USAF Space Test Program and the NASA Marshall Space Flight Center, who shared in the management of the project; to General Dynamics for the successful launch of Atlas-Centaur rocket; and to the USAF Consolidated Space Test Center, which operated the satellite.

References

[1] Baker, D. N., Blake, J. B., Klebesadel, R. W., and Higbie, P. R., "Highly Relativistic Electrons in the Earth's Outer Magnetosphere, 1. Lifetimes and Temporal History, 1979-1984," *Journal of Geophysical Research*, Vol. 91, No. A4, 1986, pp. 4265-4276.

[2] Baker, D. N., Blake, J. B., Callis, L. B., Belian, R. D., and Cayton, T. E., "Relativistic Electrons Near Geostationary Orbit: Evidence for Internal Magnetospheric Acceleration," *Geophysical Research Letters*, Vol. 16, No. 6, 1989, pp. 559-562.

[3] West, H. I., Jr., Buck, R. M., and Walton, J. R., "Electron Pitch Angle Distributions Throughout the Magnetosphere as Observed on Ogo 5," *Journal of Geophysical Research*, Vol. 78, No. 7, 1973, pp. 1064-1081.

[4] Reagan, J. B., Nightingale, R. W., Gaines, E. E., Imhof, W. L., and Stassinopoulos, E. G., "Outer Zone Energetic Electron Spectral Measurements," *Journal of Spacecraft and Rockets*, Vol. 18, No. 1, 1981, pp. 83-88.

[5] Teague, M. J., and Vette, J. I., "The Inner Zone Electron Model AE-5," National Space Science Data Center/World Data Center A for Rockets and Satellites, Rept 72-10, Nov. 1972.

[6] Singley, G. W., and Vette, J. I., "The AE-4 Model of the Outer Radiation Zone Electron Environment," NSSDC 72-06, Aug. 1972.

[7] Stevens, J. R., and Vampola, A. L., "Description of the Space Test Program P78-2 Spacecraft and Payloads," Space and Missile Systems Organization, Air Force Systems Command, TR-78-24, Los

Angeles Air Force Station, Los Angeles, CA, Oct. 1978.

[8]Voss, H. D., Reagan, J. B., Imhof, W. L., Murray, D. O., Simpson, D. A., Cauffman, D. P., and Bakke, J. C., "Low Temperature Characteristics of Solid State Detectors for Energetic X-ray, Ion and Electron Spectrometers," *IEEE Transactions on Nuclear Science*, Vol. NS-29, No. 1, 1982, pp. 164-168.

[9]Voss, H. D., Bakke, J. C., and Roselle, S. N., "A Spacecraft Multichannel Analyzer for a Multidetector Solid State Detector Array," *IEEE Transactions on Nuclear Science*, Vol. NS-29, No. 1, 1982, pp. 173-177.

[10]Chiu, Y. T., Nightingale, R. W., and Rinaldi, M. A., "Simultaneous Radial and Pitch Angle Diffusion in the Outer Electron Radiation Belt," *Journal of Geophysical Research*, Vol. 93, No. A4, 1988, pp. 2619-2632.

[11]Chiu, Y. T., Rinaldi, M. A., and Nightingale, R. W., "Toward Dynamic Modeling of the Outer Electron Radiation Belt," *Journal of Geophysical Research*, Vol. 95, No. A8, 1990, pp. 12,069-12,074.

Appendix 3

Neutral Atom Imaging Paper

Satellite observations and instrumentation for imaging energetic neutral atoms

H. D. Voss, J. Mobilia, H. L. Collin, and W. L. Imhof

Space Sciences Laboratory, 0/91-20 B/255
Lockheed Palo Alto Research Laboratory
3251 Hanover Street, Palo Alto, CA 94304

ABSTRACT

Direct measurements of energetic neutral atoms (ENA) and ions have been obtained with the cooled solid state detectors on the low altitude (220 km) three-axis stabilized S81-1/SEEP satellite and on the spinning 400 km × 5.5 Re CRRES satellite. During magnetic storms ENA and ion precipitation ($E > 10$ keV) is evident over the equatorial region from the LE spectrometer on the SEEP payload (ONR 804). The spinning motion of the CRRES satellite allows for simple mapping of the magnetosphere using the IMS-HI (ONR 307-8-3) neutral spectrometer. This instrument covers the energy range from 20 to 1000 keV and uses a 7 kG magnetic field to screen out protons less than about 50 MeV. ENA and the resulting low-altitude ion belt have been observed with the IMS-HI instrument. Recently, an advanced spectrometer (SEPS) has been developed to image electrons, ions, and neutrals on the despun platform of the POLAR satellite (~1.8 × 9 Re) for launch in the mid-90's as part of the NASA ISTP/GGS program. For this instrument a 256 element solid state pixel array has been developed that interfaces to 256 amplifier strings using a custom 16 channel microcircuit chip. In addition, this instrument features a motor controlled iris wheel and anticoincidence electronics.

2. INTRODUCTION

Energetic neutral atoms are an important tracer of energetic ion collisions with neutrals in solar and planetary plasmas[1]. Global scale images of the earth's ring current ($2<L<4$) may be remotely sensed from either above the earth's radiation belt[2] or from below the radiation belt at low altitude[3]. Neutral atoms can therefore provide a mapping of the internal composition, spatial geometry, and temporal changes of the ring current, weighted by the appropriate cross sections and neutral hydrogen density; it provides a powerful method of studying the magnetosphere.

The source of energetic neutral atoms (ENA) is believed to be a double-charge-exchange process of ions originating in the ring current [4,5] as shown in

0-8194-0917-0/92/$4.00

Figure 1. The trapped ions of the ring current, by charge exchange with thermal hydrogen atoms of the geocorona, become high velocity neutral atoms which are focused, for those directed toward the earth, in the equatorial atmosphere where they again become ions by ionization collisions. The injected energetic neutrals at low altitudes produce the equatorial precipitation zone and a temporary low altitude ion belt between 200 and 1000 km as illustrated in Figure 1.

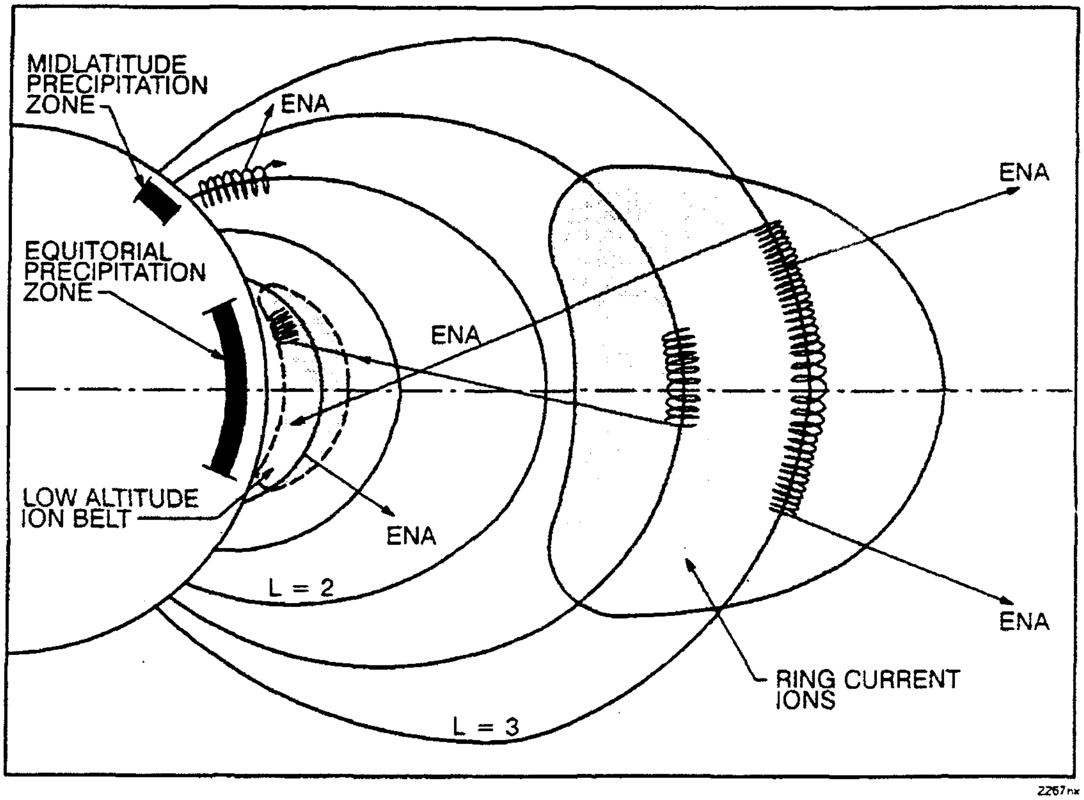

Fig. 1. Schematic representation of the ENA and resulting low altitude ion belt and precipitation.

3. RING CURRENT NEUTRALS AT LOW-ALTITUDE

The low-altitude ion belt cannot be the result of stably trapped particles since the ion lifetime is much less than the drift period. Figure 2 shows the equatorial zone of particle precipitation[6] as it appears in satellite measurements of particles by Hovestadt et al.[7], Moritz[4], Mizera and Blake[8], Butenko et al.[9], Scholer et al.[10], and Meier and Weller[11]. The intensities have been normalized to unity at the maximum. The data were taken during moderately disturbed times. The zone typically covers the region of ± 20 degrees in latitude from the geomagnetic equator.

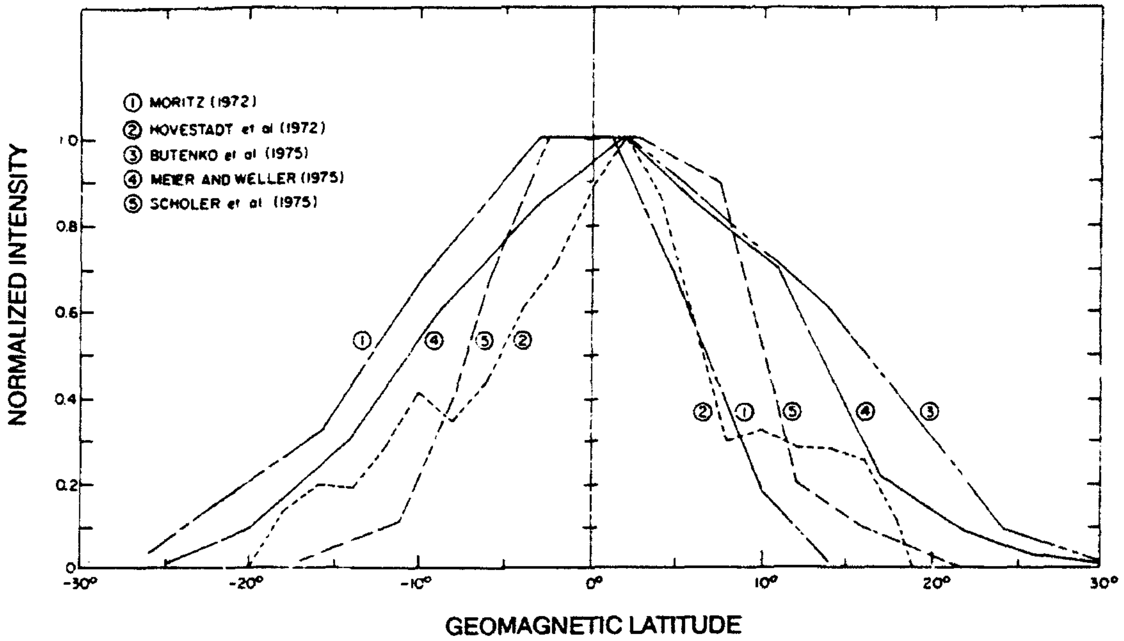

Fig. 2. The nighttime equatorial zone as it appears in satellite observations of particle flux and UV airglow. The intensity is normalized to the maximum value [6].

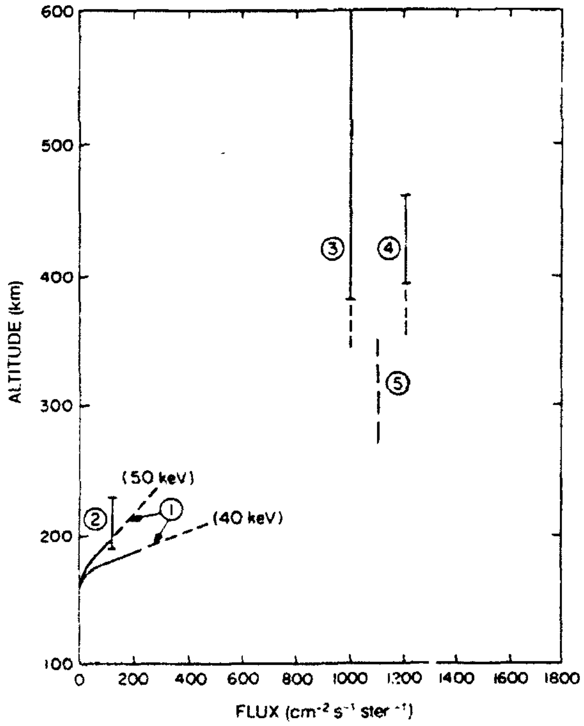

Fig.3. Rocket and satellite data of ions and neutrals at the equator. 1 is from Voss and Smith[12], 2 is from Butenko et al.[9], 3 is from Moritz[4], 4 is from Mizera and Blake[8] and 5 is based on the S81-1/SEEP data after the 13 July 1982 magnetic storm.

Low altitude rocket[12] and satellite measurements[4] at the equator (Figure 3) indicate that the ions are concentrated at 90° pitch angle with an altitude profile which increases rapidly in intensity between 180 and 260 km and becomes nearly independent of altitude thereafter. Because the loss process for ions increases with atmospheric density the source must also increase with atmospheric density to maintain a constant flux profile between 300 and 1000 km. The inferred source mechanism is the charge exchange process of ring current ions which is illustrated in Figure 1. The low altitude energy spectrum is similar to that of the ring current, with most of the particles having energies between $10 < E < 100$ keV and with the spectrum extending above 1 MeV. The precipitation rate is on the order of 10^{-3} ergs $cm^{-2} s^{-1}$.

4. S81-1 SATELLITE OBSERVATIONS

From May to December 1982, the SEEP payload on the three axis stabilized S81-1 polar satellite made high sensitivity measurements of precipitating energetic electrons and ions in the altitude region 170 to 270 km. The payload included an array of passively cooled solid-state detectors[13] covering the energy range from 2 to 1000 keV in 256 channels. The sensors had a geometrical factor of 0.17 cm^{2}ster and a field-of-view of ± 20°.

The SEEP data during the 13 - 14 July magnetic storm[14] is shown in Figures 4 and 5. The prominent equatorial zone is observed between geomagnetic latitudes of ± 20° and is stable and repeatable in form during each equatorial pass. The twin peaks in the ion flux (i.e. maxima displaced ± 10° in latitude about the geomagnetic equator) are consistent with the north and south side lobes of the temporary ion radiation belt (Figure 1).

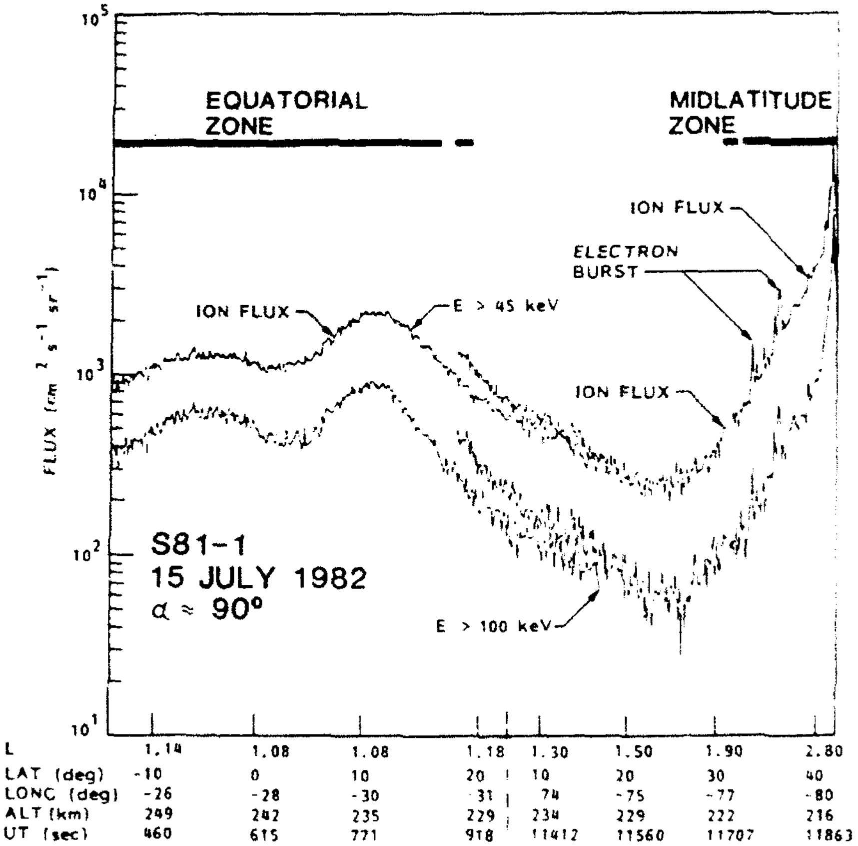

Fig. 4. Low altitude S81-1/SEEP satellite observations of precipitating energetic particles in the midlatitude and equatorial zones [14].

The temporal variations of ions in the equatorial zone are shown in the top panel of Figure 5. In the center panel the L shell variation of the plasma trough location and the equatorward auroral boundary (EAB) location are shown and indicate the relative compression of the magnetosphere and the displacement of the auroral zone to middle latitudes. The magnetic indices Kp and D_{st} are shown in the lower panel. Near 01:00 hours UT on 14 July 1982 the storm reaches a maximum (D_{st} = -325) and the equatorial zone ion flux is observed to simultaneously increase by a factor of about 500 over pre-storm levels. The energetic equatorial neutrals and ions, however, remain high ($\sim 10^3 cm^{-2} s^{-1}$) after the storm and confirm the development of a low latitude (L ~ 1.14) ion radiation belt during the storm main phase that decays relatively slowly in time producing the equatorial zone ionization. The similarity of the day and night intensity and slow temporal variation of energetic particles in the equatorial zone indicate the global extent of ion precipitation.

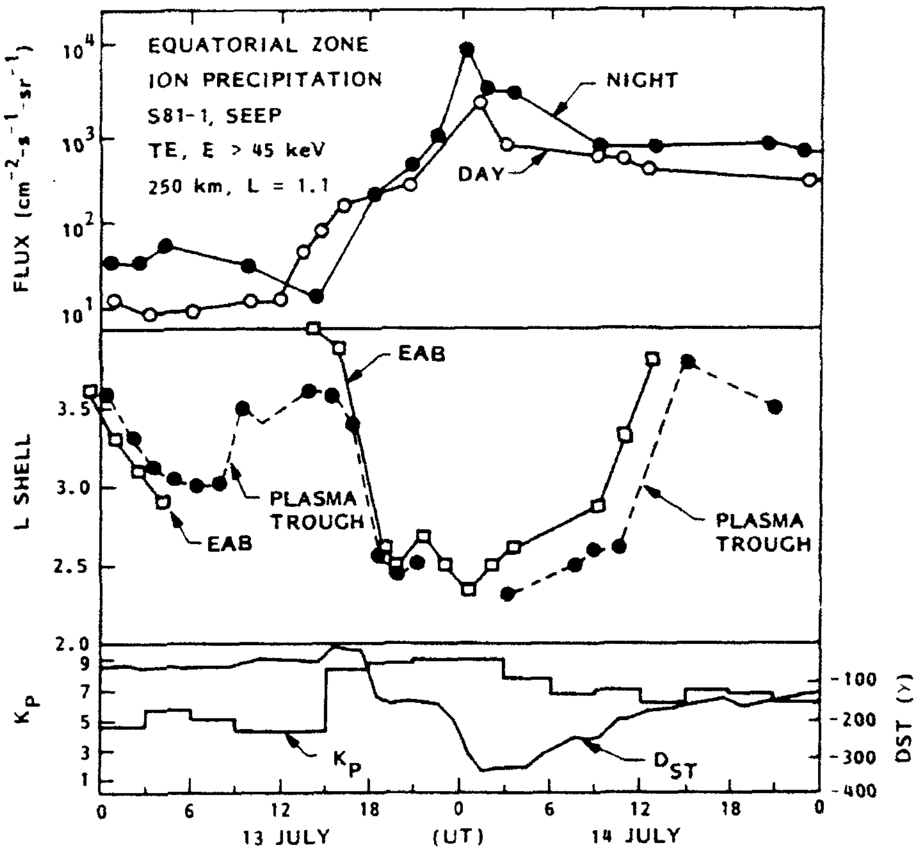

Fig. 5. Variation of equatorial zone ENA/ion precipitation during the magnetic storm of 13-14 July 1982. The location of the plasma 13-14 July 1982. The location of the plasma (EAB) are also shown [14].

5. CRRES ION MASS AND NEUTRAL ATOM SPECTROMETER

The contiguous mapping of the particle distribution by the CRRES satellite over the radial distance range from 400 km to 5.5 Re near the equatorial plane provides a comprehensive data base that can be used for studies of the radiation belt and ring current. The primary objective of the medium energy ion mass spectrometer (IMS-HI) on the CRRES satellite was to obtain the necessary data to construct models of the energetic ion (10 to 2000 keV-AMU/q^2) and neutral atom (10 to 1500 keV) environment of the Earth's radiation belts. The spectrometer[15] measured the energetic ion composition, energy spectrum, charge, and pitch angle distribution with good mass, temporal, and spatial resolution. Additionally simultaneous mass and energy analysis at relatively large geometrical factors (10^{-3} to 10^{-2} cm^{2}ster) was obtained.

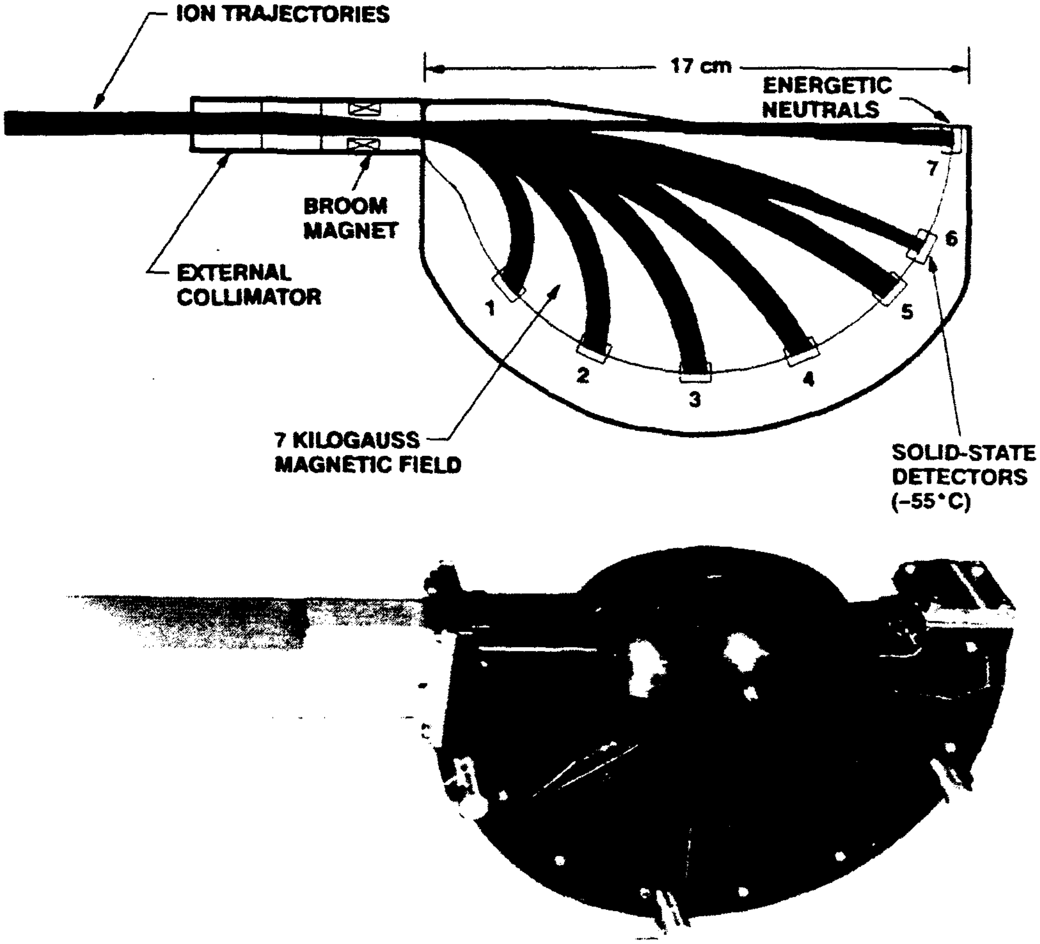

Fig. 6. The IMS-HI instrument on CRRES uses ion momentum, mass defect, and energy analysis from a 7 kG magnet and an array of cooled solid-state detectors. The magnet is shown in the lower portion of the figure and the ENA and ion optics in the upper portion.

The instrument principle of operation is illustrated in Figure 6 and is based on ion momentum separation in a 7kG magnetic field followed by energy and mass defect analysis using an array of cooled (-50°C) silicon solid-state detectors. The entrance collimator consists of a series of rectangular baffles that define the ion and neutral beam angular resolution and a broom magnet to reject electrons with energy less than 1 MeV. A seventh sensor, located directly in line with the collimator, measures energetic neutrals and has an ion rejection of approximately 50 MeV-AMU/q^2. In principal the spin of the satellite and orbit motion can be used to "raster scan" a portion of the magnetospere to obtain a neutral atom image. In practice, however, the duty cycle associated with the spinning of the satellite and the background of the radiation belts make this a difficult task from CRRES.

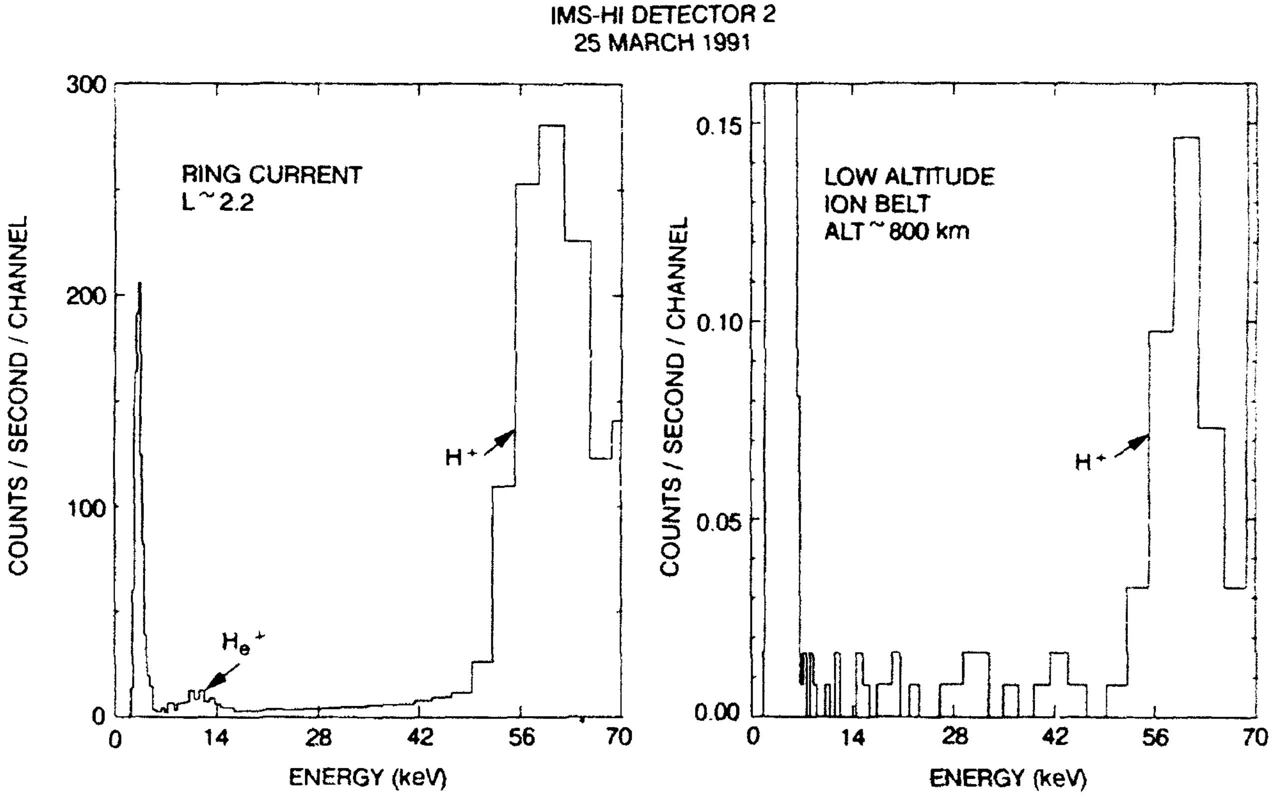

Fig. 7. Mass spectrograms on 25 March 1991 from the IMS-HI instrument on CRRES of the low altitude ion belt which is understood to be the result of ENA and the associated ring current mass spectrogram at L~2.2.

Near perigee (<1000km), when CRRES is below the inner belt, the IMS-HI instrument is able to directly view the ring current neutrals and ion composition of the low-altitude ion belt. Above the inner belt the IMS-HI instrument is able to make cross-sectional cuts of the ring current ion composition. About one day after the large magnetic storm of 24 March 1991 the ring current ions were observed to increase and move to lower altitudes. The ring current flux at this time extends down to L~2.0 and is dominated by hydrogen at E~60 keV. O+, O++, and He+ are one to two orders of magnitude less in flux at these energies.

The ENA transported to low altitude is again charge exchanged by the atmosphere and temporarily becomes the low-altitude ion belt. Because the ions cannot support drift motion in much of the belt the loss rate is high. The steady-state ion population to first order is a mapping of the source composition multiplied by the appropriate atmospheric loss rates. A mass spectrogram of the low altitude ion belt for detector two is shown for the first time in figure 7 for 25 March 1992. Also shown for comparison is the mass spectrogram of detector two near the inside edge of the ring current at L~ 2.2. At this time the prominent ion, inferred from the ring current ENA is H^+ at 60 keV. The average low-altitude hydrogen count rate is about 2000 times lower than the average count rate in the ring current for the IMS-HI spectrometer.

6. SEPS ENERGETIC PARTICLE IMAGER

SEPS (Source-Loss/Cone Energetic Particle Spectrometer) is to be flown in the mid-90's on the POLAR Satellite in the NASA ISTP Program. Because SEPS is mounted on the POLAR spacecraft despun platform and is capable of imaging particles over a 24° × 48° field-of-view in the nadir and zenith directions the particle "source cone" and "loss cone" can be monitored continuously and simultaneously. In addition, over the polar caps, SEPS will be able to image ENA.

The ion/neutral telescope on SEPS has 128 XY pixel elements over a 1 in^2 by 200 micron deep solid state detector. A strong broom magnet rejects electrons from the entrance collimator of the SEPS pinhole camera. A SiLi detector behind the XY detector is used for anticoincidence. The instrument is designed to cover the energy range from 30 keV to 10 MeV.

In addition to the SEPS ion/neutral telescope the "electron" telescope of SEPS can measure ions and neutrals above 300 keV in 256 pixels over 2 in^2. For this telescope a motor driven iris can change the aperture size upon command thereby optimizing the instrument's geometrical factor and associated spatial resolution. Unique electron, ion, and neutral particle images are expected with 100% duty cycle. The SEPS instrument mass is 3.4 kg, the power consumption 3.5W, and the telemetry rate is 1.2 kbps.

7. ADVANCED MICROCIRCUIT TECHNOLOGY FOR IMAGING SPECTROMETERS

State-of-the-art sensors and electronics are required on future instrumentation to perform energetic particle imaging and spectroscopy within spacecraft resources. Neutral atom imaging requires large geometrical factor sensors with multi-pixels and good background rejection. Background rejection can be improved by using anticoincidence detectors (as in SEPS), electric and magnetic field deflectors in the optical path, coincidence time-of-flight techniques, and coded aperture devices to improve signal-to-noise.

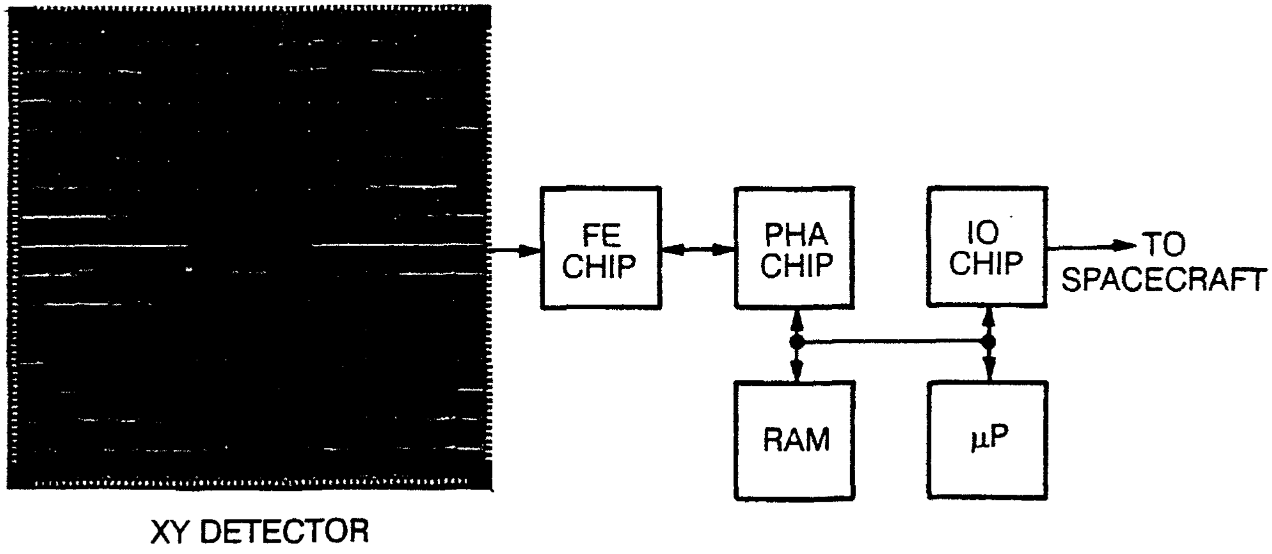

Fig. 8. System block diagram of an advanced microcircuit detector and analog/digital microchips to spectroscopicly image energetic particles.

A recent review of instrumentation techniques for the remote sensing of space plasmas in the heliosphere via energetic neutral atoms has been presented by Hsieh et al.[1] Much of the proposed new instrumentation is based on rather sophisticated sensor electronics demands. To simplify instrument development and greatly reduce instrument spacecraft resource requirements the development of advanced microcircuits, solid-state detectors, and microchannel plate sensors have been pursued. Figure 8 illustrates the key modules which have been developed as part of the SEPS program.

To minimize capacitance (i.e. low energy threshold) and crosstalk a 1 in^2 by 200 micron thick solid state sensor was developed with Hamamatsu Inc. that has 256 pixels with individual readouts (Figure 8). The proton dead zone for this device was found to be 8 keV and has an energy resolution at room temperature of 2 keV FWHM.

Thousands of sensor elements require microcircuit technology to amplify and process the data. To achieve this an advanced CMOS mixed mode (combined analog and digital) gate array microcircuit was developed that is radiation hard. A gate array is a matrix of transistors on a microcircuit that can be interconnected for unique circuit functions. Because the matrix is mass produced and well characterized (semi-custom) the risk, cost, and turnaround are significantly reduced compared to a full custom microcircuit. The arrays are highly reliable since they significantly reduce the number of bonds and PC board parts and permit a parallel system architecture.

The first circuit developed on the rad-hard array (Figure 8) is a 16 channel amplifier chip that features; 1) 0.5 microsecond shaping, 2) peak detection, 3) 32 individual comparators with D to A control, and 4) coincidence and anticoincidence logic. To date, a single channel version of this chip has been tested. The input preamplifier is designed to work with a microchannel plate or sensor in a DC coupled mode to a solid state detector.

The second circuit developed is a pulse height analyzer (PHA) chip that can accumulate counts in an external RAM according to energy and position. It also includes eight 17 bit counters and a 16 level flash A to D converter for log or linear analysis.

The third chip features the necessary IO functions to interface with the spacecraft and the onboard microprocessor. Some of the features of the IO circuit include 1) 8-bit D to A converter with calibrate pulse output, 2) eight multiplexed inputs to a 8 bit A to D converter, 3) interrupt controller, 4) 16-bit counter timer, 5) address decoding, 6) parallel port, 7) serial port, and 8) internal clock processing.

8. CONCLUSIONS

Global geospace cannot be effectively observed by multiple *in situ* measurements. The dynamics of the ring current are only partially understood [16]. The ability to remotely sense the heliosphere via ENA may significantly improve our understanding of the large scale dynamics of planetary magnetospheres and shocks. Many rocket and satellite measurements to date have indicated the credibility of ENA and the resulting low-altitude ion fluxes. The recent CRRES data has now made it possible to compare the ion composition of the ring current with the energetic neutrals and the resulting ion composition at low altitudes.

Future instrumentation must be carefully designed to maintain a large geometrical factor with a high background rejection capability. Although the SEPS instrument geometrical factor is small, its ability to stare at the ring current when over the polar cap for several hours will improve the signal-to-noise ratio.

The implementation of several new technologies makes ENA imaging an attractive diagnostic tool for mapping the global particle environment.

9. ACKNOWLEDGMENTS

The work at Lockheed was supported in part by the Office of Naval Research under contract N00014-83-C-0476 and by the Lockheed Independent Research Program. We thank all of our colleagues at LPARL who have contributed to the various programs mentioned above. In particular we thank Dr. J.R. Kilner and Mr. R.A. Baraze for their efforts in the development of the SEPS instrument and microcircuits.

10. REFERENCES

1. K.C. Hsieh, C.C. Curtis, C.Y. Fan, and M.A. Gruntman, "Techniques for the Remote Sensing of Space Plasma in the Heliosphere via Energetic Neutral Atoms: a Review", in press,1992.

2. E.C. Roeloff, D.G. Mitchell, and D.J. Williams, "Energetic Neutral Atoms (5-50 keV) from the Ring Current, Imp 7/8 and ISEE-1", J. Geophys. Res., 90, 10991-11008,1985.

3. H.D. Voss, W.L. Imhof, and J. Mobilia, "Satellite Observations of Energetic Ions and Neutrals in the Equatorial Precipitation Zone", Proceedings Yosemite '84 Planetary Plasma Environments: A Comparative View, ed. C.R. Clauer and J.H. Waite, Jr., 95-96, 1984.

4. J. Moritz, "Energetic Protons at Low Altitudes: A Newly Discovered Radiation Belt Phenomenon and its Explanation", Z. Geophys., 38, 701,1972.

5. B.A. Tinsley, Neutral Atom Precipitation- a Review, J. Atmos.Terr. Phys., 43, 617, 1981.

6. H.D. Voss and L.G. Smith, "Global zones of energetic particle precipitation", J. of Atmos. and Terr. Phys., 42, 227-239

7. D.B. Hovestadt, B. Hausler, and M. Scholer, "Observations of energetic particles at very low altitudes near the geomagnetic equator", Phys. Rev. Lett., 28, 1340-1344, 1972

8. P.F. Mizera and J.B. Blake, "Observations of Ring Current Protons at Low Altitudes", J. Geophys. Res., 78, 1058-1062, 1973.

9. V.D. Butenko, O.R. Grigoryan, S.N. Kuznetsov, G.S. Malkiel, and V.G. Stolpvskii, "Proton Currents with Ep>70 keV at Low Altitudes in the Equatorial Region", Kosmecheskie Issledovaniya, 13, 508-512, 1975.

10. M. Scholer, D. Hovestadt, and G. Morfill, "Energetic He^+ Ions from the Radiation Belt at Low Altitudes Near the Geomagnetic Equator", J. Geophys. Res., 80, 80-85, 1975.

11. R.R. Meier and C.S. Weller, "Observations of Equatorial EUV Bands: Evidence for Low-Altitude Precipitation of Ring Current Helium", J. Geophys. Res., 80, 2813-2818, 1975.

12. H. D. Voss and L.G. Smith, "Rocket Observations of Energetic Ions in the Nighttime Equatorial Precipitation Zone", COSPAR Advances in Space Exploration, 8, 131-134, 1979.

13. H.D. Voss, J.B. Reagan, W.L. Imhof, D.O. Murray, D.A. Simpson, D.P. Cauffman, and J.C. Bakke, "Low Temperature Characteristics of Solid State Detectors for Energetic X-ray , Ion and Electron Spectrometers", IEEE Trans. Nucl. Sci., NS-29, 164-168, 1982.

14. H.D. Voss, W. L. Imhof, J. Mobilia, E. E. Gaines, and J. B. Reagan, "Energetic Particles in the Nighttime Middle and Low Latitude Ionosphere", Adv. Space Res., 5, 175-178, 1984.

15. H.D. Voss, E. Hertzberg, A.G. Ghielmetti, S.J. Battel, K.A. Appert, B.R. Higgins, D.O. Murray, and R.R. Vondrak, "The Meduim Energy Ion Mass and Neutral Atom Spectrometer (ONR-307-8-3)", in press, J. Spacecraft and Rockets, 1992.

16. D.J. Williams, " Dynamics of the Earth's Ring Current: Theory and Observations", Space Sci. Rev., 42, 375,1985.

Appendix 4

Abstracts of Papers Presented

CRRES IMS-HI Energetic Ion Composition Measurements During the August 1990 and March 1991 Storms

H.D. Voss J. Mobilia and R.A. Baraze (Lockheed Palo Alto Research Laboratory, 3251 Hanover St., Palo Alto, CA 94304)

The energetic ion composition (10 to 2000 keV-AMU/q^2) during the 26 August 1990 and 24 March 1991 storms provides unique insight into the dynamics of the radiation belts compared to quiet-time profiles. The IMS-HI (ONR 307-8-3) spectrometer on the CRRES satellite measures the energetic ion composition, energy spectrum charge, and pitch angle distribution with good mass, temporal, and spectral resolution. One of the *instrument* detectors measures neutrals with ion rejection of < 100 MeV/AMU/q^2. Because IMS-HI has a relatively large geometric factor and 100% duty cycle the instrument is well suited for mapping the fluxes of radiation belt H^+, He^+, O^+, O^{++}, and neutrals during quiet time periods and for the study of wave-particle interactions and the loss-cone fluxes. For the August storm ULF waves in H^+ and O^+ are observed as precursors to the sudden commencement and occur in both storms during several of the injection events. A product of the IMS-HI investigation is to obtain an energetic particle database of the penetrating radiation fluxes for specifying and modeling the radiation belt environment.

1. 1991 Fall Meeting

2. 001387177

3. (a) H.D. Voss
   Dept. 91-20, Bldg. 255
   Lockheed
   Palo Alto
   Research Lab.
   3251 Hanover St.
   Palo Alto, Ca.
   94304

   (b) (415) 424-3299

   (c) (415) 424-3333

4. SM

5. (a) SH01-The Solar Heliospheric and Magnetospheric environment : March 21- April 9,1991
   (b) 2720-Energetic Particles-Trapped

6. Oral

7. 0%

8. Invoice P.O.
   ZAP24279
   Dept. 90-11, Bldg.
   201
   Lockheed
   3251 Hanover St.
   Palo Alto, Ca. 94304
   Attn. Janet Thomas
   (415) 424-2810

9. Contributed

Observations from the IMS-HI (ONR 307-8-3) Energetic Neutral and Ion Composition Instrument on the CRRES Satellite

J. Mobilia H .D. Voss and R.A. Baraze (Lockheed Palo Alto Research Laboratory, 3251 Hanover St., Palo Alto, CA 94304)

Observations made with the IMS-HI (ONR 307-8-3) energetic neutral and ion composition instrument on the CRRES satellite will be presented. CRRES was launched into a geosynchronous transfer (350 x 33500 km) orbit on 25 July 1990 at an inclination of 18.1 degrees and period of ~10 hours. The IMS-HI spectrometer simultaneously measures mass, charge, and energy for 10 to 2000 keV-AMU/q^2 ions with high time resolution and 100% duty cycle. The instrument consists of seven detectors with the seventh measuring neutrals in the 10 to 1500 keV range. The major magnetospheric ions, H^+, He^+, O^+, and O^{++} are measured with high sensitivity which allows good radiation belt mapping. Intensity modulations in the particle distribution have been observed on numerous occasions and will be discussed. The energetic neutral atoms and ion composition profiles are used as a basis for developing models of the radiation belt populations.

1. 1991 Fall AGU meetin

2. 001636642

3. (a) J. Mobilia
   Dept. 91-20, Bldg. 255
   Lockheed
   Palo Alto
   Research Lab.
   3251 Hanover St.
   Palo Alto, Ca. 94304

   (b) (415) 424-3292

   (c) (415) 424-3333

4. SM

5. (b) 2720-Energetic

   particles
   -Trapped

6. Poster

7. 0%

8. Invoice P.O. ZAP24279
   Technical Information
   Dept. 90-11, Bldg. 201
   Lockheed
   3251 Hanover St.
   Palo Alto, Ca. 94304
   ATTN. Janet Thomas
   (415)424-2810

9. Contributed

CRRES Energetic Particles and Ion Composition Measurements During the March 1991 Storm

R M Robinson, H L Collin, H D Voss, R R Vondrak, R W Nightingale and W L Imhof, (Lockheed Palo Alto Research Laboratory, 3251 Hanover St., Palo Alto, CA 94304)

The ONR 307 experiment package on the Combined Release and Radiation Effects Satellite (CRRES) consists of three different types of instruments that measure particle fluxes and ion composition with good temporal and angular resolution. The Spectrometer for Electrons and Protons (SEP) measures electrons with energies from 40 keV to 5 MeV and protons with energies between 900 keV and 40 MeV. The low energy ion mass spectrometer (IMS-LO) measures electrons and major ions between 110 eV and 35 keV. The medium energy ion mass spectrometer (IMS-HI) measures the composition of ions at ring current energies. The development of the March 1991 storm over the energy ranges and particle types sampled by the ONR 307 instruments will be described. The SEP instrument monitored the dramatic increases in energetic electrons and protons associated with the storm including the onset of the solar proton event at 1100 UT on 23 March and the second proton belt beginning at 0400 UT on 24 March. The IMS-LO data show persistent dispersive signatures in the ion fluxes that are suggestive of multiple injection events. Dynamic variations in the low energy plasma fluxes were observed near apogee in association with the storm. The IMS-HI measurements provide information about the behavior of the ring current. The data from these three experiments are intercompared to study the relative responses of electrons and ions over a broad energy range throughout the storm period.

1. 1991 Fall Meeting

2. 001385846

3. R. M. Robinson
Dept 91-20, Bldg 255
Lockheed
3251 Hanover St.
Palo Alto, CA 94304
(415) 424-3296

4. SM

5. (a)SH01-The solar, heliospheric and magnetospheric environment: March 21-April 9, 1991
(b)2720-Energetic particles-trapped

6. O

7. 0

8. Invoice P.O. ZAP24235
Technical Information
Dept 90-11, Bldg 201
Lockheed
3251 Hanover St.
Palo Alto, CA 94304
Attn: Jan Thomas
(415)424-2810

9. Contributed

Spring Agu 1992

Intense >10 MeV Particle Injection Near L=2.5 During the 24 March 1991 Magnetic Shock

H D Voss W L Imhof M Walt J Mobilia R M Robinson and
R W Nightingale
(Lockheed Palo Alto Research Laboratory,
3251 Hanover St, Palo Alto, CA 94304)

On 24 March 1991 a strong magnetospheric shock reached the Earth at 3:42 UT. Between 3:42 and 3:54 the ONR 307 instruments on the CRRES satellite measured impulsive bursts of >10 MeV electrons, protons, and alphas in the slot region ($2.1 < L < 2.5$) near the equator at 3 MLT. The electron bursts are consistent with drift echos of about 15 MeV while the protons are consistent with drift echos of >20 MeV. Particle measurements were obtained with the High-Energy Ion Mass Spectrometer (IMS-HI) and the Spectrometer for Electrons and Protons (SEP) which are part of the ONR 307 experiment on CRRES. IMS-III uses a 7 KG magnet and 7 solid-state detectors to analyze ion mass and energy. No medium energy 18 keV $< E <$ 1.5 MeV ion bursts were observed at this time. However, in the neutral detector, which is also sensitive to protons with $E>50$ MeV, a particle burst was observed 0.5 minutes before the electron peak. SEP employs a telescope of three solid-state detectors and is surrounded by a scintillator. During the burst event the instrument scanned through 8 logic modes to measure electrons (40 keV $< E <$ 5 MeV), protons ($0.9 < E < 100$ MeV), and alphas ($7 < E < 24$ MeV). Simultaneous injection/acceleration of > 10 MeV particles at $L \sim 2.5$ with a sudden commencement is surprising and suggests that an unexpected acceleration mechanism is active in that region.

Acceleration of Particles to > 10 MeV at L=2.5 during a Sudden Commencement

H. D. VOSS (Lockheed Palo Alto Research Laboratory, Palo *Alto, California 94304*)

Simultaneous injection/acceleration of >10 MeV particles at L of about 2.5 with a magnetic storm onset is surprising and suggests a powerful injection mechanism. On 24 March 1991, between 0342 and 0354 UT, the particle instruments on the CRRES satellite observed impulsive bursts of >10 MeV electrons, protons and alphas in the slot region (2.1<L<2.5) near the equator at 0300 MLT. The origin of this event is puzzling and any proposed theory must explain the following key data: 1) the narrow longitude spread and brief interval of injection inferred from the short 5 s pulse width of the electrons, 2) the preferential acceleration of high energy electrons, protons and alphas of MeV energies, 3) the greater injected particle energy at lower L, 4) the 30 second delay between proton and electron peaks, and 5) the nearly simultaneous acceleration of particles with a sudden commencement. To investigate the first order physics, a simple model was formulated using a dipole earth field and a dynamic magnetosphere produced by an approaching image dipole. Using the 100 gamma increase observed on CRRES over a 40 s interval the standoff distance drops to about 3 Re. Particles initially near noon at 3<L<10 are transported below 3 Re and accelerated (a factor of about 10 for 7 Re initial position) by adiabatic compression assuming that the first invariant is conserved. Because of the compression, the constant B particle drift contours are shifted sunward so that the slot region has momentary *direct access* to the magnetosphere acceleration region. For >10 MeV particles the longitude drift periods are short (<3 min.) allowing the particles to drift out of the compression region to low L on the night side. After the initial magnetopause compression to ~ 3 Re it appears that the standoff distance retreats in about 1 minute to somewhat larger distances so that the >10 MeV particles injected into the slot region violate the third invariant.

1. 1992 Fall meeting
2. 001387177
3. (a) H.D. Voss
   Dept. 91-20, Bldg. 255
   Lockheed Palo Alto Researc
   Laboratory
   3251 Hanover St.
   Palo Alto, CA 94304

   (b) (415) 424-3299
4. SM (Magnetospheric Physics)
5. (a) SM03
   (b) 2720,2788
6. oral
7. 0%
8. P.O. No.ZAP25167
   Technical Information Center
   Lockheed Palo Alto Research
   Laboratory
   Dept. 90-11, Bldg. 201
   3251 Hanover St.
   Palo Alto, CA 94304
   Attention: Janet Thomas
   415-424-2810
9. Contributed

SATELLITE INSTRUMENTATION FOR IMAGING ENERGETIC NEUTRAL ATOMS

H.D. Voss, J. Mobilia, H.L. Collin, and W.L. Imhof
Dept. 91-20, Bldg. 255
Lockheed Palo Alto Research Laboratory
3251 Hanover St.
Palo Alto, Ca. 94303
Phone: 415-424-3299
Fax:: 415-424-3333

We wish to submit this abstract to the conference "Instrumentation for Magnetospheric Imagery " (S. Chakrabarti) at San Diego ' 92.

Direct measurements of energetic neutral atoms (ENA) and ions have been obtained with the cooled solid state detectors on the low altitude (220 km) three-axis stablized S81-1/SEEP satellite and on the spinning 1.1 x 6 Re CRRES satellite. During magnetic storms ENA and ion precipitation is evident over the equatorial region from the LE spectrometer in the SEEP payload (ONR 804) on S81-1 . The spinning motion of the CRRES satellite allows for simple mapping of the magnetosphere using the IMS-HI (ONR 307-8-3) neutral spectrometer. This spectrometer covers the energy range from 20 to 1000 keV and uses a 7 kG magnetic field to screen out protons less than about 50 MeV. Recently, an advanced spectrometer (SEPS) has been developed to image electrons, ions, and neutrals on the despun platform of the POLAR satellite (~1.8 x 9 Re) for launch in 1994 as part of the NASA ISTP/GGS program. For this instrument a 256 element solid state pixel array has been developed that interfaces to 256 amplifier strings using a custom 16 channel microcircuit chip. In addition, this instrument features a motor controlled iris wheel and anticoincidence electronics.

H. D. Voss received his B.S. degree in Electrical engineering from Illinois Institute of Technology in 1972 and M.S. and PhD. degrees in space physics from the University of Illinois, Urbana in 1974 and 1977, respectively. From 1977 to 1979 he developed 10 rocket payloads as a research associate at U. of Illinois. From 1979 to present he has been with the Lockheed Palo Alto Research Laboratory where he has been directly involved with the development of energetic particle, plasma, X-ray, optical, and dust instruments for satellites. He is the author or co-author of over 60 scientific papers in space physics.